

https://dspace.org/

Computational study of structural, electronic and optical properties of molybdenum chalcogenides

Ondzibou, Ninon Gildas

2014-07-22
http://hdl.handle.net/10539/14967

Downloaded from a DSpace repository. https://dspace.org/

Computational study of structural, electronic and optical properties of Molybdenum Chalcogenides

Ninon Gildas Ondzibou (NinonGildas.Ondzibou@students.wits.ac.za)

Supervised by: Professor Daniel P. Joubert (daniel.joubert2@wits.ac.za)

22 April 2014

A dissertation submitted to the Faculty of Science, University of the Witwatersrand, Johannesburg, in fulfillment of the requirements for the degree of Master of Science

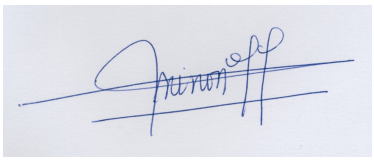


Abstract

Based on first principles calculations the structural, mechanical stability and electronic properties of molybdenum chalcogenides 2H-MoX$_2$ (X = S, Se, Te) have been studied using density functional theory (DFT). The generalized gradient approximation (GGA) proposed by Perdew, Burke and Ernzerhof (PBE) was employed together with the projector augmented plane wave (PAW) method. The van der Waals interactions in the Grimme (DFT-D2) and Lundqvist and Langreth (vdW-DF) approximations have been added on top of PBE or revised PBE in order to take into account the weak interactions between layers of 2H-MoX$_2$ (X = S, Se, Te). The structural properties include the equilibrium lattice parameters, the cohesive energy and the formation energy. Besides we have studied the mechanical stability of these compounds by examining the elastic constants using the PBE, vdW-DF, and DFT-D2 approximations. Other quantities related to the mechanical properties such as the Young's modulus, the Poisson's ratio and the bulk modulus were also calculated. Electronic properties of bulk 2H-MoX$_2$ (X = S, Se, Te) have been investigated using density functional theory (via band structure and projected density of state), and a partially self-consistent GW (GW$_0$) approximation. We have investigated electronic properties (band structure) for monolayers 1H-MoX$_2$ (X = S, Se, Te) using a single shot GW (G$_0$W$_0$) approximation. Optical properties for monolayer 1H-MoX$_2$ (X = S, Se, Te) were studied using the Bethe-Salpeter equation (BSE).

DECLARATION

I declare that this Dissertation is my own, unaided work. Any work done by others of by myself previously has been acknowledge and referenced accordingly. It is being submitted for the Degree of Master of Science at the University of the Witwatersrand, Johannesburg. It has not been submitted before for any degree or examination at any other University.



(Signature of the candidate)

_____day of _____2014

Acknowledgements

I would like to thank God the Almighty (The Lord Jesus Christ) for everything that he has done in my life and who made everything possible.

My profound gratitude goes to my supervisor, Prof. Daniel P. Joubert for his guidance, encouragement and support throughout this project.

I am highly indebted to Dr. Mohammed Suleiman Hussein Suleiman for his valuable assistance with DFT-VASP calculations in the beginning of this project.

I would like to thank George Manyali for all the useful discussions and for helping me in calculating Bethe-Salpeter equation (BSE).

I would like to thank Mr. Darlison Nyirenda in school of Mathmatics for his time in reading and rereading several drafts of this dissertation.

I would also like to acknowledge the financial support provided by the University of the Witwatersrand, Johannesburg South Africa, and the African Institute for Mathematical Sciences (AIMS).

I acknowledge the Centre for High Performance Computing (CHPC) for providing the computational resources to perform some of the calculations in this dissertation.

I would not fail to acknowledge my colleagues Moise Dongho, and Mahmud Abdusalem for all the discussions and jokes during hard time.

Finally, I thank my family and friends no names are mentioned.

List of Figures

5.1 Schematic illustration of photoemission. On left the direct photo-electron spectroscopy in which the energy difference $E_{kin} - \hbar\omega$ corresponds to $\epsilon_i = E_0^N - E_i^{N-1}$. On the right the energy difference corresponds to $\epsilon_i = E_i^{N+1} - E_0^N$ in inverse photo-electron spectroscopy. 34

5.2 This diagram is a sketch of the self-consistent in GW method. In the partially self-consitent GW_0 approximation only G is updated while in the fully self-consistent GW approximation both G and W are updated. 38

6.1 (a) Molybdenum chalcogenides: Bulk 2H-MoX_2 (X = S, Se, Te) and monolayer 1H-MoX_2 (X = S, Se, Te). The big and small balls represent Mo and X (S, Se, Te) atoms respectively. The interlayer distance is denoted by d. (b) and (c), top and side view of the 2H-MoX_2 (X = S, Se, Te) unit cell. 44

6.2 Cohesive energy E_{coh}(eV/atom) versus volume V(Å^3 /atom) for 2H-MoS_2 in three different approximations. 45

6.3 Cohesive energy E_{coh}(eV/atom) versus volume V(Å^3 /atom) for 2H-$MoSe_2$ in three different approximations. 46

6.4 Cohesive energy E_{coh}(eV/atom) versus volume V(Å^3 /atom) for 2H-$MoTe_2$ in three different approximations. 47

6.5 Formation energy E_f(eV/atom) versus 2H-MoX_2 (X = S, Se, Te) in PBE, vdW-DF and DFT-D2, the more negative the energy is, the more favourable the stability. It can be seen that E_f(2H-MoS_2) $< E_f$(2H-$MoSe_2$) $< E_f$(2H-$MoTe_2$), thus at zero temperature 2H-$MoSe_2$, and 2H-$MoTe_2$ have higher formation energies than 2H-MoS_2. 50

7.1 Band gap energies E_{gap} (eV) versus volume V(Å^3 /atom) for 2H-$MoSX_2$ (X = S, Se, Te) in PBE approximation. 57

7.2 Brillouin zone with high symmetry points ($\Gamma - M - K - \Gamma - A - L - H - A$), b_1, b_2, and b_3 represent the lattices vectors. 58

7.3 DFT in PBE approximation: Left, band structure for 2H-MoS_2 at zero pressure. The minimum of conduction band is at 0.48 eV, at the K high symmetry point and the maximum of the valence band is at -0.52 eV, at the Γ high symmetry point, thus an indirect band gap of 1.0 eV. Right, the projected density of state (PDOS). 58

7.4 DFT in DFT-D2 approximation: Left, band structure for 2H-MoS_2 at zero pressure. The minimum of conduction band is at 0.48 eV, at the K high symmetry point and the maximum of the valence band is at -0.43 eV, at the Γ high symmetry point, thus an indirect band gap of 0.91 eV. Right, the projected density of state (PDOS). 59

7.5 DFT in vdW-DF approximation: Left, band structure for 2H-MoS_2 at zero pressure. The minimum of conduction band is at 0.53 eV, at the K high symmetry and the maximum of the valence band is at -0.49 eV, at the Γ high symmetry, thus an indirect band gap of 1.02 eV. Right, the projected density of state (PDOS). 59

7.6 DFT in PBE approximation: Left, band structure for 2H-$MoSe_2$ at zero pressure. The minimum of conduction band is at 0.44 eV, at the K high symmetry point, and the maximum of the valence band is at -0.45 eV, at the Γ high symmetry point, thus an indirect band gap of 0.89 eV. Right, the projected density of state (PDOS). 60

7.7 DFT in DFT-D2 approximation: Left, band structure for 2H-$MoSe_2$ at zero pressure. The minimum of conduction band is at 0.45 eV, at the K high symmetry point, and the maximum of the valence band is at -0.42 eV at the Γ high symmetry point, thus an indirect band gap of 0.87 eV. Right, the projected density of state (PDOS). 60

7.8 DFT in vdW-DF approximation: Left, band structure for 2H-$MoSe_2$ at zero pressure. The minimum of conduction band is at 0.45 eV, at the K high symmetry point and the maximum of the valence band is at -0.50 eV, at the Γ high symmetry point, thus an indirect band gap of 0.95 eV. Right, the projected density of state calculated (PDOS). . 61

7.9 DFT in PBE approximation: Left, band structure for 2H-$MoTe_2$ at zero pressure. The minimum of conduction band is at 0.29 eV, at the K high symmetry point, and the maximum of the valence band is at -0.42 eV, at the Γ high symmetry point, thus an indirect band gap of 0.71 eV. Right, the projected density of state (PDOS). 61

7.10 DFT in DFT-D2 approximation: Left, band structure for 2H-$MoTe_2$ at zero pressure. The minimum of conduction band is at 0.29 eV, at the K high symmetry point, and the maximum of the valence band is at -0.41 eV, at the Γ high symmetry point, thus an indirect band gap of 0.70 eV. Right, the projected density of state (PDOS). 62

7.11 DFT in vdW-DF approximation: Left, band structure for 2H-$MoTe_2$ at zero pressure. The minimum of conduction band is at 0.40 eV, at K high symmetry point, and the maximum of the valence band is at -0.43 eV at Γ high symmetry point, thus an indirect band gap of 0.83 eV. Right, the projected density of state (PDOS). 62

7.12 Band convergence of the quasiparticle band gap of 2H-MoX_2 (X = S, Se, Te) employing a $9 \times 9 \times 1$ **k**-point set in G_0W_0 with the DFT-D2 eigenvalues and wave functions as inputs approximation 65

7.13 Band convergence of the quasiparticle band gap of 1H-MoX_2 (X = S, Se, Te) employing a $12 \times 12 \times 1$ **k**-point set in G_0W_0 with the DFT-D2 eigenvalues and wave functions as inputs approximation 68

7.14 Quasiparticle band structure for 1H-MoS_2 at zero pressure. The minimum of conduction band is at 1.95 eV and the maximum of the valence band is at -0.85 eV, thus a direct band gap of 2.80 eV at K high symmetry point. 68

7.15 Quasiparticle band structure for 1H-$MoSe_2$ at zero pressure. The minimum of conduction band is at 1.61 eV and the maximum of the valence band is at -0.87 eV, thus a direct band gap of 2.48 eV at K high symmetry point. 69

7.16 Quasiparticle bandand structure for 1H-$MoTe_2$ at zero pressure. The minimum of conduction band is at $0.1.43$ eV and the maximum of the valence band is at -0.92 eV, thus a direct band gap of 2.18 eV at K high symmetry point. 69

8.1 Absorption coefficient spectra from BSE calculations for monolayer 1H-$MoTe_2$, as a function of photon energy (ω). 74

8.2 Absorption coefficient spectra from BSE calculations for monolayer 1H-$MoSe_2$, as a function of photon energy (ω). 75

8.3 Absorption coefficient spectra from BSE calculations for monolayer 1H-$MoTe_2$, as a function of photon energy (ω). 75

8.4 Real part of dielectric constant for monolayer 1H-MoS_2, as a function of photon energy ($\hbar\omega$). Computed spectra are presented at the BSE level. 76

8.5 Imaginary part of dielectric constant for monolayer 1H-MoS_2, as a function of photon energy ($\hbar\omega$). Computed spectra are presented at the BSE level. The two energy peaks in the spectrum from 1 eV to 2.5 eV correspond to the A and B excitons. 77

8.6 Real part of dielectric constant for monolayer 1H-$MoSe_2$, as a function of photon energy ($\hbar\omega$). Computed spectra are presented at the BSE level. 78

8.7 Imaginary part of dielectric constant for monolayer 1H-$MoSe_2$, as a function of photon energy ($\hbar\omega$). Computed spectra are presented at the BSE level. The two energy peaks in the spectrum from 1 eV to 2.3 eV correspond to the A and B excitons. 78

8.8 Real part of dielectric constant for monolayer 1H-$MoTe_2$, as a function of photon energy ($\hbar\omega$). Computed spectra are presented at the BSE level. 79

8.9 Imaginary part of dielectric constant for monolayer 1H-$MoTe_2$, as a function of photon energy ($\hbar\omega$). Computed spectra are presented at the BSE level. The two energy peaks in the spectrum from 1 eV to 1.5 eV correspond to the A and B excitons. 79

9.1 Side view of 2H-MoX_2 structure where the big and small balls represent Mo and X (S, Se, Te) atoms respectively. 92

9.2 Top view of 2H-MoX_2 structure where the big and small balls represent Mo and X (S, Se, Te) atoms respectively. 93

9.3 Side view of 1H-MoX_2 structure where the big and small balls represent Mo and X (S, Se, Te) atoms respectively. 94

9.4 Top view of 1H-MoX_2 structure where the big and small balls represent Mo and X (S, Se, Te) atoms respectively. 95

9.5 Top, charge density for 2H-MoS_2 and bottom, charge density for 1H-MoS_2 calculated in 110 plane 96

9.6 Top, charge density for 2H-$MoSe_2$ and bottom, charge density for 1H-$MoSe_2$ calculated in 110 plane 97

9.7 Top, charge density for 2H-$MoTe_2$ and bottom, charge density for 1H-$MoTe_2$ calculated in 110 plane 97

9.8 Convergence test for bulk 2H-MoX_2 (X = S, Se, Te): (a), total energy E versus Kpoints (K_x represents the component of kpoints along x direction, and K_z represents the component of kpoints along z direction). (b), total energy E versus energy cuttoff (E_{cut}, using $9 \times 9 \times 1$, and $9 \times 9 \times 2$ Γ - centered Monkorst-Pack mesh) 98

9.9 Convergence test for monolayer 1H-MoX_2 (X = S, Se, Te): (c), total energy E versus Kpoints (K_x represents the component of kpoints along x direction). (d), total energy E versus energy cuttoff (E_{cut}, using $12 \times 12 \times 1$ Γ - centered Monkorst-Pack mesh) . . 98

List of Tables

6.1 Equilibrium parameters: lattice parameter a, a/c-ratio, equilibrium volume, Bulk modulus B_0 and its pressure derivative $B_0^{'}$ at zero pressure are calculated in PBE, DFT-D2 and vdW-DF. 48

6.2 Formation energy E_f (eV/atom) of 2H-MoX_2 (X = S, Se, Te) in three different approximations. 50

6.3 Elastic constants C_{ij} (GPa), Bulk modulus B (GPa), Poisson's ratio ν, Young's modulus Y (GPa), Shear modulus (GPa) are calculated at zero pressure 53

7.1 Energy band gaps E_{gap} for 2H-MoX_2 (X = S, Se, Te) compounds calculated in DFT within three different approximations. 63

7.2 Energy band gaps E_{gap} for 2H-MoX_2 (X = S, Se, Te) compounds calculated in GW (GW_0) within three different approximations 66

7.3 Relaxed lattice parameter a (Å) and band gap energy E_{gap} (eV) for 1H-MoX_2 (X = S, Se, Te) compounds calculated in GW (G_0W_0) within three different approximations. . . 71

8.1 Data from BSE calculations for monolayers 1H-MoX_2 (X = S, Se, Te) calculated in DFT-D2. Transition energy E(eV) for A and B excitons. 81

8.2 Binding energy E_b for 1H-MoX_2 (X = S, Se, Te) compounds for each exciton in three different approximations. 82

Contents

Abstract i

Declaration ii

Acknowledgements iii

List of Figures vii

List of Tables viii

1 Introduction 1

1.1 Molybdenum chalcogenides . . . 1

1.2 Motivation . . . 2

1.3 Aim . . . 3

1.4 Dissertation outline . . . 4

2 Theoretical Methods 5

2.1 Many-body problem . . . 5

2.2 Electronic density . . . 7

2.3 Hartree-Fock Approximation . . . 7

2.4 Density Functional Theory . . . 10

2.5 Functional for exchange and correlation . . . 15

2.6 Hybrid functionals . . . 19

2.7 Van der Waals approximation . . . 21

3 Elastic constants of solids 22

3.1 Generalized Hooke's Law . . . 22

3.2 Reduced elastic constant matrices . . . 24

4 Outline of calculations 26

4.1 Vienna Ab-Initio Simulation Package . . . 26
4.2 Equation of state . . . 26
4.3 Cohesive energy . . . 27
4.4 Formation energy . . . 28
4.5 Electronic Density of state . . . 28
4.6 Band Gap . . . 29
4.7 Phenomenological study of the optical functions . . . 30

5 Many-body perturbation theory **33**

5.1 Quasiparticle . . . 33
5.2 One particle Green's function . . . 33
5.3 Self energy in GWA . . . 35
5.4 Hedin's equations . . . 37
5.5 GW approximation . . . 37
5.6 Dielectric matrix and Polarizability . . . 39
5.7 Two particles Green's function . . . 40
5.8 Second iteration of Hedin's equation . . . 41
5.9 Excitonic Hamiltonian . . . 42

6 Structural properties **43**

6.1 Cohesive energy . . . 43
6.2 Formation energy . . . 49
6.3 Mechanical stability . . . 50

7 Electronic properties **54**

7.1 Band Structure and Projected Density of States in DFT . . . 55
7.2 Energy band gap in the GW approximation . . . 64
7.3 Computational methods . . . 64
7.4 Quasiparticles in the GW approximation . . . 65
7.5 Band Structure of monolayer 1H-MoX_2 (X = S, Se, Te) in the GW approximation . . . 67

8 Optical properties 72

9 Conclusion 83

References 107

1. Introduction

Amongst the major technological challenges of the twenty first century are the harvesting of renewable energy sources and the miniaturisation of electronic components. Molybdenum chalcogenides are promising materials to investigate for meeting both these challenges. These layered materials have structural properties similar to graphene, but in contrast to graphene, some of the molybdenum chalcogenides, such as molybdenum disulfide, have an intrinsic band gap. A band gap is a property essential for many applications. In this chapter we introduce some properties and applications of the molybdenum chalcogenides and give a motivation for studying them.

1.1 Molybdenum chalcogenides

Nanoscience and nanotechnology have been dominated by low dimensional honeycomb structured carbon based materials in the last two decades. Graphene, a two dimensional honeycomb structure of carbon, has been investigated in great detail by researchers but has no band gap [1, 2]. However, molybdenum chalcogenides are inorganic layered materials similar to graphene, but in contrast to graphene, some of the molybdenum chalcogenides, such as molybdenum disulfide (MoS_2), have an intrinsic band gap. A band gap is a property essential for many applications including low dimensional transitors, optoelectronic devices and solar energy harvesters. MoS_2 has a layered structure with each layer consisting of S-Mo-S sheets, consisting of an atomic plane of Mo sandwiched between two atomic planes of S in a trigonal prismatic arrangement. While atoms in each layer are strongly bound, layers are attracted to each other by weak van der Waals forces conferring on MoS_2 an anisotropic structure, and anisotropic electrical, optical, and mechanical properties [3]. There has been a search for other two dimensional materials that can be split from the bulk into individual atomic layers for more intriguing properties and phenomena [4, 5, 6].

Recently, layered molybdenum disulfide (MoS_2) was synthesised for the first time [7]. As the number of layers decreases from bulk (indirect gap) to a monolayer, the gap increases and changes from an indirect to a direct band gap [1]. MoS_2 is a promising material for electronic applications because of its stability and transport characteristics [3]. The optical properties and the electronic structure of (MoS_2) have been investigated by optical spectroscopy. The indirect bulk band gap has a value of 1.23 eV and the monolayer direct gap is 1.8 eV [1]. A direct band gap does not require phonon assisted photo-absorption. In fact the energy band gap is a function of the momentum (**k**-vector) in the Brillouin zone, the latter momentum is related to the minimum energy state in the conduction band and the maximum energy state in the valence band. If the momentum of electron-holes is the same in both the conduction band and the valence band, then an electron can be directly emitted by a photon without passing through an intermediate state which refers to a direct band gap. Therefore offers the possibility of constructing thin solar cells [8, 7]. For an indirect band gap an electron is assited by photon absorption.

For a semiconductor to be used in solar-energy conversion, its electronic band structure is one of the

most important parameters and determines, among others, the range of the solar spectrum it can absorb [9]. Various theoretical approaches have also been used to study electronic band structures of molybdenum chalcogenides [10, 9]. Most of those studies are based on Kohn-Sham density functional theory (KS-DFT) in the local-density or generalized gradient approximations (LDA/GGA). KS-DFT with LDA/GGA suffers from the well-known band gap problem. A method of improving the band gap is a hybrid functional which adds a certain amount of exact exchange to DFT exchange [11]. However, formally KS-DFT does not yield the correct band-gap [12]. A theoretically rigorous way to solve the band gap problem is to go beyond the KS-DFT framework by formulating the electronic band structure in terms of the single-particle Green's function [13]. Many-body perturbation theory in the GW approximation is currently the most accurate first principles approach to describe the electronic band structure of crystalline systems. The GW method gives an approximation to the fundamental gap (difference in energy between the ionisation energy and electron affinity) and not the optical gap. A good band structure is not enough when one is interested in spectroscopy like absorption, where one creates a neutral, i.e., electron-hole type excitation. One needs to go to the so called Bethe-Salpeter equation (BSE) to include electron-hole interactions to calculate an approximation to the optical gap which is necessary to know if optical absorption is of interest.
The challenges of ab-initio modelling of these materials are three fold:
Firstly, an accurate characterisation of structural and mechanical properties of these materials in their bulk form.
Secondly, the ab-initio calculation must be capable of handling large systems and also be free of the well-known band gap problem of the density functional theory (DFT)
Thirdly, to accurately predict the optical spectra of these materials which are directly accessible through experimental techniques such as photoabsorption, and photoluminescence spectroscopy.

1.2 Motivation

An increased effort in the field of renewable energy in general and solar energy in particular is necessary for the following reasons:

- The intensive use of fossil fuels (oil, natural gas, etc.) puts the global ecosystem in peril. The combustion of these materials leads to, among others, the release of carbon dioxide, the main greenhouse gas responsible for the warming of the planet. The results of such a warming could be difficult to control and catastrophic for humanity. Most local effects to consumption of fossil fuels are being felt in many cities (Athens, Bangkok, Tokyo, etc.).
- Renewable energies can be a non-negligible factor in the development for both undeveloped and developed countries. Renewable energies have the advantage of being available locally and not being dependent on supply networks necessitating a heavy and expensive infrastructure [14, 15].
- Fossil energy sources are available in limited quantities. Even if the curve of new deposits follows

> the curve of consumption, it appears probable, according to many estimates, that after fifty years of supply, problems could be felt.

It is desirable that the six billion inhabitants of the planet one day have access to the energy as easily as people in industrialized countries. But if every person on the planet would consume as much as fossil energy as do western countries currently, the result would be the increase in pollution and shortage of fuel. The reduction of consumption of fossil energy has therefore become a challenge to the western society, as well as the implementation of alternative strategies based on renewable energies. In developing countries, many projects have been or are about to be realized such as the electrification by photovoltaic which allows operation of water pumps, night lighting, powering a radio etc.
Layered molybdenum chalcogenides MoX_2 (X = S, Se, Te) have attracted great interest because of their distinctive structural, electronic and optical properties. Furthermore, layered molybdenum chalcogenides MoX_2 (X = S, Se, Te) are semiconductors with a high coefficient of absorption, and a band gap for absorbing a large part of the solar spectrum. They are therefore potential candidates for being the active element of a solar cell.

The most commonly used solar cell material is crystalline silicon (Si), despite the fact that it is indirect band gap and therefore does not absorb light very well. Silicon solar cells are typically 100μm thick; if it was much thinner, much of the light (particularly in the infrared) would simply pass through. On the other hand, thin-film solar cells are made of direct band gap materials (such as MoX_2 (X = S, Se, Te)), which absorb the light in a much thinner region, and consequently can be made with a very thin active layer (often less than 1μm thick) [16].

Recently a two dimensional, single layer MoS_2 transistor was built [7] while CdS and CDTe, for example, have been used in solar cell applications [17].
From a theoretical point of view, the inter-layer interaction of $MoS2$, a layered materials is dominated by weak van der Waals-type interactions. It is fortunate at this time that theoretical and computational tools to perform a systematic study of the structural, electronic, and optical properties are reaching the level of accuracy that will allow a reliable identification of optimal materials [18].
Density functional theory with the inclusion of van der Waals interactions to deal with interlayer van der Waals force, can give highly accurate structural information for molybdenum chalcogenide compounds. Many-body techniques at the GW level have been developed to a point where accurate fundamental gap energies can be calculated and the optical gap can be determined at the BSE level of approximation.

1.3 Aim

The objective of this work is as follows:

1. To computationally investigate the structural properties of bulk molybdenum chalcogenides MoX_2 (X = S, Se, Te) within density functional theory in three different approximations for the exchange-

correlation namely the Perdew-Burke-Ernzerhof (PBE), Grimme (DFT-D2), and Lundqvist and Langreth (vdw-DF).

2. To investigate the mechanical stability of molybdenum chalcogenides at the calculated equilibrium configuration, using elastic constants.

3. To investigate the electronic properties of bulk molybdenum chalcogenides MoX_2 (X = S, Se, Te) in density functional theory and the GW approximation in order to identify potential optimal materials for low dimensional solar energy harvesters.

4. To investigate the electronic properties of monolayer molybdenum chalcogenides in the GW approximation.

5. To investigate the optical properties of monolayer molybdenum chalcogenides in the BSE approximation.

1.4 Dissertation outline

This dissertation is organized as follows. In Chapter 2, we review the many body problem of electrons and discuss density functional theory (DFT) with different approximations of exchange correlation energy. We also discuss the long range dispersion interactions, generally denoted as van der Waals interactions. In Chapter 3, we discuss elastic constants of solids and a practical method of obtaining them. In Chapter 4 we describe the computational method that enables the calculation of the ground states properties in DFT, in and we also review the Viena Ab-Initio Simulation Package (VASP) and the band gap problem. In Chapter 5 we give a brief description of the key concepts of many-body perturbation theory (MBPT) and the GW approximation. Chapter 6 is dedicated to the structural properties and mechanical stability. In Chapter 7 we present the electronic properties for both bulk and monolayer of molybdenum chalcogenides compounds. In chapter 8 we present the optical properties of the monolayer of these compounds. Finally we present the conclusion.

2. Theoretical Methods

One of the most challenging problems in condensed matter physics, computational materials physics and quantum chemistry is to describe the structure and electronic structure of many-atom, many-electron systems. The interactions between atoms and electrons are governed by the laws of quantum mechanics. The problem is to derive the properties of many-atom, many-electron systems from the quantum mechanical laws. Furthermore, the properties of matter can broadly be ranged into two categories: 1) the electronic ground state properties such as cohesive energy, equilibrium crystal structure, elastic properties, charge density, and 2) electronic excited states such as low-energy excitations in metals, susceptibility, higher energy excitation that determine insulating gaps, optical properties spectra for adding and removing electrons. This distinction determines the framework for theoretical understanding and development of the entire field of electronic structure calculations [19], hence, accurate and efficient methods for solving the quantum mechanical equation for many-atom system must be developed [20]. Various electronic structure methods have been developed in the past. The most widely used method for structural and electronic structure calculations is Density Functional Theory (DFT). It is one of the most reliable theories for predicting potential materials with specific properties.

2.1 Many-body problem

The study and the analysis of the electronic structure of matter is done by solving the Schrödinger equation of many-atom systems. Considering Ψ the wave function of a many-atom system, the general form of the Schrödinger equation can be written as follows (excluding spin for simplicity of notation):

$$\hat{\mathcal{H}}\Psi(\mathbf{R}_1, ..., \mathbf{R}_N; \mathbf{r}_1, ..., \mathbf{r}_n) = E\Psi(\mathbf{R}_1, ..., \mathbf{R}_N; \mathbf{r}_1, ..., \mathbf{r}_n), \tag{2.1.1}$$

where E is the energy of the system, $\mathbf{R}_i$ and $\mathbf{r}_i$ are respectively the positions of the nuclei and the positions of the electrons. N and n are respectively the number of nuclei and electrons of the system. The Hamiltonian operator is given by:

$$\hat{\mathcal{H}} = \hat{T}_n + \hat{V}_{nn} + \hat{T}_e + \hat{V}_{ee} + \hat{V}_{en}. \tag{2.1.2}$$

In (2.1.2), $\hat{T}_n$ represents the kinetic energy of the nuclei,

$$\hat{T}_n = \sum_i^N -\frac{\hbar^2}{2M_i}\nabla^2_{\mathbf{R}_i} \tag{2.1.3}$$

where $\mathbf{R}_i$ represents the position of the atom i with mass M_i. The second term represents the interaction energy of the nuclei with charges $(Z_i e)$

$$\hat{V}_{nn} = \sum_{i<j}^N \frac{Z_i Z_j e^2}{|\mathbf{R}_i - \mathbf{R}_j|}. \tag{2.1.4}$$

The remaining terms in (2.1.2) are respectively the electronic kinetic energy, the electron-electron interaction energy and the electron-nuclei interaction energy operators:

$$\hat{T}_e = \sum_{i}^{N} -\frac{\hbar^2}{2m}\nabla^2_{\mathbf{r}_i} \tag{2.1.5}$$

$$\hat{V}_{ee} = \sum_{i<j}^{N} \frac{e^2}{|\mathbf{r}_i - \mathbf{r}_j|} \tag{2.1.6}$$

$$\hat{V}_{en} = \sum_{i=1}^{N}\sum_{j=1}^{N} \frac{Z_i e^2}{|\mathbf{R}_i - \mathbf{r}_j|}. \tag{2.1.7}$$

The standard step to solve (2.1.1) is the Born-Oppenheimer approximation in which the wave function of many-atom systems can be written as the product of the following form:

$$\Psi(\mathbf{R}_i, \mathbf{r}_j) = \Psi_n(\mathbf{R}_i)\Psi_e(\mathbf{R}_i, \mathbf{r}_j), \tag{2.1.8}$$

where $\Psi_n(\mathbf{R}_i)$ in (2.1.8) represents the wave function of the nuclei and $\Psi_e(\mathbf{R}_i, \mathbf{r}_j)$ is the electronic wave function. Substituting (2.1.8) in (2.1.2) we obtain the following equations

$$\hat{\mathcal{H}}_e\Psi_e(\mathbf{R}_i, \mathbf{r}_j) = (\hat{T}_e + \hat{V}_{ee} + \hat{V}_{en})\Psi_e(\mathbf{R}_i, \mathbf{r}_j) \tag{2.1.9}$$

which gives

$$\hat{\mathcal{H}}_e\Psi_e(\mathbf{R}_i, \mathbf{r}_j) = E^e\Psi_e(\mathbf{R}_i, \mathbf{r}_j) \tag{2.1.10}$$

and

$$\hat{\mathcal{H}}_n\Psi_n(\mathbf{R}_i) = (\hat{T}_n + \hat{V}_{nn} + E^e)\Psi_n(\mathbf{R}_i) \tag{2.1.11}$$

from which we get

$$\hat{\mathcal{H}}_n\Psi_n(\mathbf{R}_i) = E^n\Psi_n(\mathbf{R}_i). \tag{2.1.12}$$

If we consider the potential of the nuclei in (2.1.9) as static, and let $\hat{V}_{en} = \hat{V}_{ext}$, we get the time independent electronic Hamiltonian

$$\hat{\mathcal{H}} = \hat{T}_{ee} + \hat{V}_{ee} + \hat{V}_{ext}. \tag{2.1.13}$$

Let

$$\hat{\mathcal{H}} = \hat{F} + \hat{V}_{ext}, \tag{2.1.14}$$

where $\hat{F}$ is the sum of the kinetic and mutual Coulomb interaction energy operator and $\hat{V}_{ext}$ the external potential energy which describes the attraction between the electrons and nuclei. The many-body problem is still immensely difficult to solve; various approximations have been developed over the years such as: Hartree-Fock (HF) approximation and density function theory (DFT).

2.2 Electronic density

Let $\mathbf{r}_i$ be the position of electron i, with spin coordinate $\sigma_i = \uparrow$ or $\downarrow$ and N the total number of electrons. The wave function of a many-electron system describes the quantum mechanical behaviour of that system and depends on the position and spin coordinates $\Psi_e(\mathbf{r}_1\sigma_1, \mathbf{r}_2\sigma_2, \ldots, \mathbf{r}_N\sigma_N)$. This wave function satisfies two conditions: firstly it must be normalized

$$\langle \Psi_e | \Psi_e \rangle = \sum_{\sigma_1 \ldots \sigma_N} \int d\mathbf{r}_1 \int \mathbf{r}_2 \ldots \int d\mathbf{r}_N |\Psi_e(\mathbf{r}_1\sigma_1, \mathbf{r}_2\sigma_2, \ldots, \mathbf{r}_N\sigma_N)|^2 = 1, \tag{2.2.1}$$

and secondly it must be antisymmetric,

$$\Psi_e(\ldots, \mathbf{r}_i\sigma_i, \ldots, \mathbf{r}_j\sigma_j, \ldots) = -\Psi_e(\ldots, \mathbf{r}_j\sigma_j, \ldots, \mathbf{r}_i\sigma_i, \ldots). \tag{2.2.2}$$

In an electronic system, the electronic density $n(\mathbf{r})$ for a given state is defined as the number of electrons per unit volume at the point $\mathbf{r}$ for that state. The total number of electrons is given by

$$\int n(\mathbf{r}) d^3r = N, \tag{2.2.3}$$

The density can be expressed as the expectation value of the density

$$n(\mathbf{r}) = \sum_{i=1}^{N} \delta(\mathbf{r} - \mathbf{r}_i) \tag{2.2.4}$$

so that the relation between $n(\mathbf{r})$ and many-electron wave function is

$$n(\mathbf{r}) = N \sum_{\sigma_2 \ldots \sigma_N} \int d\mathbf{r}_2 \int d\mathbf{r}_3 \ldots \int d\mathbf{r}_N |\Psi_e(\mathbf{r}_2\sigma_2, \mathbf{r}_3\sigma_3, \ldots, \mathbf{r}_N\sigma_N)|^2. \tag{2.2.5}$$

The expression on the right hand side looks similar to the wave-function normalization integration (2.2.1), but without one of the spatial integrals, and thus one coordinate is left free.
We define the electron spin density $n_\sigma(\mathbf{r})$ so that $n_\sigma(\mathbf{r})d^3r$ is the probability to find the electron with spin σ in volume element d^3 at $\mathbf{r}$. Integrating over the coordinates and spin of the (N-1) other electrons we have

$$n_\sigma(\mathbf{r}) = \frac{1}{(N-1)!} \sum_{\sigma_2 \ldots \sigma_N} \int d^3\mathbf{r}_2 \ldots \int d^3r_N N! |\Psi(\mathbf{r}\sigma, \mathbf{r}_2\sigma_2, \ldots, \mathbf{r}_N\sigma_N)|^2. \tag{2.2.6}$$

Combining (2.2.1) and (2.2.6) yields

$$\sum_\sigma \int d\mathbf{r} n_\sigma(\mathbf{r}) = \int (n_\uparrow(\mathbf{r}) + n_\downarrow(\mathbf{r})) = N. \tag{2.2.7}$$

2.3 Hartree-Fock Approximation

The Hartree-Fock (HF) approximation can be viewed as a variational method in which the wave functions of many-electron system have the form of an antisymetrised product of one-electron wave functions.

This restriction leads to an effective Schrödinger equation for individual one-electron wave functions called orbitals with a potential determined by the orbitals occupied by the other electrons [21].
Let $\Psi^H(\mathbf{r})$ be a many-electron wave function for non-interacting electrons called Hartree wave function and given by

$$\Psi^H(\mathbf{r}_i) = \Phi_1(\mathbf{r}_1)\Phi_2(\mathbf{r}_2)\dots\Phi_N(\mathbf{r}_N) \tag{2.3.1}$$

with the index i running over all electrons and $\Phi_i(\mathbf{r}_i)$ are the one-electron wave functions. The total energy of the system is given by

$$E^H = \langle\Psi^H|\hat{\mathcal{H}}|\Psi^H\rangle \tag{2.3.2}$$

$$E^H = \sum_i \langle\Phi_i| - \frac{\hbar^2}{2m}\nabla^2_{\mathbf{r}} + \hat{V}_{ext}(\mathbf{r})|\Phi_i\rangle + \frac{e^2}{2}\sum_{ij(j\neq i)}\langle\Phi_i(\mathbf{r}_i)\Phi_j(\mathbf{r}')|\frac{1}{|\mathbf{r}-\mathbf{r}'|}|\Phi_i(\mathbf{r})\Phi_j(\mathbf{r}')\rangle. \tag{2.3.3}$$

On using a variational argument, we arrive at the single-electron Hartree equation

$$\left[-\hbar^2\frac{\nabla^2_{\mathbf{r}}}{2m} + \hat{V}_{ext}(\mathbf{r}) + e^2\sum_{j\neq i}\langle\Phi_j(\mathbf{r}')|\frac{1}{|\mathbf{r}-\mathbf{r}'|}|\Phi_j(\mathbf{r}')\rangle\right]\Phi_i(\mathbf{r}) = \epsilon_i\Phi_i(\mathbf{r}) \tag{2.3.4}$$

where ϵ_i are Lagrange multipliers introduced to take into account the normalization of the single-electron wave functions Φ_i. We define the Hartree potential as

$$V_i^H(\mathbf{r}) = e^2\sum_{j\neq i}\langle\Phi_j(\mathbf{r}')|\frac{1}{|\mathbf{r}-\mathbf{r}'|}|\Phi_j(\mathbf{r}')\rangle. \tag{2.3.5}$$

Since the Hartree wave function does not obey the Pauli Exclusion Principle [22], we incorporate the Fermionic nature of electrons in the many-body wave function so that we can build a wave function which is antisymmetrized for the Hartree wave function, this latter wave function changes sign when the coordinates of two electrons are interchanged. This is known as the Hartree Fock (HF) approximation. In order to describe the Hartree-Fock wave functions, we combine the Hartree version wave function to form a properly antisymmetrized wave function for the system [23]. For simplicity we will neglect the spin of electrons and deep only the spatial degrees of freedom. We obtain the Hartree Fock wave function as

$$\Psi^{HF}(\mathbf{r}_i) = \frac{1}{\sqrt{N!}}\begin{vmatrix}\Phi_1(\mathbf{r}_1) & \Phi_1(\mathbf{r}_2) & \cdots & \Phi_N(\mathbf{r}_N)\\ \Phi_2(\mathbf{r}_1) & \Phi_2(\mathbf{r}_2) & \cdots & \Phi_N(\mathbf{r}_N)\\ \vdots & \vdots & & \vdots\\ \Phi_N(\mathbf{r}_1) & \Phi_N(\mathbf{r}_2) & \cdots & \Phi_N(\mathbf{r}_N)\end{vmatrix}.$$

The total energy with the Hartree-Fock wave function is given by

$$\begin{aligned} E^{HF} &= \langle \Psi^{HF} | \hat{\mathcal{H}} | \Psi^{HF} \rangle \\ &= \sum_i \langle \Phi_i | -\frac{\hbar^2}{2m}\nabla^2_{\mathbf{r}} + \hat{V}_{ext}(\mathbf{r}) | \Phi_i \rangle \\ &+ \frac{e^2}{2} \sum_{ij(j\neq i)} \langle \Phi_i \Phi_j | \frac{1}{|\mathbf{r}-\mathbf{r}'|} | \Phi_i \Phi_j \rangle \\ &- \frac{e^2}{2} \sum_{ij(j\neq i)} \langle \Phi_i \Phi_j | \frac{1}{|\mathbf{r}-\mathbf{r}'|} | \Phi_j \Phi_i \rangle \end{aligned} \tag{2.3.6}$$

Minimising the energy a variational calculation gives

$$\left[-\frac{\hbar^2}{2m}\nabla^2\mathbf{r} + V_{ext}(\mathbf{r}) + V_i^H(\mathbf{r}) \right] \Phi_i(\mathbf{r}) - e^2 \sum_{j\neq i} \langle \Phi_j | \frac{1}{|\mathbf{r}-\mathbf{r}'|} | \Phi_i \rangle \Phi_j(\mathbf{r}) = \epsilon_i(\mathbf{r}) \Phi_i(\mathbf{r}). \tag{2.3.7}$$

Equation (2.3.7) has an extra term in first term compare to the Hartree (2.3.4). This term describes exchange between electrons. Now construct a single-electron exchange density as

$$n_i^x(\mathbf{r}, \mathbf{r}') = \sum_{j\neq i} \frac{\Phi_i(\mathbf{r}) \Phi_i^*(\mathbf{r}') \Phi_j(\mathbf{r}') \Phi_j^*(\mathbf{r}')}{\Phi_i(\mathbf{r}) \Phi_i^*(\mathbf{r})}. \tag{2.3.8}$$

A single-electron Hartree-Fock equation can be written as

$$\left[-\frac{\hbar^2 \nabla^2_{\mathbf{r}}}{2m} + V_{ext}(\mathbf{r}) + V_i^H(\mathbf{r}) + V^x(\mathbf{r}) \right] \Phi_i(\mathbf{r}) = \epsilon_i \Phi_i(\mathbf{r}) \tag{2.3.9}$$

where $V^x(\mathbf{r})$ is the exchange potential and given by

$$V_i^x(\mathbf{r}) = -e^2 \int \frac{n_i^x(\mathbf{r}, \mathbf{r}')}{|\mathbf{r}-\mathbf{r}'|} d\mathbf{r}' \tag{2.3.10}$$

The Hartree and the exchange potentials give the electron-electron interaction in the Hartree-Fock approximation

$$V_i^{HF} = e^2 \int \frac{n(\mathbf{r}')}{|\mathbf{r}-\mathbf{r}'|} d\mathbf{r}' - e^2 \int \frac{n_i(\mathbf{r}') + n_i^x(\mathbf{r}, \mathbf{r}')}{|\mathbf{r}-\mathbf{r}'|} d\mathbf{r}'. \tag{2.3.11}$$

It follows that the total electron-electron interaction potential

$$V_i^{HF}(\mathbf{r}) = e^2 \int \frac{n(\mathbf{r}') - n_i^{HF}(\mathbf{r}, \mathbf{r}')}{|\mathbf{r}-\mathbf{r}'|} d\mathbf{r}'. \tag{2.3.12}$$

The Hartree-Fock is commonly used in chemistry and gives accurate results for a small number of electrons, but is inefficient in the study of solids. In this work we will focus on density functional theory which is a theory of correlated many-atom systems, based on the electronic density $n(\mathbf{r})$, and transforms the problem into a minimization of a functional using a fictitious system of independent electrons.

2.4 Density Functional Theory

Density functional theory (DFT) is a mathematical tool for solving problems in many-body systems such as those encountered in studies of correlated many-electrons systems in general, and crystalline solids in particular. In contrast to the theory of Hartree-Fock (Hartree-Fock approximation) which describes individual electrons in interaction with the rest of the electrons and nuclei of these systems, DFT is based on a description of the entire system, and provides a better approximation for solving many-electron problems. The formalism of DFT is developed on the basis of two theorems proposed by Hohenberg and Kohn in 1964, through the consideration of the effects of correlation studies of the physical properties of the ground state of many-electron systems [24]. The correlations, thus introduced in terms of contributions of exchange-correlation (xc) provide highly accurate energy calculations of many-electron systems. In this part we introduce the concept of density functional theory and some of its approximations.

2.4.1 Hohenberg-Kohn theorems. In 1927 the original density functional theory of quantum systems was proposed by Thomas and Fermi in which the energy can be written in terms of the electronic density. Their approach is not accurate enough for realistic calculations. In 1964, Hohenberg and Kohn formulated and proved a theorem that puts former ideas on solid mathematical ground [24]. The theorem is divided into two parts [25].

- **Theorem 1 :** An external potential is uniquely determined by the corresponding ground state density, to within an additive constant.
  Proof : Let $V^1_{ext}(\mathbf{r})$ and $V^2_{ext}(\mathbf{r})$ be respectively two external potentials that differ by more than a constant, but which lead to the same ground state density $n(\mathbf{r})$. The total number of particles is given by :
  $$N = \int n(\mathbf{r}) d^3r. \tag{2.4.1}$$
  Let Ψ_1 and $E_1 = \langle\Psi_1|\hat{\mathcal{H}}_1|\Psi_1\rangle$ be the ground state wave function and ground state energy of Hamiltonian $\hat{\mathcal{H}}_1 = \hat{F} + \hat{V}^1_{ext}$. Similarly let Ψ_2 and $E_2 = \langle\Psi_2|\hat{\mathcal{H}}_2|\Psi_2\rangle$ be the ground state wave function and ground state energy of Hamiltonian $\hat{\mathcal{H}}_2 = \hat{F} + \hat{V}^2_{ext}$. Since Ψ_2 is not the ground state of $\hat{\mathcal{H}}_1$, it follows
  $$E_1 = \langle\Psi_1|\hat{\mathcal{H}}_1|\Psi_1\rangle < \langle\Psi_2|\hat{\mathcal{H}}_1|\Psi_2\rangle. \tag{2.4.2}$$
  The strict inequality above follows if the ground state is non-degenerate. Using the Rayleigh-Ritz variational principle we have
  $$E_1 < \langle\Psi_2|\hat{\mathcal{H}}_1|\Psi_2\rangle = \langle\Psi_2|\hat{\mathcal{H}}_2|\Psi_2\rangle + \langle\Psi_2|\hat{\mathcal{H}}_1 - \hat{\mathcal{H}}_2|\Psi_2\rangle \tag{2.4.3}$$
  $$E_1 < E_2 + \int n(\mathbf{r}) \left[V^1_{ext}(\mathbf{r}) - V^2_{ext}(\mathbf{r})\right] d^3r. \tag{2.4.4}$$
  Also
  $$E_2 < \langle\Psi_1|\hat{\mathcal{H}}_2|\Psi_1\rangle = \langle\Psi_1|\hat{\mathcal{H}}_1|\Psi_1\rangle + \langle\Psi_1|\hat{\mathcal{H}}_2 - \hat{\mathcal{H}}_1|\Psi_2\rangle \tag{2.4.5}$$

$$E_2 < E_1 + \int n(\mathbf{r}) \left[V_{ext}^2(\mathbf{r}) - V_{ext}^1(\mathbf{r})\right] d^3r. \tag{2.4.6}$$

Adding (2.4.4) and (2.4.6) we find that $E_1 + E_2 < E_1 + E_2$, which is a contradiction. Therefore there cannot be an external potential $V_{ext}^2(\mathbf{r})$ which is equal to $V_{ext}^1(\mathbf{r})+c$ and gives the same density state $n(\mathbf{r})$, where c is a constant. Since $n(\mathbf{r})$ determines the external potential and N, it also determines $\hat{\mathcal{H}}$. Hence, all properties are derivable from $n(\mathbf{r})$ through the solution of Schrödinger equation.

- **Theorem 2 :** For any external potential $V_{ext}(\mathbf{r})$, we can define the energy functional $E[n]$ in terms of the electronic density $n(\mathbf{r})$ so that the density which minimizes the energy is the ground state density.

  Proof : We saw that all properties are derivable from $n(\mathbf{r})$ such as kinetic energy, electron-electron interaction energy, such properties can be viewed as a functional of $n(\mathbf{r})$, including the total energy

$$E[n] = \langle \Psi[n] | \hat{T} + \hat{V}_{ee} | \Psi[n] \rangle + V_{ext}[n] \tag{2.4.7}$$

and

$$F[n] = \langle \Psi[n] | \hat{T} + \hat{V}_{ee} | \Psi[n] \rangle. \tag{2.4.8}$$

$F[n]$ is the functional of $n(\mathbf{r})$ through $\Psi(\mathbf{r}_1\sigma_1, \mathbf{r}_2\sigma_2, \ldots, \mathbf{r}_N\sigma_N)$. Since the kinetic energy and the interaction of the particles are functionals of the density $n(\mathbf{r})$ only, $F[n]$ must be universal by construction i.e, it is the same for any electronic systems therefore $F[n]$ does not depend on anything else than the electron density (which is determined uniquely by the external potential V_{ext} that differs from system to system) [23]. Thus such of density is called $v-representable$. Let $\tilde{n}(\mathbf{r})$ be a positive density normalized to N and the corresponding energy functional $E[\tilde{n}]$ is defined by

$$E[\tilde{n}] = F[\tilde{n}] + \int \tilde{n}(\mathbf{r}) V_{ext}(\mathbf{r}) d^3r \tag{2.4.9}$$

and

$$F[\tilde{n}] = \langle \Psi[\tilde{n}] | \hat{T} + \hat{V}_{ee} | \Psi[\tilde{n}] \rangle. \tag{2.4.10}$$

Here $\Psi[\tilde{n}]$ represents the ground state wave function which has $\tilde{n}(\mathbf{r})$ as ground state density. Also for any $n(\mathbf{r}) \neq \tilde{n}(\mathbf{r})$, where $n(\mathbf{r})$ is the ground state density of $E[n]$, we have

$$\langle \Psi[n] | \hat{\mathcal{H}} | \Psi[n] \rangle = F[n] + \int n(\mathbf{r}) V_{ext}(\mathbf{r}) d^3r \tag{2.4.11}$$

and

$$\langle \Psi[\tilde{n}] | \hat{\mathcal{H}} | \Psi[\tilde{n}] \rangle = F[\tilde{n}] + \int \tilde{n}(\mathbf{r}) V_{ext}(\mathbf{r}) d^3r, \tag{2.4.12}$$

Then

$$E[\tilde{n}] > E[n] = \langle \Psi[n] | \hat{\mathcal{H}} | \Psi[n] \rangle. \tag{2.4.13}$$

The knowledge of universal functional $F[n]$ implies the knowledge of the solution of the many-body Schrödinger equation. The problem now becomes finding the universal functional in Equation (2.4.11) from which the exact energy and the ground state density can be found by minimizing the energy. These two theorems form the mathematical basis of density functional theory [25].

2.4.2 Constrained search approach. The second HK assumes that the density that minimizes the energy is the density of the ground state and the latter density must be $v-representable$. However Levy and Lieb [26] extend that theorem to degenerate ground state by a weaker constraint, that the density is $N-representable$. The proof involves a constrained search over all any antisymmetric wave functions (N-particle wave functions) $\Psi^{'}$ generated by the ground state density $n(\mathbf{r})$. Let Ψ be the true wave function for the ground state density $n(\mathbf{r})$, the variational principle gives

$$E[n] = \langle\Psi|\hat{H}|\Psi\rangle < \langle\Psi^{'}|\hat{H}|\Psi^{'}\rangle. \tag{2.4.14}$$

On recalling the energy due to the external potential, we obtain

$$\langle\Psi[n]|\hat{T}+\hat{V}_{ee}|\Psi[n]\rangle + \int n(\mathbf{r})V_{ext}(\mathbf{r}) < \langle\Psi^{'}[n]|\hat{T}+\hat{V}_{ee}|\Psi^{'}[n]\rangle + \int n(\mathbf{r})V_{ext}(\mathbf{r})d^3r. \tag{2.4.15}$$

We define the Levy-Lieb universal functional as

$$F[n] = \min_{\Psi\to n}\langle\Psi|\hat{T}+\hat{V}_{ee}|\Psi\rangle. \tag{2.4.16}$$

$F[n]$ differs from the universal functional defined in the HK theorem in (2.4.8) by the fact that it is defined for all wave functions that yield the input density $n(\mathbf{r})$ and allows the energy to be expressed as

$$E = \min_{n}\left[\min_{\Psi\to n}\langle\Psi|\hat{T}+\hat{V}_{ee}|\Psi\rangle + \int n(\mathbf{r})V_{ext}(\mathbf{r})d^3r\right]. \tag{2.4.17}$$

The constraint of fixed N can be defined by introducing a Lagrange multiplier μ

$$\delta\left\{F[n] + \int d^3rV_{ext}(\mathbf{r})n(\mathbf{r}) - \mu\int d^3rn(\mathbf{r})\right\} = 0 \tag{2.4.18}$$

which is equivalent to the Euler equation

$$\frac{\delta F[n]}{\delta n(\mathbf{r})} + V_{ext}(\mathbf{r}) = \mu \tag{2.4.19}$$

where $V_{ext}(\mathbf{r})$ is uniquely determined by the ground state density $n(\mathbf{r})$ so that

$$\int n(\mathbf{r})d^3r = N \quad \text{and} \quad \int|\nabla n^{1/2}(\mathbf{r})|^2d^3r < \infty. \tag{2.4.20}$$

The constrained search formulation has introduced the concept of $N-representable$. In addition, the restriction to non-degenerate ground states of the original Hohenberg-Kohn theorem is lifted and the restriction requiring no degeneracy has also been removed.

2.4.3 Kohn-Sham equation. We are now able to determine the density $n(\mathbf{r})$ and all properties of the ground state of any system by searching the minimum energy of the many electron system, which can be expressed in the form of the density and can be written as:

$$E[n] = F[n] + \int n(\mathbf{r})v(\mathbf{r})d^3r \tag{2.4.21}$$

where

$$F[n] = T[n] + V_{ee}[n], \tag{2.4.22}$$

where $T[n]$ is the interacting kinetic energy functional and $V_{ee}[n]$ the Coulomb interaction energy functional. The density that minimizes the energy can be found from the Euler-Lagrange equation

$$\frac{\delta F[n]}{\delta n(\mathbf{r})} + v(\mathbf{r}) = \mu, \tag{2.4.23}$$

where μ is the Euler-Lagrange multiplier associated with the constraint

$$\int n(\mathbf{r}) d^3r = N. \tag{2.4.24}$$

The formulation of Kohn-Sham (KS) is to replace the interacting system with a fictitious non-interacting system with the same ground state density and where each electron moves in the same external potential [27]. Let $\mathcal{H}_s$ denote the Hamiltonian of the non-interacting with the same ground state density $n(\mathbf{r})$ than the interacting system and $v_s(\mathbf{r})$ the external potential. The wave functions Φ_i satisfy the following Schrödinger equation:

$$\hat{\mathcal{H}}_s \Phi_i = \epsilon_i \Phi_i \tag{2.4.25}$$

so

$$\left(-\frac{1}{2}\nabla^2 + v_s(\mathbf{r}) \right) \Phi_i = \epsilon_i \Phi_i. \tag{2.4.26}$$

The density is defined as

$$n(\mathbf{r}) = \sum_i^N |\Phi_i|^2 \tag{2.4.27}$$

and

$$T_s[n] = \sum_i^N \langle \Phi_i | -\frac{1}{2}\nabla^2 | \Phi_i \rangle. \tag{2.4.28}$$

Here s represents single electron and $T_s[n]$ is the kinetic energy of the non-interacting system usually called the Kohn-Sham kinetic energy. The Euler-Lagrange that describes these equations is given by

$$\frac{\delta T_s[n]}{\delta n(\mathbf{r})} + v_s(\mathbf{r}) = \mu \tag{2.4.29}$$

Since the functional $F[n]$ and the Kohn-Sham kinetic energy $T_s[n]$ are defined only for the ground state density, we can write the functional as a large part $T_s[n]$ and the Hartree energy as

$$F[n] = T_s[n] + \int \frac{n(\mathbf{r}) n(\mathbf{r}')}{|\mathbf{r} - \mathbf{r}|} d^3r d^3r' + E_{xc}[n] \tag{2.4.30}$$

where

$$E_{xc}[n] = T[n] - T_s[n] - \int \frac{n(\mathbf{r}) n(\mathbf{r}')}{|\mathbf{r} - \mathbf{r}'|} d^3r d^3r' + V_{ee}[n]. \tag{2.4.31}$$

$E_{xc}[n]$ is called the exchange correlation energy and is the functional which contains everything that is unknown, which we do not know how to handle exactly [28], thus must be approximated. Substituting Equation (2.4.30) into Equation (2.4.23) and comparing with (2.4.29), we obtain

$$v_s(\mathbf{r}) = v(\mathbf{r}) + \frac{\delta}{\delta n(\mathbf{r})}\left[\int \frac{n(\mathbf{r})n(\mathbf{r}')}{|\mathbf{r}-\mathbf{r}'|}d^3r d^3r'\right] + \frac{\delta E_{xc}[n]}{\delta n(\mathbf{r})} \tag{2.4.32}$$

then

$$v_s(\mathbf{r}) = v(\mathbf{r}) + \int \frac{n(\mathbf{r}')}{|\mathbf{r}-\mathbf{r}'|}d^3r' + v_{xc}(\mathbf{r}) \tag{2.4.33}$$

with the exchange correlation potential

$$v_{xc}(\mathbf{r}) = \frac{\delta E_{xc}[n]}{\delta n(\mathbf{r})}. \tag{2.4.34}$$

We find that the ground state density can be obtained by solving the non-interacting system of Kohn-Sham equation which is given by

$$\left[-\frac{1}{2}\nabla^2 + v(\mathbf{r}) + \int \frac{n(\mathbf{r}')}{|\mathbf{r}-\mathbf{r}'|}d^3r' + v_{xc}(\mathbf{r})\right]\Phi_i(\mathbf{r}) = \epsilon_i\Phi_i(\mathbf{r}). \tag{2.4.35}$$

The problem of finding the universal functional in the many particle interacting system has been reduced to a non-interacting system by introducing the exchange correlation energy $E_{xc}[n]$. The Kohn-Sham equations determine the exact density and energy of the ground state of a many-body electrons using the non-interacting system approach. In practice, we will solve the Kohn-Sham equations self-consistently, by diagonalizing the Hamiltonian matrix and iterating on the charge density (or potential) until self-consistency is achieved. Indeed we will consider the charge density (or potential $v_s(\mathbf{r})$) as the quantity to be determined self-consistently. We start by supplying an input charge density $n_{in}(\mathbf{r})$ to the Kohn-Sham equations and we get an output charge density $n_{out}(\mathbf{r})$, hence we define a functional A as

$$n_{out}(\mathbf{r}) = A[n_{in}(\mathbf{r})]. \tag{2.4.36}$$

At self consistency,

$$n(\mathbf{r}) = A[n(\mathbf{r})]. \tag{2.4.37}$$

In the following, the first algorithm use $n_{out}(\mathbf{r})$ as the new input charge density:

$$n_{in}^{(i+1)} = n_{out}^{(i)}. \tag{2.4.38}$$

where i is the iteration number. Since the algorithm works only for a smaller error on the output than the error on input, we consider an error $\delta n^{in}(\mathbf{r})$ on input, the error on output, close to self-consistency, will be

$$\delta n_{out}(\mathbf{r}) \simeq \int \frac{\delta A}{\delta n(\mathbf{r})}\delta n_{in}(\mathbf{r})d\mathbf{r} \equiv J\delta n_{in} \tag{2.4.39}$$

There is no guarantee the output error is smaller than the input error, this assumption depends on the size of the largest eigenvalue, e_J, of the operator J, which is related to the dielectric response of the

system. For $e_J > 1$ the iteration does not converge. The algorithm which leads to the converge is obtained by defining a new input charge density generated by mixing the input and output charges:

$$n_{in}^{(i+1)} = (1-\alpha)n_{in}^{i} + \alpha n_{out}^{i}. \tag{2.4.40}$$

At any step of iteration we can define the deviation from the correct density as

$$\delta n \equiv n - n_{KS}, \tag{2.4.41}$$

then near the solution, the error in output density is given by

$$\delta n_{out}[n_{in}] = n_{out} - n_{KS} = (\tilde{\chi}+1)(n^{in} - n_{KS}), \tag{2.4.42}$$

where

$$\tilde{\chi} + 1 = \frac{\delta n_{out}}{\delta n_{in}}. \tag{2.4.43}$$

Here the function $\tilde{\chi}$ is called a response function and can be calculated. The best choice for the new density would make the error zero, i.e, $n_{in}^{i+1} = n_{KS}$ and if $\tilde{\chi}$ is known, then (2.4.42) can be solved for n_{KS},

$$n_{KS} = n_{in}^{i} - \tilde{\chi}^{-1}(n_{i}^{out} - n_{in}^{i}) \tag{2.4.44}$$

Equation (2.4.44) is not exact but gives the best input for the next iteration. If it were exact, this would be the answer and the iterations could stop. The response kernel $\tilde{\chi}$ is very demanding to calculate since it costs many iterations, it can be more efficient to consider $\tilde{\chi}$ as a Jocobian J (the second derivative matrix) of the system [19].

2.5 Functional for exchange and correlation

The crucial quantity in the Kohn-Sham approach is the exchange-correlation energy which is expressed as a functional of the density $E_{xc}[n]$. In this section we present relevant approximate functionals, in particular the local density approximation (LDA), and generalized gradient approximation (GGA).

2.5.1 Local density approximation. Within the Kohn-Sham equation the exchange correlation energy is unknown, the greatest challenge in density functional theory is to find an accurate $E_{xc}[n]$. The most commonly used and successful approximation for calculating $E_{xc}[n]$ is the local density approximation (LDA). This approximation assumes that the density varies slowly. It replaces the exchange and correlation potential at each point of space by an uniform interacting electron gas. The exchange correlation energy can be expressed as:

$$E_{xc}^{LDA}[n] = \int d^3r n(\mathbf{r}) \epsilon_{xc}^{unif}(n), \tag{2.5.1}$$

where $\epsilon_{xc}^{unif}(n)$ is the exchange correlation energy per particle of uniform electron gas of density n.The corresponding exchange correlation potential to (2.4.34) is

$$v_{xc}^{LDA}(\mathbf{r}) = \frac{\delta E_{xc}^{LDA}[n]}{\delta n(\mathbf{r})} = \left[\epsilon_{xc}^{unif} + n\frac{\partial \epsilon_{xc}^{unif}}{\partial n}\right]_{\mathbf{r}}. \tag{2.5.2}$$

The function ϵ_{xc}^{unif} can divided into two parts so that:

$$\epsilon_{xc}^{unif}(n) = \epsilon_{x}^{unif}(n) + \epsilon_{c}^{unif}(n), \tag{2.5.3}$$

where $\epsilon_{x}^{unif}(n)$ is the exchange. The accurate value of the exchange part is known from the Dirac exchange energy [29] and given by

$$\epsilon_{x}^{unif}(n) = -\frac{3}{4}\left(\frac{3}{\pi}\right)^{1/3} n^{1/3} = -\frac{3}{4}\left(\frac{9}{4\pi^2}\right)^{1/3}\frac{1}{r_s} = -\frac{0.458}{r_s} a.u., \tag{2.5.4}$$

where $r_s = (3/4\pi n)^{1/3}$ is the mean interelectronic distance expressed in atomic units (a.u.).
Several approximations for correlation part are also available [30]. The most accurate results available have been calculated by Ceperley and Alder using the quantum Monte Carlo method in 1980 [31]. This correlation part has been parameterized by Perdew and Zunger (1981) for a spin-polarized (P) and spin-unpolarized (U) uniform electron gas. For the spin polarized electron gas the paramatrized expression is of the form

$$\epsilon_{c}^{P}(n) = \begin{cases} A\ln r_s + B + Cr_s \ln r_s + Dr_s, & r_s \leq 1, \\ \gamma/(1+\beta_1\sqrt{r_s} + \beta_2 r_s), & r_s > 1. \end{cases}$$

For $r_s \leq 1$ the above expression derives from the random phase approximation, and has been calculated by Gell-Mann and Brueckner (1957). This is valid in the limit of very dense electronic systems, and fixes the values of the leading coefficents: $A^U = 0.0311. B^U = -0.048$. The relations given by Misawa in 1965 allows us to obtain the values for the fully polarized gas: $A^P = 0.015555, B^P = -0.0269$ and the remaining coefficients have been fitted to the quantum Monte Carlo results of Ceperley and Alder (1980): $C^U = 0.002, D^U = -0.0116$, and $C^P = 0.0007, D^P = -0.0048$. The numerical values of the fitted coefficients of Perdew and Zunger are: $\gamma^U = -0.1423, \beta_1^U = 1.0529, \beta_2^U = 0.3334$ for unpolarized gas, and $\gamma^P = -0.0843, \beta_1^P = 1.3981, \beta_2^P = 0.2611$ for full polarized electron gas [25].
Another parameterization is the one proposed by Vosko et al (1980),

$$\begin{aligned} \frac{\epsilon_c^{VWN}(r_s)}{A} &= \ln\left(\frac{r_s}{F(\sqrt{r_s})}\right) + \frac{2b}{\sqrt{4c-b^2}}\tan^{-1}\left(\frac{\sqrt{4c-b^2}}{2\sqrt{r_s}+b}\right) \\ &- \frac{bx_0}{F(x_0)}\left[\ln\left(\frac{\sqrt{r_s}-x_0}{F(\sqrt{r_s})}\right) + \left(\frac{\sqrt{4c-b^2}}{2\sqrt{r_s}+b}\right)\frac{2(b-2x_0)}{\sqrt{4c-b^2}}\tan^{-1}\left(\frac{\sqrt{4c-b^2}}{2\sqrt{r_s}+b}\right)\right] \end{aligned} \tag{2.5.5}$$

where $F(x) = x^2 + bx + c$, and A, b, c and x_0 are fitting coefficients that differ for the spin polarized and spin unpolarized cases.
The local density approximation predicts very accurately the physical properties of many systems. LDA does not work for system where the density has strong spatial variations or for weakly interacting systems such as van der Waals bonded molecules. It usually overestimates atomization energy, it overestimates correlation and underestimates exchange.

2.5.2 Local spin density approximation. Local spin density approximation (LSDA) is the extension of the LDA to the spin polarized cases and it is based on the spin interpolation proposed by Von Barth

and Hedin [30] and by Vosko, Wills, and Nusair [32]. The idea of the LSDA is to replace the exchange correlation energy density with a spin polarized expression:

$$E_{xc}^{LSDA}[n_\uparrow(\mathbf{r}), n_\downarrow(\mathbf{r})] = \int (n_\uparrow(\mathbf{r}) + n_\downarrow(\mathbf{r}))\epsilon_{xc}^{unif}[n_\uparrow(\mathbf{r}), n_\downarrow(\mathbf{r})]d^3r \tag{2.5.6}$$

$$= \int n(\mathbf{r})\epsilon_{xc}^{unif}[n(\mathbf{r}), \zeta(\mathbf{r})]d^3r. \tag{2.5.7}$$

where $\zeta(\mathbf{r})$ is the magnetization density. As for the LDA, the LSDA exchange correlation energy can be divided into two pieces the exchange energy and the correlation energy so that the exchange energy is given by

$$E_x^{LSDA}[n_\uparrow, n_\downarrow] = \frac{1}{2}C_x \int [(1+\zeta)^{4/3} + (1-\zeta)^{4/3}] \tag{2.5.8}$$

$$= \int n\epsilon_x(n, \zeta)d^3r \tag{2.5.9}$$

where

$$\epsilon_x(n, \zeta) = \epsilon_x^0 + [\epsilon_x^1(n) - \epsilon_x^0(n)]f(\zeta). \tag{2.5.10}$$

The contribution for the exchange density for the spin compensated (paramagnetic) and for spin completely polarized (ferromagnetic) for uniform electron gas are respectively

$$\epsilon_x^0(n) = \epsilon_x(n, 0) = C_x n^{1/3} \tag{2.5.11}$$

and

$$\epsilon_x^1(n) = \epsilon_x(n, 1) = 2^{1/3}C_x n^{1/3} \tag{2.5.12}$$

where $C_x = \frac{3}{4}\left(\frac{3}{4}\right)^{1/3}$ and $f(\zeta)$ has been proposed by Von Barth and Hedin (1972) as

$$f(\zeta) = \frac{(1+\zeta)^{4/3} + (1-\zeta)^{4/3} - 2}{2^{4/3} - 2}. \tag{2.5.13}$$

Many workers have been proposed for LSDA correlation energy (Von Barth and Hedin 1972, Gunnarsson and Lundqvist 1976). The most realistic formula for correlation was proposed by Vosko et al. (1980), based on the random phase approximation (RPA) so

$$E_c^{LSDA}[n_\uparrow(\mathbf{r}), n_\downarrow(\mathbf{r})] = \epsilon_c^U[n] + \left(\frac{f(\zeta)}{f''(0)}\right)[1-\zeta]\epsilon_c^A[n] + f(\zeta)\zeta^4(\epsilon_c^P[n] - \epsilon_c^U[n]), \tag{2.5.14}$$

where $\epsilon_c^U[n]$ and $\epsilon_c^U[n]$ are the correlation energy densities for the unpolarized and fully polarized uniform gas, and $\epsilon_c^A[n]$ has the same expression as the former, but different fitting coefficients.

2.5.3 Generalized gradient approximation. When the density increases rapidly such as for the molecules, the LDA (LSDA) does not give the good approximation, the improvement of this approximation can be made by considering the gradient of the electron density, and so called the Generalized gradient approximation (GGA) in which the exchange correlation energy can be written as [33]

$$E_{xc}^{GGA}[n_\uparrow, n_\downarrow] = \int d^3r n(\mathbf{r})\epsilon_{xc}^{unif}\left(n_{\uparrow(r)}, n_\downarrow(r), \nabla n_\uparrow(r), \nabla n_\downarrow(r), \ldots\right) \tag{2.5.15}$$

$$= \int d^3r n(\mathbf{r})\epsilon_x^{unif}F_{xc}\left(n_{\uparrow(r)}, n_\downarrow(r), \nabla n_\uparrow(r), \nabla n_\downarrow(r), \ldots\right), \tag{2.5.16}$$

where F_{xc} is dimensionless and depends on the density and ϵ_x^{unif} is the exchange energy of the unpolarized gas. The exchange correlation potential of GGA is obtained by including the derivatives regarding the gradient density so

$$v_{xc}^{GGA}(\mathbf{r}) = \frac{\delta E_{xc}^{GGA}}{\delta n(\mathbf{r})} = \left[\epsilon_{xc} + n\frac{\partial \epsilon_{xc}}{\partial n} - \nabla\left(n\frac{\partial \epsilon_{xc}}{\partial n}\right)\right]_{\mathbf{r}}. \tag{2.5.17}$$

From (2.5.16), there exists differents parameterizations of F_{xc}. The parameterization realized by Perdew, Burke and Enzerhof (PBE) [33] is employed this work. Perdew, Burke, and Ernzerhof (PBE) defined the enhancement factor $F_x(n,\zeta,s)$ over the local exchange in (5.2.10) depends on the density n, magnetization density ζ (including spin), and the dimensioless density gradient $s = |\nabla n(\mathbf{r})|/(2k_F n)$. The factor can be written as

$$F_x(s) = 1 + k - \frac{k}{1 + \mu s^2/k}, \tag{2.5.18}$$

where $\mu = \beta(\pi^2/3) = 0.21951$, $\beta = 0.066725$ and $k = 0.804$. Other authors have proposed the same form, but with values of k and μ fitted empirically to a database of atomization energies . The correlation energy takes the form of

$$E_c^{GGA} = \int n(\mathbf{r})(\epsilon_c^{unif}(n,\zeta) + H[n,\zeta,t])d^3r \tag{2.5.19}$$

with

$$H[n,\zeta,t] = (e^2/a_0)\gamma\phi^3 \ln\left\{1 + \frac{\beta}{\gamma}t^2\left[\frac{1+At^2}{1+At^2+A^2t^4}\right]\right\} \tag{2.5.20}$$

where $t = |\nabla(\mathbf{r})|/(2\phi k_s n)$ is the dimensionless density gradient, with $k_s = (4k_F/\pi a_0)$ being the Thomas Fermi screening wave number, and $\phi(\zeta) = [(1+\zeta)^{2/3} + (1-\zeta)^{2/3}]/2$ is a spin scaling factor. Here β has the same value for the exchange term $\beta = 0.066725$, and $\gamma = (1 - \ln 2)/\pi^2 = 0.031091$. The function A has the form of

$$A = \frac{\beta}{\gamma}\left[\exp\{-\epsilon^{unif}/(\gamma\phi^3 e^2/a_0)\} - 1\right]^{-1}. \tag{2.5.21}$$

The correlation correction term H satisfies the following conditions:

(a) In slowing varying limit ($t \to 0$), H tends to the correct second order gradient expansion as

$$H \to (e^2/a_0)\beta\phi^3 t^2, \tag{2.5.22}$$

(b) In the rapidly varying limit ($t \to \infty$), H approaches the uniform electron gas correlation so

$$H \to -\epsilon_c^{unif}, \tag{2.5.23}$$

(c) H cancels the logarithmic singularity of ϵ_c^{unif} in the high density limit, thus forcing the correlation energy to scale to a constant under uniform scaling of the density so that

$$H \to -\frac{e^2}{a_0}\int d^3r n\gamma\phi^3 \ln\left[1 + \frac{1}{\chi s^2/\phi^2 + (\chi s^2/\phi^2)^2}\right] \tag{2.5.24}$$

where $s = |\nabla n|/2k_f n$ is dimensionless density gradient, and $\chi = (\beta/\gamma)c^2\exp(-\omega/\gamma) \simeq 0.72161$. The GGA for the exchange energy will be constructed by the following conditions:

(d) Under the uniform density, E_x must satisfy the scaling condition $\zeta = 0$, we obtain

$$E_x^{GGA} = \int d^3r n\epsilon^{unif}(n)F_x(s). \tag{2.5.25}$$

From (2.5.18), it recovers the correct uniform electron gas limit when $F_x(0) = 1$.

(e) The exchange energy obeys the spin scaling relationship

$$E_x[n_\uparrow, n_\downarrow] = (E_x[2n] + E_x[2n])/2. \tag{2.5.26}$$

(f) The LSDA linear response for $(s \to 0)$ is recovered [33], thus

$$F_x(s) \to 1 + \mu s^2. \tag{2.5.27}$$

(g) It satisfies the local Lieb-Oxford bound [34]

$$E_x[n_\uparrow, n_\downarrow] \geq E_{xc}[n_\uparrow, n_\downarrow] \tag{2.5.28}$$

$$\geq -1.679e^2 \int d^3r n^{4/3}. \tag{2.5.29}$$

For $F_x(s) \leq 1.804$ and $k = 0.804$.

2.6 Hybrid functionals

The hybrid functionals are constructed by mixing a fraction Hartree Fock (HF) exact exchange energy and an explicit density functional. The construction is motivated by predicting accurate gaps and accurate total energies [35]. This mixture can be justified by the ab-initio adiabatic connection formula in which the exchange correlation energy can be written as [20, 36]

$$E_{xc} = \int_0^1 U_{xc}^\lambda d\lambda, \tag{2.6.1}$$

where λ is an interelectronic coupling strength parameters, U_{xc}^λ is the exchange correction potential energy at the intermediate coupling strength λ. This integral can be approximated using the mean-value theorem of integration as

$$E_{xc} \simeq \frac{1}{2}\left(U_{xc}^0 + U_{xc}^1\right) = \frac{1}{2}\left(E_x + U_{xc}^1\right) \tag{2.6.2}$$

with U_{xc}^0 is the exchange correlation potential energies of the Kohn-Sham system and U_{xc}^1 is the exchange correlation potential energy of the full interaction real system. U_{xc}^1 can be similarly approximated as LDA reads

$$U_{xc}^1 \simeq U_{xc}^{LDA} = \int u_{xc}(n(\mathbf{r}))d^3r \tag{2.6.3}$$

The LDA-like functional u_{xc} is derived as an LDA approximation of potential energy [37]. Becke proposed the scheme as a method for incorporating exact exchange into DFT calculation called half-and-half theory so that the exchange correlation energy is given by

$$E_{xc}\frac{1}{2}E_x + \frac{1}{2}U_{xc}^{LDA} \tag{2.6.4}$$

which approximates (2.6.1) with $\lambda = 0$ and LDA for exchange correlation potential energy at $\lambda = 1$. The half-and-half theory is followed by three parameter of Becke such that the exchange correlation energy becomes

$$E_{xc} = E_{xc}^{LDA} + a_0\left(E_x - E_x^{LDA}\right) + a_x\left(E_x^{GGA} - E_x^{LDA}\right) + a_c\left(E_c^{GGA} - E_c^{LDA}\right), \tag{2.6.5}$$

whith a_0 , a_x, and a_c are empirical parameters. Perdew, Ernzerhof and Burke looked at the formula with $a_x = a_c = 1$ for the theoretical motivation which led to the hybrid function regarding the coupling-constant dependence for $a \simeq 0.25$. One of the most popular hybrid is the three parameters B3LYP functionals, mixing 80% of LDA with 20% of HF exchange and adding a certain amount of Becke 's correction ΔE_x^{B88}, the exchange correlation turn out to the following equation [20]

$$E_{xc}^{B3LYP} = 0.8E_x^{LDA} + 0.2E_x^{HF} + 0.72\Delta E_x^{B88} + 0.19E_c^{WN3} + 0.81E_x^{LYP}. \tag{2.6.6}$$

Here 81% of the semi-local Lee-Yang-Parr for correlation energy is used [35], the remaining part 19% of the local correlation energy is added from the Vosko-Wilk-Nusair correlation functional III (VWN3). Apart from B3LYP, several forms of the hybrid method have been proposed such as PBE0 and Heyd-Scuseria-Ernezerhof (HSE) functionals. These functionals differ on how the exact exchange energy is mixed in the energy functional [38]. The Hartree-Fock (HF) exact exchange energy E_x is given by

$$E_x^{HF} = -\frac{e^2}{2}\sum_{ij}\int\int d^3r d^3r' \frac{\phi_i^*(\mathbf{r})\phi_j^*(\mathbf{r}')\phi_i(\mathbf{r}')\phi_j(\mathbf{r})}{|\mathbf{r}-\mathbf{r}'|} \tag{2.6.7}$$

where ϕ_i are the occupied wave functions and i represents a quantum-number set comprising band and k-point indexes. The PBE0 hybrid is constructed by a rational mixing of 25% Fock exchange with 75% of well-know PBE exchange [39], and the exchange correlation energy of PBE0 takes the form of

$$E_{xc}^{PBE0} = \alpha E_x + (1-\alpha)E_x^{PBE} + E_c^{PBE} \tag{2.6.8}$$

Besides HSE has been found to give satisfactory results of energy gap on various solid systems. This is done by splitting the Coulomb operator into short-range (SR) and long-range (LR) parts [38]:

$$\frac{1}{r} = S_\mu(r) + L_\mu(r) = \frac{erfc(\mu r)}{r} + \frac{erf(\mu r)}{r} \tag{2.6.9}$$

then the HF exchange energy in (2.6.1) is calculated by the use of $S_\mu(r)$. The resulting exchange correlation energy of HSE is given as follows

$$E_{xc}^{HSE} = \alpha E_x^{SR}(\mu) + (1-\alpha)E_x^{PBE,SR}(\mu) + E^{PBE,LR}(\mu) + E_c^{PBE}. \tag{2.6.10}$$

In above equations, $r = |\mathbf{r} - \mathbf{r}'|$, and μ is the parameter that defines the range separation related to a characteristic distance $(2/\mu)$ at which the short-range interactions become negligible.

2.7 Van der Waals approximation

In static density functional theory using LDA and GGA, we can describe physical properties of many atoms, molecules and solids with good accuracy, but these approximations fail to describe the long range dispersion interactions, generally denoted as van der Waals interactions. Interaction between the layers of layered molybdenum chalcogenides are dominated by van der Waals-type interactions and are therefore important for this study. We distinguish two directions in the approaches undertaken to overcome this deficiency of DFT. Firstly we present the approach proposed by Grimme which leads to a better description of these interactions [40, 41]. To begin with, there is a term E_{Disp} added to the DFT interaction energy to obtain the total energy as

$$E_{tot} = E_{DFT} + E_{Disp} \tag{2.7.1}$$

where E_{DFT} is the DFT interaction energy computed with an approximate exchange correlation function, and E_{Disp} is the dispersion energy which is defined for periodic system as two-body interaction of the following form

$$E_{Disp} = -s_6 \sum_{i=1}^{N} \sum_{j=i+1}^{N} \frac{C_6^{ij}}{\mathbf{r}_{ij}^6} f(\mathbf{r}_{ij}), \tag{2.7.2}$$

where $-s_6$ is a scaling factor and depends on the DFT used, C_6^{ij} are coefficients of dispersion and $f(\mathbf{r}_{ij})$ is the damping function. The damping function requires the specification of an atom pairwise cuttof radius $\mathbf{R}_r$ which determines in which interatomic distance region the dispersion is decreasing. The damping function can be written as

$$f(\mathbf{r}_{ij}) = \frac{1}{1 + e^{-d(\frac{\mathbf{r}_{ij}}{\mathbf{R}_r - 1})}}. \tag{2.7.3}$$

Here d is a damping parameter.

Secondly the groups of Lundqvist and Langreth have presented a density functional to treat the long-range dispersion. The key is the inclusion of a long range piece of the correlation energy, $E_c^{nl}[n]$ [42, 43], a fully nonlocal functional of the density n. In this functional, the exchange correlation energy takes the form of [44]

$$E_{xc} = E_x^{GGA} + E_c^{LDA} + E^{nl} \tag{2.7.4}$$

where the exchange energy E_x^{GGA} uses the PBE generalized gradient approximation (GGA) functional, and E_c^{LDA} is the local density approximation (LDA) to the correlation energy. E_c^{nl} is the nonlocal energy term defined as

$$E_c^{nl} = \int d^3r \int d^3r' \, \phi(\mathbf{r}, \mathbf{r}') n(\mathbf{r}'). \tag{2.7.5}$$

Here ϕ is called Kernel and is given as a function of $Rf(\mathbf{r})$ and $Rf(\mathbf{r}')$, where $R = |\mathbf{r} - \mathbf{r}'|$ and $f(\mathbf{r})$ is a function of $n(\mathbf{r})$ and its gradient. In fact $f(\mathbf{r})$ is proportional to the exchange correlation energy density ϵ_{xc} of the gradient corrected LDA at the point $\mathbf{r}$ [45].

3. Elastic constants of solids

The elastic constants determine the responses of solids to external forces. They are characterized by the Young's modulus, the Poisson ratio, and the bulk modulus and play an important role in determining the strength and the stability of materials [46]. The knowledge of elastic constant is essential in practical applications related to the mechanical properties of solids: load deflection, thermoelastic stress, stain, fracture toughness [47]. In this part, the description of obtaining elastic constants of solids are carried out in order to further confirm the mechanical stability of molybdenum chalcogenides. We present a discussion of Hooke's law, this law is a basic statement of linear elasticity. A brief review of reduced elastic constants matrices for seven different crystal systems: triclinic, monoclinic, orthorhombic, trigonal, tetragonal, tetragonal, hexagonal and cubic is underlined.

3.1 Generalized Hooke's Law

The elastic properties are described by considering a crystal as a homogeneous continuum medium rather than a periodic array of atoms. In a general case, the problem is formulated as follows:

- When stress σ is applied to the crystal, the crystal is deformed and the parameters which describe it are modified.
- For small deformations, the elastic constants C relate the stress σ and strain ε in the linear relationship, so that $\sigma = C\varepsilon$; this is called Hooke's law.

The theory of obtaining the elastic constants is described as follows: The total energy of a crystal in a strained state can be expressed by the means of a Taylor expansion in the distortion parameters as

$$E = E_0 + V_0 \left(\sum_{ij} \sigma_{ij}\varepsilon_{ij} + \frac{1}{2} \sum_{ijkl} C_{ijkl}\varepsilon_{ij}\varepsilon_{kl} \right) \tag{3.1.1}$$

[48] where E_0 is the total energy of unstrained crystal, V_0 is the volume of the unstrained crystal and E is the corresponding total energy, $\sigma_{ij}\varepsilon_{ij}$ is an element in the distortion tensor and the indices i, j, k, and l run over the x, y, and z. In (3.1.1) σ_{ij} is the tensor of stress defined as

$$\sigma_{ij} = \frac{1}{V_0} \left(\frac{\partial E}{\partial \varepsilon_{ij}} \right), \tag{3.1.2}$$

C_{ijkl} is the tensor of elastic constants derived from second order derivative of E and given by

$$C_{ijkl} = \frac{1}{V_0} \left(\frac{\partial^2 E}{\partial \varepsilon_{ij}} . \varepsilon_{kl} \right)_{\varepsilon=0}. \tag{3.1.3}$$

At equilibrium, i.e. when the energy is a minimum,

$$\left(\frac{\partial E}{\partial \varepsilon_{ij}} \right)_{\varepsilon=0} = 0 \tag{3.1.4}$$

then

$$\sigma_{ij} = \sum_{kl} C_{ijkl}\varepsilon_{kl} \tag{3.1.5}$$

In (3.1.5), elastic constants relate stress and strain in a linear relationship, which is the general form of the Hooke's law. The C_{ijkl} has 81 elastic components. However, due to the symmetry of σ_{ij} and ε_{ij} each of them have 6 independent components. There is a convention to denote these constants called Voigt notation in order to reduce the number of indices [49]. In this notation, the elastic constants are written as C_{ij} where the indices i and j will run over $1, 2, 3, 4, 5$ and 6 so that $1 = xx, 2 = yy, 3 = zz$ define the compression components, and $4 = yz, 5 = zx, 6 = xy$ define shear components.
For example $C_{11} = C_{xxxx}, C_{12} = C_{xxyy} =, C_{44} = C_{yzyz}$.
Therefore, the general form of the Hooke's law is given by

$$\begin{aligned}
\sigma_{xx} &= C_{11}\varepsilon_{xx} + C_{12}\varepsilon_{yy} + C_{13}\varepsilon_{zz} + C_{14}\varepsilon_{yz} + C_{15}\varepsilon_{zx} + C_{16}\varepsilon_{xy},\\
\sigma_{yy} &= C_{21}\varepsilon_{xx} + C_{22}\varepsilon_{yy} + C_{23}\varepsilon_{zz} + C_{24}\varepsilon_{yz} + C_{25}\varepsilon_{zx} + C_{26}\varepsilon_{xy},\\
\sigma_{zz} &= C_{31}\varepsilon_{xx} + C_{32}\varepsilon_{yy} + C_{33}\varepsilon_{zz} + C_{34}\varepsilon_{yz} + C_{35}\varepsilon_{zx} + C_{36}\varepsilon_{xy},\\
\sigma_{yz} &= C_{41}\varepsilon_{xx} + C_{42}\varepsilon_{4y} + C_{23}\varepsilon_{zz} + C_{44}\varepsilon_{yz} + C_{45}\varepsilon_{zx} + C_{46}\varepsilon_{xy},\\
\sigma_{zx} &= C_{51}\varepsilon_{xx} + C_{52}\varepsilon_{yy} + C_{53}\varepsilon_{zz} + C_{54}\varepsilon_{yz} + C_{55}\varepsilon_{zx} + C_{56}\varepsilon_{xy},\\
\sigma_{xy} &= C_{61}\varepsilon_{xx} + C_{62}\varepsilon_{yy} + C_{63}\varepsilon_{zz} + C_{64}\varepsilon_{yz} + C_{65}\varepsilon_{zx} + C_{66}\varepsilon_{xy}.
\end{aligned}$$

Thus, we obtain 36 elastic constants. In matrix form, these elastic constants can be written as

$$\begin{pmatrix}
C_{11} & C_{12} & C_{13} & C_{14} & C_{15} & C_{16}\\
C_{21} & C_{22} & C_{23} & C_{24} & C_{25} & C_{26}\\
C_{31} & C_{32} & C_{33} & C_{34} & C_{35} & C_{36}\\
C_{41} & C_{42} & C_{43} & C_{44} & C_{45} & C_{46}\\
C_{51} & C_{52} & C_{53} & C_{54} & C_{55} & C_{56}\\
C_{61} & C_{62} & C_{63} & C_{64} & C_{65} & C_{66}
\end{pmatrix}$$

For some applications, it is sometimes preferable to express strain in terms of stress. This can be done by inverting (3.1.5) so that

$$\varepsilon_{ij} = S_{ijkl}\sigma_{kl} \tag{3.1.6}$$

where S_{ijkl} is the elastic compliance constants tensor and can be written in full, Equation (3.1.6) becomes

$$\begin{aligned}
\varepsilon_{xx} &= S_{11}\sigma_{xx} + S_{12}\sigma_{yy} + S_{13}\sigma_{zz} + S_{14}\sigma_{yz} + S_{15}\sigma_{zx} + S_{16}\sigma_{xy},\\
\varepsilon_{yy} &= S_{21}\sigma_{xx} + S_{22}\sigma_{yy} + S_{23}\sigma_{zz} + S_{24}\sigma_{yz} + S_{25}\sigma_{zx} + S_{26}\sigma_{xy},\\
\varepsilon_{zz} &= S_{31}\sigma_{xx} + S_{32}\sigma_{yy} + S_{33}\sigma_{zz} + S_{34}\sigma_{yz} + S_{35}\sigma_{zx} + S_{36}\sigma_{xy},\\
\varepsilon_{yz} &= S_{41}\sigma_{xx} + S_{42}\sigma_{yy} + S_{43}\sigma_{zz} + S_{44}\sigma_{yz} + S_{45}\sigma_{zx} + S_{46}\sigma_{xy},\\
\varepsilon_{zx} &= S_{51}\sigma_{xx} + S_{52}\sigma_{yy} + S_{53}\sigma_{zz} + S_{54}\sigma_{yz} + S_{55}\sigma_{zx} + S_{56}\sigma_{xy},\\
\varepsilon_{xy} &= S_{61}\sigma_{xx} + S_{62}\sigma_{yy} + S_{63}\sigma_{zz} + S_{64}\sigma_{yz} + S_{65}\sigma_{zx} + S_{66}\sigma_{xy}.
\end{aligned}$$

For completeness, the elastic compliance constants tensor are given by

$$S_{ij} = \frac{(-1)^{i+j}\Delta^c_{ij}}{\Delta^c}, \tag{3.1.7}$$

where Δ^c is the determinant of the C_{ij} terms, and is the minor obtained by suppressing the i^{th} row and the j^{th} column. Since $C_{ij} = C_{ji}$ it follows that $S_{ij} = S_{ji}$.

3.2 Reduced elastic constant matrices

In three dimensions, there are 32 symmetric point groups that can be subdivided into fourteen Bravais or space lattices. These lattices are further grouped into seven crystal system: triclinic, orthorhombic, monoclinic, tetragonal, trigonal, hexagonal and cubic. The elastic constant components of matrices of these seven crystal systems can be described as follows [50]:
The triclinic has 21 elastic constants

$$\begin{pmatrix} C_{11} & C_{12} & C_{13} & C_{14} & C_{15} & C_{16} \\ 0 & C_{22} & C_{23} & C_{24} & C_{25} & C_{26} \\ 0 & 0 & C_{33} & C_{34} & C_{35} & C_{36} \\ 0 & 0 & 0 & C_{44} & C_{45} & C_{46} \\ 0 & 0 & 0 & 0 & C_{55} & C_{56} \\ 0 & 0 & 0 & 0 & 0 & C_{66} \end{pmatrix}$$

Orthorhombic has nine elastic constants

$$\begin{pmatrix} C_{11} & C_{12} & C_{13} & 0 & 0 & 0 \\ 0 & C_{22} & C_{23} & 0 & 0 & 0 \\ 0 & 0 & C_{33} & 0 & 0 & 0 \\ 0 & 0 & 0 & C_{44} & 0 & 0 \\ 0 & 0 & 0 & 0 & C_{55} & 0 \\ 0 & 0 & 0 & 0 & 0 & C_{66} \end{pmatrix}$$

The monoclinic system has 13 elastic constants

$$\begin{pmatrix} C_{11} & C_{12} & C_{13} & 0 & C_{15} & 0 \\ 0 & C_{22} & C_{23} & 0 & C_{25} & 0 \\ 0 & 0 & C_{33} & 0 & C_{35} & 0 \\ 0 & 0 & 0 & C_{44} & 0 & C_{46} \\ 0 & 0 & 0 & 0 & C_{55} & 0 \\ 0 & 0 & 0 & 0 & 0 & C_{66} \end{pmatrix}$$

The tetragonal system has 7 independent elastic constants

$$\begin{pmatrix} C_{11} & C_{12} & C_{13} & 0 & & C_{16} \\ 0 & C_{11} & C_{13} & 0 & 0 & -C_{16} \\ 0 & 0 & C_{33} & 0 & 0 & 0 \\ 0 & 0 & 0 & C_{44} & 0 & 0 \\ 0 & 0 & 0 & 0 & C_{44} & 0 \\ 0 & 0 & 0 & 0 & 0 & C_{66} \end{pmatrix}$$

The trigonal system has 6 independent elastic constant

$$\begin{pmatrix} C_{11} & C_{12} & C_{13} & C_{14} & -C_{15} & 0 \\ 0 & C_{11} & C_{13} & -C_{14} & C_{25} & 0 \\ 0 & 0 & C_{33} & 0 & 0 & 0 \\ 0 & 0 & 0 & C_{44} & 0 & C_{25} \\ 0 & 0 & 0 & 0 & C_{44} & -C_{14} \\ 0 & 0 & 0 & 0 & 0 & \frac{1}{2}(C_{11} - C_{12}) \end{pmatrix}$$

The hexagonal system has 5 independent elastic constants

$$\begin{pmatrix} C_{11} & C_{12} & C_{13} & 0 & 0 & 0 \\ 0 & C_{11} & C_{13} & 0 & 0 & 0 \\ 0 & 0 & C_{33} & 0 & 0 & 0 \\ 0 & 0 & 0 & C_{44} & 0 & 0 \\ 0 & 0 & 0 & 0 & C_{44} & 0 \\ 0 & 0 & 0 & 0 & 0 & \frac{1}{2}(C_{11} - C_{12}) \end{pmatrix}$$

The cubic system has 3 independent elastic constants

$$\begin{pmatrix} C_{11} & C_{12} & C_{12} & 0 & 0 & 0 \\ 0 & C_{11} & 0 & 0 & 0 & 0 \\ 0 & 0 & C_{11} & 0 & 0 & 0 \\ 0 & 0 & 0 & C_{44} & 0 & 0 \\ 0 & 0 & 0 & 0 & C_{44} & 0 \\ 0 & 0 & 0 & 0 & 0 & C_{44} \end{pmatrix}$$

In summary, all 36 elastic constant are independent. However, in crystals, many of them are the same due to symmetry. As for cubic system, we can see from the matrix $C_{11} = C_{22} = C_{33}$, $C_{12} = C_{21} = C_{23} = C_{32} = C_{13} = C_{31}$, $C_{44} = C_{55} = C_{66} =$ due the fact that x, y and z are identical by symmetry. Also the off diagonal shear are zero, i.e $C_{45} = C_{54} = C_{56} = C_{65} = C_{46} = C_{64} = 0$, and mixed compression/shear coupling does not occur, i.e $C_{14} = C_{41} = \ldots = 0$ [51].

4. Outline of calculations

In this work, the Vienna-ab initio Simulation Package (VASP) [52] has been used to perform the electronic structure calculations. The projector-augmented wave formalism (PAW) implemented in this package were used to represent the valence electrons [53]. The electronic exchange and correlation functions are treated within DFT by using a generalized gradient approximation (GGA) [33], and performed by using the van der Waals approximation proposed by Grimme [40, 41], and Lundqvist and Langreth [42, 43]. We have optimized the kinetic energy cutoff and mesh of k-points by carrying out self-consistent calculations. We have used a kinetic energy cutoff of 520 eV for the plane wave basis set and a Monkhorst-Pack grid of $9 \times 9 \times 2$ for MoX_2 (X = S, Se, Te) in space group $P6_3/mmc$ for Brillouin-zone integrations.

4.1 Vienna Ab-Initio Simulation Package

The viena ab-initio package (VASP) is a plane-wave all-electron code using the pseudopotential or projector augmented wave method (PAW) and plane wave basis set [52]. In order to describe the interaction between ions and electrons fully, VASP uses ultra-soft Vanderbilt pseudopotentials (US-PP) or uses the projector augmented wave (PAW) method. The code uses fast iterative techniques for the diagonalization of DFT Hamiltonian which allows efficient total energy calculations and structural optimizations for systems. VASP calculates forces and stress tensors [52]. VASP is applied in many different areas such as structure and phase stability, mechanical and dynamical properties, liquids, glasses and quasicrystals, magnetism and magnetic nanostructures, semiconductors and insulators, surfaces, interfaces and thin films, chemical reactions, and catalysis [20]. The structural properties within DFT , GW approximation for band structure energy have been applied using various smearing or tetrahedron methods implemented in VASP.

4.2 Equation of state

The equation of state (EOS) of solids describes the relationship between thermodynamic variables of compressed solids, applied in investigating thermodynamic properties of materials [54].
Many, semi-emperical relations have been proposed to describe the EOS [55]. In this work, we are going to use the Murnaghan-Birch equation of state [56]. To begin with, we define the energy of a compressed system as a Taylor series based on the finite strain as

$$E(f) = a + bf + cf^2 + \dots \tag{4.2.1}$$

where f is a finite strain given by

$$f = \frac{1}{2}\left[\left(\frac{V_0}{V}\right)^{2/3} - 1\right]. \tag{4.2.2}$$

The pressure and bulk modulus are respectively define as

$$P = -\frac{\partial E}{\partial f} \cdot \frac{\partial f}{\partial V}, \tag{4.2.3}$$

$$B = -V\left(\frac{\partial P}{\partial f} \cdot \frac{\partial f}{\partial V}\right). \tag{4.2.4}$$

The second order of (4.2.3) gives

$$P = \frac{3B_0}{2}\left[\left(\frac{V_0}{V}\right)^{7/3} - \left(\frac{V_0}{V}\right)^{5/2}\right]. \tag{4.2.5}$$

In above equations V_0 is the equilibrium volume of the system, and B_0 is the isothermal bulk modulus. The third order shows increased accuracy over the Murnaghan equation of state and has a relatively simple analytical form

$$P = \frac{3B_0}{2}\left[\left(\frac{V_0}{V}\right)^{7/3} - \left(\frac{V_0}{V}\right)^{5/3}\right]\left[1 + \frac{3}{4}(B_0^{'} - 4)\left(\left(\frac{V_0}{V}\right)^{2/3} - 1\right)\right]. \tag{4.2.6}$$

Here $B_0^{'}$ is the bulk modulus derivative. The energy is obtained by integration of the pressure

$$E = E_0 + \frac{9V_0B_0}{16}\left\{\left[\left(\frac{V_0}{V}\right)^{2/3} - 1\right]^3 B_0^{'} + \left[\left(\frac{V_0}{V}\right)^{2/3} - 1\right]^2\left[6 - 4\left(\frac{V_0}{V}\right)^{2/3}\right]\right\}. \tag{4.2.7}$$

Using data from the GGA in the PBE parametrization and Van der Waals (Grime, and Langreth and Lundqvist) calculations, we obtain the total energy versus the volume by fitting the third order Murnaghan-Birch EOS, and deduce the ground state properties of the equilibrium lattice constant (a) the ratio (a/c), bulk modulus B_0 and pressure derivative of the bulk modulus ($B_0^{'}$).

4.3 Cohesive energy

The cohesive energy of a solid is defined as the energy required for separating the condensed material into isolated free atoms. For molybdenum chalcogenides $M_mX_n(M_m = Mo_m, X_n = S_n)$, the cohesive energy is given by

$$E_{coh}^{M_mX_n} = \frac{E_{solid}^{M_mX_n} - Z \times (mE_{atom}^{M_m} + nE_{atom}^{X_n})}{Z \times (m+n)}, \tag{4.3.1}$$

where Z is the number of M_mX_n per unit cell, $E_{atom}^{M_m}$ and $E_{atom}^{X_n}$ are the energies of the spin-polarized non-spherical isolated M and X atoms in its electronic ground state. These energies are computed by placing a free atom in a big orthorhombic unit cell.
$E_{solid}^{M_mX_n}$ are the bulk cohesive energies with respect to spherical non spin-polarized reference atoms, and $m, n = 1, 2$ are the stoichiometric weights. The cohesive energy will be obtained from the fit to a Murnaghan-Birch third order equation of state and will be used to deduce the structural parameters and to predict the stability of the structures.

4.4 Formation energy

Apart from the cohesive energy, another measure of relative stability is the formation energy. The formation energy is defined as the heat of formation per atom of the structure under consideration. Let us consider that the solid M_mX_n result from the interaction between the molybdenum (solid) M_m and the gaseouse chalcogenide X_2 through the chemical reaction [57]

$$mM^{solid} + \frac{n}{2}X_2^{solid} \rightleftharpoons M_mX_n^{solid}. \tag{4.4.1}$$

To compare the relative stabilities of the various structures, we define the formation energy as

$$E_f(M_mX_n^{solid}) = E_{coh}(M_mX_n^{solid}) - \frac{mE_{coh}(M^m) + \frac{n}{2}E_{coh}(X_2^{gas})}{m+n} \tag{4.4.2}$$

where $m, n = 1, 2$ are the stoichiometric weights and $E_{coh}(M_mX_n^{solid})$ is the cohesive energy per atom as described in (4.3.1), and $E_{coh}(M^{solid})$ and $E_{coh}(X_2^{gas})$ are the ground state cohesive energy of M^{solid} and X_2^{gas} respectively.

4.5 Electronic Density of state

The response of electrons in a solid to external perturbations such as absorption or emission of light can be elucidated by the energy eigenvalues (band structure). This response is related to the electronic properties (band gap) and optical properties (color, reflectivity, and dielectric response of the solid) [23]. A useful concept in analyzing the band structure of solids is the density of states as a function of the energy [23]. The density of states $N(E)dE$ is defined as the number of states per volume Ω of the solid (for each direction of the electron spin separately) in the range $[E, E+dE]$ [58]. Since the states are characterized by their wave-vector $\mathbf{k}$, and taking into account the usual foctor of 2 for spin degeneracy, it follows that

$$N(E)dE = \frac{1}{\Omega}\sum_{E_{\mathbf{k}}\in[E,E+dE]} 2 = \frac{2}{(2\pi)^3}\int_{E_{\mathbf{k}}\in[E,E+dE]} d\mathbf{k} = \frac{1}{\pi^2}k^2dk \tag{4.5.1}$$

where (4.5.1) has been obtained by the use of the spherical coordinates in $\mathbf{k}$-space. In the free-electron model we get

$$E_{\mathbf{k}} = \frac{\hbar^2|\mathbf{k}|^2}{2m} \Longrightarrow kdk = \frac{m}{\hbar^2}dE, \quad k = \left(\frac{2mE}{\hbar^2}\right)^{1/2}. \tag{4.5.2}$$

These relations give for the density of states in this simple model in 3 D:

$$N(E) = \frac{1}{2\pi^2}\left(\frac{2m}{\hbar^2}\right)^{3/2}\sqrt{E}. \tag{4.5.3}$$

Using the band structure calculation for $E_{\mathbf{k}}$, the density of states becomes

$$\begin{aligned} N(E) &= \frac{1}{\Omega}\sum_{n,\mathbf{k}} 2\delta(E - E_{\mathbf{k}}^{(n)}) = \frac{2}{(2\pi)^3}\sum_n \int \delta(E - E_{\mathbf{k}}^{(n)})d\mathbf{k} \\ &= \frac{2}{(2\pi)^3}\sum_n \int_{E_{\mathbf{k}}^{(n)}=E} \frac{1}{|\nabla_{\mathbf{k}}E_{\mathbf{k}}^{(n)}|}dS_k. \end{aligned} \tag{4.5.4}$$

In (4.6.3) the integral goes over a surface in k- space on which $E_{\mathbf{k}}^{(n)}$ is constant and equals to E, and $S_{\mathbf{k}}$ represents the two-dimensional surface. The energy surfaces are spherical and defined for a free electron model as:

$$|\nabla_{\mathbf{k}} E| = \frac{\hbar^2 k}{m} = \hbar \left(\frac{2E}{m}\right)^{1/2}. \tag{4.5.5}$$

In above equations, the subscript n represents the band index. It is difficult to evaluate (4.6.3) to determine the density of states in most actual problems in band structure calculation. In order to express the contribution of the atoms for layered molybdenum chalcogenides $M_m X_n$ to the total density, we will calculate the projected density of states for each atom.

4.6 Band Gap

In an electronic system, the fundamental band gap is defined as the difference between the ionization energy and electron affinity [59]. However, the well-known band gap problem, in which DFT in LDA and GGA fails to correctly predict the energy gap between occupied and unoccupied states, is a hindrance to research in fields including semiconductors, optical, and photovoltaic materials [60]. Indeed in a DFT calculation, the Kohn-Sham gap E_{gap}^{KS} is defined as the difference between the eigenvalues of lowest unoccupied and highest occupied eigenvalues, but the eigenvalues obtained from Kohn-Sham equation do not have the physical meaning. Typically, E_{gap}^{KS} underestimates band gaps of solids by about 30% up to 100% [61, 62, 63]. For a neutral N electron system the ionization energy is $I = E_{N-1}^{(0)} - E_N^{(0)} \equiv -\epsilon_{HOMO}$, and the electron affinity is $A = E_N^{(0)} - E_{N+1}^{(0)} \equiv -\epsilon_{LUMO}$ so that the gap can be written as

$$E_{gap} = I - A = \epsilon_{LUMO} - \epsilon_{HOMO}, \tag{4.6.1}$$

where HOMO and LUMO are the highest occupied and lowest unoccupied molecular orbitals respectively. We can calculate the band gap E_{gap} using KS-DFT through the expression

$$E_{gap} = \epsilon_{N+1}^{KS}(N+1) - \epsilon_N^{KS}(N) \tag{4.6.2}$$

where $\epsilon_{N+1}^{KS}(N+1)$ is the energy of the highest occupied KS orbital of the $N+1$ electron system, and $\epsilon_N^{KS}(N)$ is the HOMO level of the KS N - particle system.
For the non-interacting system, the band gap can be readily written in terms of its orbital energies as

$$E_{gap}^{KS} = \epsilon_{N+1}^{KS}(N) - \epsilon_N^{KS}(N) \tag{4.6.3}$$

From (4.6.2) and (4.6.3), we get that the exact and KS gaps are related through

$$E_{gap} = (\epsilon_{N+1}^{KS}(N) - \epsilon_N^{KS}(N)) + (\epsilon_{N+1}^{KS}(N+1) - \epsilon_{N+1}^{KS}(N)) = E_{gap}^{KS} + \Delta_{xc}. \tag{4.6.4}$$

Here Δ_{xc} is the difference between the energies of the $(N+1)$-th orbitals of the KS systems that correspond to the neutral and ionized electron system. The addition of an extra electron only induces

an infinitesimal change of the density [64], so Δ_{xc} is the measure of a non-analytical behaviour of the exchange correlation (xc) energy functional to an infinitesimal variation of $n(\mathbf{r})$ [64] so that

$$\Delta_{xc} \simeq \left(\frac{\delta E_{xc}[n]}{\delta n(\mathbf{r})}|_{N+1} - \frac{\delta E_{xc}[n]}{\delta n(\mathbf{r})}|_{N} \right) \tag{4.6.5}$$

which gives

$$\Delta_{xc} = v_{xc}^{(N+1)}(\mathbf{r}) - v_{xc}^{(N)}(\mathbf{r}). \tag{4.6.6}$$

We notice that when N increases, the exchange potential jumps discontinuously by Δ_{xc}.This discontinuity is the consequence of a position independent derivative discontinuity in the exchange correlation potential $v_{xc}(\mathbf{r}) = \frac{\delta E_{xc}}{\delta n(\mathbf{r})}$ when the particle number changes through an integer number [65]. Also this discontinuity is the main cause of the difference between the experimental gaps and those given by LDA or GGA [63]. There is some evidence that this discontinuity is responsible for a large part of the band gap problem. In chapter 5, we will see how the energies of adding (removing) an electron to (from) system can be calculated using many-body perturbation theory in the quasiparticle formalism.

4.7 Phenomenological study of the optical functions

The optical properties of solids provide an important tool for studying energy band structure. Observables such as reflectivity, transmission, absorption, can be measured with techniques such as ellipsometry. From these measurements, the dielectric function $\varepsilon(\omega)$, the optical conductivity $\sigma(\omega)$ can be deduced [66]. The optical properties of solids are best represented by the real and imaginary part of the dielectric function ε, which appears in Maxwell's equations,

$$\nabla \times \vec{H} - \frac{1}{c}\frac{\partial \vec{D}}{\partial t} = \frac{4\pi}{c}\vec{j} \tag{4.7.1}$$

$$\nabla \times \vec{E} + \frac{1}{c}\frac{\partial \vec{B}}{\partial t} = 0 \tag{4.7.2}$$

$$\nabla \cdot \vec{D} = 0 \tag{4.7.3}$$

$$\nabla \cdot \vec{B} = 0. \tag{4.7.4}$$

In above equations, we assume that the charge density is zero. The constitutive equations are written as:

$$\vec{D} = \varepsilon \vec{E} \tag{4.7.5}$$

$$\vec{B} = \mu \vec{H} \tag{4.7.6}$$

$$\vec{j} = \sigma \vec{E} \tag{4.7.7}$$

From Maxwell's equations and the constitutive equations, we obtain a wave equation for the field variables $\vec{E}$ and $\vec{H}$

$$\nabla^2 \vec{E} = \frac{\varepsilon\mu}{c^2}\frac{\partial^2 \vec{E}}{\partial t^2} + \frac{4\pi\sigma\mu}{c^2}\frac{\partial \vec{E}}{\partial t} \tag{4.7.8}$$

and

$$\nabla^2 \vec{H} = \frac{\varepsilon\mu}{c^2}\frac{\partial^2 \vec{H}}{\partial t^2} + \frac{4\pi\sigma\mu}{c^2}\frac{\partial \vec{H}}{\partial t}. \tag{4.7.9}$$

For optical fields, we are going to look for a sinusoidal solution to (4.7.8) and (4.7.9)

$$\vec{E} = \vec{E}_0 e^{i(\vec{K}\cdot\vec{r}-\omega t)} \tag{4.7.10}$$

where $\vec{K}$ is a complex propagation constant and ω is the frequency of the light. On substituting (4.7.10) into the wave equation (4.7.8) yields the following relation for K

$$-K^2 = -\frac{\varepsilon\mu\omega^2}{c^2} - \frac{4\pi i\sigma\mu\omega}{c^2}. \tag{4.7.11}$$

If there were no attenuation, K would be equal to

$$K_0 = \frac{\omega}{c}\sqrt{\varepsilon\mu} \tag{4.7.12}$$

and would be real, but since there are losses, K is complex and can written as:

$$K = \frac{\omega}{c}\sqrt{\varepsilon_{complex}\mu} \tag{4.7.13}$$

where we define the dielectric function as:

$$\varepsilon_{complex} = \varepsilon + \frac{4\pi i\sigma}{\omega} = \varepsilon_1 + i\varepsilon_2 \tag{4.7.14}$$

where ε_1 and ε_2 are the real and imaginary parts of $\varepsilon_{complex}$ respectively. From Equation (4.7.14) it follows that

$$\varepsilon_{complex} = \frac{4\pi i}{\omega}\left[\sigma + \frac{\varepsilon\omega}{4\pi i}\right] = \frac{4\pi i}{\omega}\sigma_{complex}. \tag{4.7.15}$$

The complex dielectric function and the complex conductivity can be related to the reflectivity and other properties such as relaxation time, energy band gaps etc.
Indeed, after substitution for K in (4.7.10), the solution equation (4.7.11) to (4.7.9) yields a plane wave

$$\vec{E}(z,t) = \vec{E}_0 e^{-i\omega t}\exp\left(i\frac{\omega z}{c}\sqrt{\varepsilon\mu}\sqrt{1+\frac{4\pi i\sigma}{\varepsilon\omega}}\right). \tag{4.7.16}$$

In vacuum ($\varepsilon = 1, \mu = 1, \sigma = 0$), (4.7.16) reduces to a simple plane wave solution, while for a propagation of the wave in a medium of finite electrical conductivity, the amplitude of the wave exponentially decays over a characteristic distance δ given by

$$\delta = \frac{c}{\omega\tilde{N}_2(\omega)} = \frac{c}{\omega\tilde{k}(\omega)} \tag{4.7.17}$$

where δ is called the optical skin depth, and $\tilde{k}$ is the imaginary part of the complex index of refraction thus

$$\tilde{N}(\omega) = \sqrt{\mu\varepsilon_{complex}} = \sqrt{\varepsilon\mu\left(1+\frac{4\pi i\sigma}{\varepsilon\omega}\right)} = \tilde{n}(\omega) + i\tilde{k}(\omega). \tag{4.7.18}$$

The above equation means that the intensity of the electric field, $|E|^2$, falls off to $1/e$ of its value at the surface in a distance

$$\frac{1}{\alpha_{abs}} = \frac{c}{2\omega\tilde{k}(\omega)} \tag{4.7.19}$$

where α_{abs} is the absorption coefficient for the solid at frequency ω.
The complex index of refraction $\tilde{N}_{complex}$ is usually written in terms of its real and imaginary parts as:

$$\tilde{N}_{complex} = \tilde{n} + i\tilde{k} = \tilde{N}1 + i\tilde{N}_2, \tag{4.7.20}$$

where $\tilde{n}$ and $\tilde{k}$ are called the optical constants of the solid, where $\tilde{n}$ is the index of refraction and $\tilde{k}$ is the extinction coefficient. For $\mu = 1$, and with the definition for $\tilde{N}_{complex}$

$$\varepsilon_{complex} = \varepsilon_1 + i\varepsilon_2 = (\tilde{n} + \tilde{k})^2. \tag{4.7.21}$$

Thus

$$\varepsilon_1 = \tilde{n}^2 - \tilde{k}^2 \tag{4.7.22}$$

$$\varepsilon_2 = 2\tilde{n}\tilde{k} \tag{4.7.23}$$

where ϵ_1, ϵ_2, $\tilde{n}$ and $\tilde{k}$ are all frequency dependent.
The reflectivity measurement, by which one measures the ratio $|\mathcal{R}|^2$ of reflected to the incident intensity, is related to the indices of refraction by

$$\mathcal{R} = |\frac{1 - \tilde{N}_{complex}}{1 + \tilde{N}_{complex}}|^2 = \frac{(1-\tilde{n})^2 + \tilde{k}^2}{(1+\tilde{n})^2 + \tilde{k}}. \tag{4.7.24}$$

where the reflectivity $\mathcal{R}$ is a number less than unity.

5. Many-body perturbation theory

The Kohn-Sham approach in DFT provides good results for the ground state properties of many electronic systems, but the Kohn-Sham eigenvalues can not be identified as excitation energies and have no physical meaning, therefore the eigenvalues do not correspond to the energy for adding or removing electrons. However, excited state properties can be accessed by many- body perturbation theory (MBPT) within the GW calculation in which the eigenvalues of Kohn-Sham are used as input. The widely used density function theory (DFT) performs well for the determination of structural properties of many materials but fails when used to calculate gaps of insulators or semiconductors such as molybdenum chalcogenides. Its results underestimate the gaps. In order to obtain physically meaningful gaps we have to go beyond DFT and resort to quasiparticle (QP) concepts. The quasiparticle energies are given by the energy needed to add (remove) an electron from the system and are experimentally accessible from direct or inverse photo-emission experiments. In this part we are going to describe this concept by the many-body perturbation theory (MBPT) [67], introducing Green's function formalism, the self energy concept and the GW approximation.

5.1 Quasiparticle

Many-body perturbation theory (MBPT) in the GW approximation is a method to determine quasiparticle excitations. It is one of the most accurate first principles approaches to describe electronic band gaps of extended systems [9]. Photo-emission spectroscopy can be used to measure the band gap. The direct photo-electron is described when a photon arrives with an energy $\hbar\omega$ and ejects an electron as demonstrated in Figure 2.1 and the kinetic energy E_{kin} is measured. The binding energy of this electron is given by the following difference $\epsilon_i = E_{kin} - \hbar\omega$ [68]. In reality the electrons are correlated though the Coulomb interaction and the ejection of an electron is a many-body process. Therefore the motion of one electron depends on the motion of all other electrons. The single independent particle can be described within the quasiparticle concept. Due to exchange and correlation effects, a Coulomb hole forms around an electron and behaves together with it like a single entity, which is called a quasiparticle. Quasiparticles interact via a weak screened interaction usually denoted by W instead of the strong Coulomb interaction.

5.2 One particle Green's function

In many-body perturbation theory the central quantity is the time ordered Green's function $G(\mathbf{r}t, \mathbf{r}'t')$ which is the probability amplitude for the propagation of an additional electron from $(\mathbf{r}', t')$ to $(\mathbf{r}, t)$ in many electron system. The Green's function contains the information of the excitation energies ϵ_i and the excitation lifetime of the quasiparticle. On considering the ground state energy of the system, the

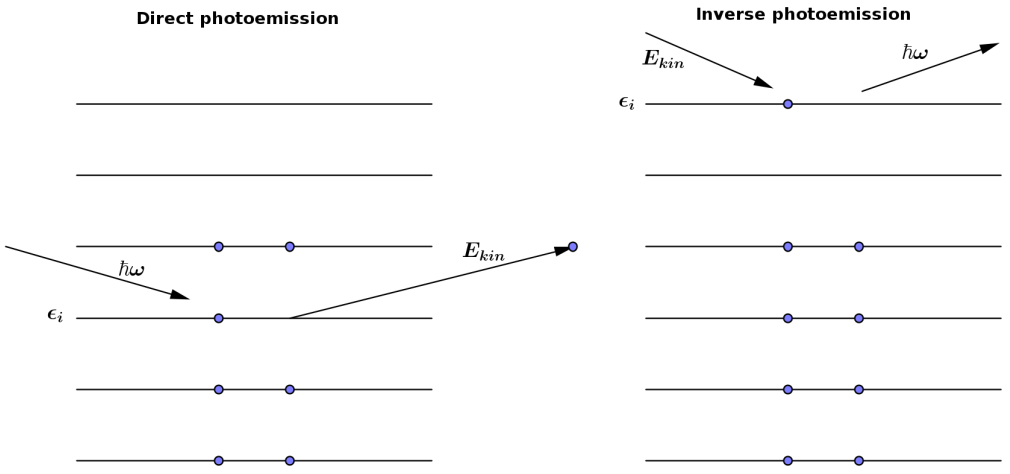


Figure 5.1: Schematic illustration of photoemission. On left the direct photo-electron spectroscopy in which the energy difference $E_{kin} - \hbar\omega$ corresponds to $\epsilon_i = E_0^N - E_i^{N-1}$. On the right the energy difference corresponds to $\epsilon_i = E_i^{N+1} - E_0^N$ in inverse photo-electron spectroscopy.

one particle Green's function particle's function is defined as

$$G(\mathbf{r}t, \mathbf{r}'t') = -\frac{i}{\hbar}\langle \Psi^N(t)|\hat{T}[\hat{\psi}(\mathbf{r}t)\hat{\psi}^\dagger(\mathbf{r}'t')]|\Psi^N(t')\rangle. \tag{5.2.1}$$

Here $\Psi(t)$ is the Heisenberg ground state vector of an N interacting electron system satisfying the Schrödinger equation $\hat{\mathcal{H}}|\Psi_0^N\rangle = E_0^N|\Psi_0^N\rangle$, $\hat{\psi}(\mathbf{r}t)$ and $\hat{\psi}^\dagger(\mathbf{r}'t')$ are the field operators that describe the annihilation and creation of an electron and $\hat{T}$ is the time ordering operator. More explicitly:

$$\hat{\psi}(\mathbf{r}t) = e^{i\hat{\mathcal{H}}t}\hat{\psi}(\mathbf{r})e^{-i\hat{\mathcal{H}}t} \tag{5.2.2}$$

$$\hat{\psi}^\dagger(\mathbf{r}'t') = e^{-i\hat{\mathcal{H}}t'}\hat{\psi}^\dagger(\mathbf{r}')e^{-i\hat{\mathcal{H}}t'}. \tag{5.2.3}$$

The anti-commutation relation gives

$$[\hat{\psi}(\mathbf{r}t), \hat{\psi}^\dagger(\mathbf{r}'t')] = \delta(\mathbf{r} - \mathbf{r}')\delta(t - t') \tag{5.2.4}$$

$$[\hat{\psi}(\mathbf{r}t), \hat{\psi}(\mathbf{r}'t')] = [\hat{\psi}^\dagger(\mathbf{r}t), \hat{\psi}^\dagger(\mathbf{r}'t')] = 0 \tag{5.2.5}$$

and

$$\hat{T}[\hat{\psi}(\mathbf{r}t), \hat{\psi}(\mathbf{r}'t')] = \begin{cases} \hat{\psi}(\mathbf{r}t)\hat{\psi}^\dagger(\mathbf{r}'t') & \text{if} \quad t > t' \\ -\hat{\psi}(\mathbf{r}'t')\hat{\psi}^\dagger(\mathbf{r}t) & \text{if} \quad t < t'. \end{cases} \tag{5.2.6}$$

Let us consider the time-ordered Green's function $G(\mathbf{r}, \mathbf{r}'; \tau)$ of stationary system with $\tau = t - t'$. On introducing the complete set of the eigenstates to the Hamiltonian,for $(N \pm 1)$ particle system, the field operators transform to the Schödinger picture as

$$\psi_i^{N+1}(\mathbf{r}) = \langle \Psi_i^{N-1}|\hat{\psi}(\mathbf{r})|\Psi_0^N\rangle \quad \text{and} \quad \psi_i^{N+1}(\mathbf{r}) = \langle \Psi_0^N|\hat{\psi}(\mathbf{r})|\Psi_i^{N+1}\rangle \tag{5.2.7}$$

with excitation energies

$$\epsilon_i^{N-1} = E_0^N - E_i^{N-1} \quad \text{and} \quad \epsilon_i^{N+1} = E_i^{N+1} - E_0^N. \tag{5.2.8}$$

We obtain

$$\begin{aligned} G(\mathbf{r}, \mathbf{r}^{'}; \tau) = & -\frac{i}{\hbar} \sum_i \psi_i^{N+1}(\mathbf{r}) \psi_i^{N+1^*}(\mathbf{r}^{'}) e^{-i\epsilon_i^{N+1}\tau/\hbar} \delta(\tau) \\ & + \frac{i}{\hbar} \sum_i \psi_i^{N-1}(\mathbf{r}) \psi_i^{N-1^*}(\mathbf{r}^{'}) e^{-i\epsilon_i^{N-1}\tau/\hbar} \delta(-\tau). \end{aligned} \tag{5.2.9}$$

The linear combination of excited sates is defined after adding an electron to the system ($\tau > 0$) so

$$\hat{\psi}^{\dagger}(\mathbf{r}^{'})|\Psi^N\rangle = \sum_i \psi_i^{N+1^*}(\mathbf{r}^{'})|\Psi_i^{N+1}\rangle. \tag{5.2.10}$$

The propagation of an electron (hole) can be analogously defined from (5.2.10) for $\tau < 0$. We can see the Green's function contains the excitation spectrum of the $(N \pm 1)$ particle system. Applying the Fourier transform of $\delta(\tau)$ from (5.2.9), we have

$$\delta(\omega) = \frac{1}{2\pi} \int_{-\infty}^{\infty} \delta(\tau) e^{i\omega\tau - \eta|\tau|} d\tau = \frac{i}{2\pi(\omega + i\eta)}. \tag{5.2.11}$$

Finally the Lehmann representation of the Green's function

$$G(\mathbf{r}^{'}, \mathbf{r}; \omega) = \sum_i \frac{\psi_i^{N+1}(\mathbf{r}) \psi_i^{N+1^*}(\mathbf{r})}{\hbar\omega - (E_i^{N+1} - E_0^N) + i\eta} + \sum_i \frac{\psi_i^{N-1}(\mathbf{r}) \psi_i^{N+1^*}(\mathbf{r})}{\hbar\omega - (E_i^{N-1} - E_0^N) - i\eta} \tag{5.2.12}$$

where $E_i^{(N\pm1)}$ are the energies which correspond to the excitation of an $(N-1)$-particle and $(N+1)$-particle system, i.e. those energies measured in direct and inverse photo-electron emission.
For non-interacting system, the $\psi_i^{N+1}(\mathbf{r})$ and $\psi_i^{N-1}(\mathbf{r})$ are the unoccupied and the occupied single-particle wave function respectively. The quantity $\pm i\eta$ are required to ensure the convergence of the Fourier transformation. The superscript $(N \pm 1)$ are used to avoid overloading the notation. The (fundamental) band gap is the minimum difference between the energies for adding and subtracting an electron. In a many-body system, if the ground state has N electrons, the fundamental gap is

$$E_{gap} = (E^{N-1} - E_0^N) - (E_0^N - E^{N+1}). \tag{5.2.13}$$

Correspondingly, $E^{N\pm1}$ denote the energies of the electron addition (removal) state with the lowest (highest) energy and E_0^N represents the ground-state energy.

5.3 Self energy in GWA

The self energy $\sum$ is described by the interaction effects on the excitation energy and contains the electron exchange and large part of electron correlation. Also in an interacting system the Green's function obeys to the Dyson equation

$$G(\mathbf{r}_1, \mathbf{r}_2) = G_H(\mathbf{r}_1, \mathbf{r}_2) + \int G_H(\mathbf{r}_1, \mathbf{r}_3) \sum(\mathbf{r}_3, \mathbf{r}_4) G(\mathbf{r}_4, \mathbf{r}_2) d\mathbf{r}_3 d\mathbf{r}_4 \tag{5.3.1}$$

where G_H is the Hartree Green's function of the non-interacting system, and is a solution of equation

$$[\omega - \hat{h}_0(\mathbf{r}_1)]G(\mathbf{r}_1, \mathbf{r}_2; \omega) = \delta(\mathbf{r}_1 - \mathbf{r}_2) \tag{5.3.2}$$

with $\hat{h}_0(\mathbf{r})$ the one electron Hamiltonian given by

$$\hat{h}_0(\mathbf{r}) = -\frac{1}{2}\nabla^2_{\mathbf{r}} + V_{ext}(\mathbf{r}) + V_H(\mathbf{r}). \tag{5.3.3}$$

We can see from (5.3.1) and (5.3.2) that the operator $\sum$ contains the exchange and correlation many body effects:

$$[\omega - \hat{h}_0(\mathbf{r}_1)]G(\mathbf{r}_1, \mathbf{r}_2; \omega) = \delta(\mathbf{r}_1 - \mathbf{r}_2) + \int d^3r \sum(\mathbf{r}_1, \mathbf{r}; \omega)G(\mathbf{r}, \mathbf{r}_2; \omega). \tag{5.3.4}$$

Expressing the Green's function G in terms of the wave function $\psi_n(\mathbf{r})$ and energies E_n we obtain

$$G(\mathbf{r}_1, \mathbf{r}_2; \omega) = \sum_n \frac{\psi_n(\mathbf{r}_1)\psi^*_n(\mathbf{r}_2)}{\omega - E_n}. \tag{5.3.5}$$

The latter wave function $\psi_n(\mathbf{r})$ and energies E_n are solutions of the equation

$$\hat{h}_0(\mathbf{r})\psi_n(\mathbf{r}) + \int d^3r' \sum(\mathbf{r}, \mathbf{r}'; \omega)\psi_n(\mathbf{r}') = E_n\psi_n(\mathbf{r}). \tag{5.3.6}$$

Since the self energy $\sum$ takes all dynamic many electron processes into account, the wave function $\psi_n(\mathbf{r})$ and the energies E_n must not be taken as single particle quantities. In general E_n is complex and the imaginary part gives the lifetime of the excitation. If the lifetime of the quasiparticle is finite, the real part of E_n corresponds to the energy of the quasiparticle $E_n = E^{QP}_n$; we arrive at the quasiparticle equation:

$$\hat{h}_0(\mathbf{r})\psi^{QP}_n(\mathbf{r}) + \int d^3r' \sum(\mathbf{r}, \mathbf{r}'; E^{QP}_n)\psi^{QP}_n(\mathbf{r}') = E^{QP}_n\psi^{QP}_n(\mathbf{r}). \tag{5.3.7}$$

The energies E^{QP} appear in a Schrödinger like equation containing the self energy $\sum$ in place of exchange correlation potential [69]. The self energy contribution to the quasiparticle energy is obtained by the Fourier transformation as:

$$\sum(\mathbf{r}, \mathbf{r}'; \omega) = \frac{i\hbar}{2\pi} \int G(\mathbf{r}, \mathbf{r}'; \omega + \omega')W(\mathbf{r}, \mathbf{r}'; \omega')e^{i\omega' i\delta}d\omega' \tag{5.3.8}$$

In (5.3.8), the function at left is the Green's function of the non-interacting system, the second function at right is the screened interaction $W(\mathbf{r}, \mathbf{r}'; \omega')$ and δ is an infinitesimal number. The Green's function can be expressed in terms of the quasiparticle (QP) wave function as

$$G(\mathbf{r}, \mathbf{r}'; \omega) = \sum_n \frac{\psi^{QP}_n(\mathbf{r})\psi^{QP}_n(\mathbf{r}')}{\omega - E^{QP}_n(\omega) - i\delta_n} \tag{5.3.9}$$

where δ_n corresponds to the lifetime of the excitation which is the imaginary part of E_n in (5.3.5). The quasiparticle energy is calculated to the first order which leads to

$$E^{QP} = Re[\langle\psi^{QP}_n|\hat{h}_0 + \sum(E^{QP}_n)|\psi^{QP}_n\rangle]. \tag{5.3.10}$$

Since (5.3.10) requires the value of E_n^{QP}, the equation must be solved by iteration. On using the Newton Raphson method we obtain

$$E_n^{QP} \leftarrow E_n^{QP} + Z_i Re[\psi_n|\hat{h}_0 + \sum(E_n^{QP})|\psi_n\rangle - E_n^{QP}] \tag{5.3.11}$$

which gives the next iteration the energies E_n^N from the quasiparticle as

$$E_n^{N+1} = E_n^N + Z_i Re[\psi_n^{QP}|\hat{h}_0 + \sum(E_n^{QP})|\psi_n^{QP} - E_n^N] \tag{5.3.12}$$

where Z_n is the normalization factor given by

$$Z_n = \left(1 - Re\langle\psi_n^{QP}|(\frac{\partial}{\partial\omega}\sum(\omega)|_{E_n^{QP}})|\psi_n^{QP}\right)^{-1}. \tag{5.3.13}$$

The iteration usually starts from the DFT eigenvalues ϵ_i. The QP energies must be calculated using a single iteration i.e., (5.3.11) should start from $E_n^{QP} = \epsilon_i$, this is referred to the first order perturbation theory.

5.4 Hedin's equations

We saw that the energy of the quasiparticle can be calculated from (5.3.11). Indeed this task can be solved by the use of the many body perturbation theory through the Hedin's equations which link the self energy $\sum$ with the screened Coulomb potential W, the single particle operator G and the vertex function Γ as a perturbation series like in a set of five Dyson equations

$$\sum(1,2) = i\int G(1,4)W(1^+,3)\Gamma(4,2;3)d(3,4) \tag{5.4.1}$$

$$W(1,2) = V(1,2) + \int W(1,3)P(3,4)V(4,2)d(3,4) \tag{5.4.2}$$

$$G(1,2) = G^0(1,2) + \int d(3,4)G_0(1,3)\sum(3,4)G(4,2) \tag{5.4.3}$$

$$\Gamma(1,2,3) = \delta(1,2)\delta(1,3) + \int d(4,5,6,7)\frac{\partial\sum(1,2)}{\partial G((4,5)}G(4,6)G(7,5)\Gamma(6,7,3) \tag{5.4.4}$$

$$P(1,2) = -i\int G(2,3)G(4,2)\Gamma(3,4;1)d(3,4) \tag{5.4.5}$$

with above definition, $1^+ = (\mathbf{r}_1 t_1 + \delta)$, $\delta > 0$ is infinitesimal number, $V(1,2)$ is the bare Coulomb interaction, P is the irreducible polarization function defined as the variation of induced density of the a classical potential (external+Hartree) and Γ is the vertex function given by the variation of the inverse Green's function with respect to a change in the total potential and G^0 coincide with the Hartree Green's function (see (5.3.1)).

5.5 GW approximation

The GW approximation (GWA) corresponds to the first iteration of the Hedin's equations. It sets the vertex function to unity and starts for $\sum = 0$ which leads to the random phase approximation level

(RPA) for screened interaction W and subsequently to $\sum = GW^{RPA}$. In principle, GWA requires a self-consistent determination of P and $\sum$ by setting $G = G_{KS}$ in (5.3.9). Thus

$$G_{KS} = \sum_n \frac{\Phi_n^{KS}(\mathbf{r})\Phi_n^{KS}(\mathbf{r}')}{\omega - \epsilon_n^{KS}(\omega) - i\delta_n}. \tag{5.5.1}$$

On considering $\sum = 0$ in (5.4.4), we get $\Gamma(1,2;3) = \delta(1,2)\delta(1,3)$, $P^0 = -G^0(1,2)G(2,1^+)$ in this case P^0 corresponds to the polarizability which leads to the random phase approximation (RPA), therefore the Hedin's equations are reduced to

$$P^0(1,2) = -iG^0(1,2)G^0(2,1^+) \tag{5.5.2}$$

$$W^0(1,2) = V(1,2) + \int d(3,4)W^0(1,3)P^0(3,4)V(4,2) \tag{5.5.3}$$

$$\sum(1,2) = iG^0(1,2)W^0(1^+,2). \tag{5.5.4}$$

The single particle Green's function G is determined when the $\sum$ updates the quasiparticle wave functions and energies in considering the Green's function of the non-interacting KS system. The screened interaction W can be calculated by the use of the dielectric matrix (see section 4.6).

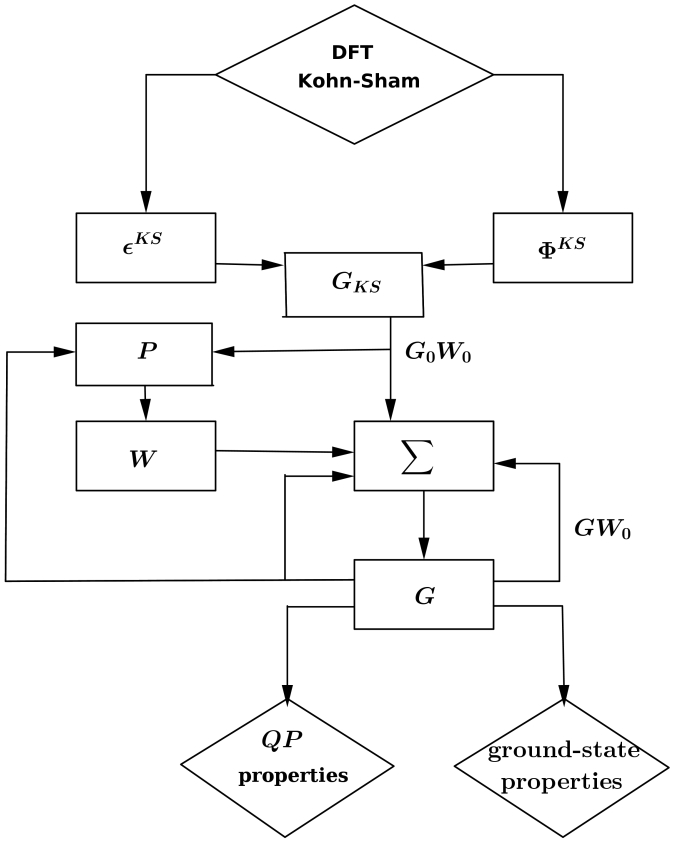


Figure 5.2: This diagram is a sketch of the self-consistent in GW method. In the partially self-consitent GW_0 approximation only G is updated while in the fully self-consistent GW approximation both G and W are updated.

We expand to first order Taylor series the self energy (5.5.4) around the KS eigenvalues:

$$\langle\sum(E_i^{QP})\rangle \simeq \langle\sum(\epsilon_i^{KS})\rangle + \langle\frac{\partial\sum(\omega)}{\partial\omega}|_{\omega=\epsilon_i^{KS}}\rangle(E_i^{QP}-\epsilon_i^{KS}). \tag{5.5.5}$$

In the first order perturbation theory the quasiparticle energies give:

$$E_i^{QP} = \epsilon_i^{KS} + \frac{\sum\langle(\epsilon_i^{KS})\rangle - \langle v_{xc}^{LDA}\rangle}{1-\langle\frac{\partial\sum(\omega)}{\partial\omega}|_{\omega=\epsilon_i^{KS}}\rangle}. \tag{5.5.6}$$

The quasiparticle energies are related to the KS energies when an electron is added or subtracted in the system. If the electron's momentum is well defined in an infinite, periodic solid system, the quasiparticle energies can be written as functions in terms of that momentum. These functions are known as the band structure of the solid [69]. Several calculations have been done using GW approximation and agree with the experiments

5.6 Dielectric matrix and Polarizability

Let $\varepsilon_{\mathbf{q}}^{-1}$ be the inverse of the dielectric matrix in a solid. The screened interaction W is determined by multiplying the bare Coulomb kernel with the inverse dielectric matrix:

$$W_{\mathbf{q}}(\mathbf{G},\mathbf{G}',\omega) = 4\pi e^2\frac{1}{|\mathbf{q}+\mathbf{G}|}\varepsilon_{\mathbf{q}}^{-1}(\mathbf{G},\mathbf{G}',\omega)\frac{1}{|\mathbf{q}+\mathbf{G}'|}. \tag{5.6.1}$$

In (5.6.1) $\mathbf{G}$ and $\mathbf{G}'$ are the reciprocal lattice vectors, and $\mathbf{q}$ is a Bloch wave vector. The inverse of the dielectric matrix $\varepsilon_{\mathbf{q}}^{-1}(\mathbf{G},\mathbf{G},\omega)$ represents the screening in a solid when local fields due to density inhomogeneities and many-body effects are taken into account [70]. The dielectric matrix is calculated from the random phase approximation (RPA) as

$$\varepsilon_{\mathbf{q}}(\mathbf{G},\mathbf{G}',\omega) = \delta_{\mathbf{G},\mathbf{G}'} - \frac{4\pi e^2}{|\mathbf{q}+\mathbf{G}||\mathbf{q}+\mathbf{G}'|}\chi_{\mathbf{q}}^0(\mathbf{G},\mathbf{G}',\omega), \tag{5.6.2}$$

where $\chi_{\mathbf{q}}^0(\mathbf{G},\mathbf{G}',\omega)$ is the independent particle polarizability. The dielectric function $\varepsilon_{\mathbf{q}}^{-1}(\mathbf{G},\mathbf{G},\omega)$ is a microscopic quantity. Therefore, spatial averages have to be performed in order to relate it to measurable quantities. In solids, the macroscopic dielectric function is related to the microscopic dielectric function ε by

$$\varepsilon_M(\omega) = \lim_{\mathbf{q}\to 0}\frac{1}{\varepsilon^{-1}_{\mathbf{G}=0,\mathbf{G}=0}(\mathbf{q},\omega)}. \tag{5.6.3}$$

The optical absorption spectrum is given by the imaginary part $\varepsilon_2(\omega)$ of $\varepsilon_M(\omega)$. The dielectric constant ε_0 is the value of $\varepsilon_M(\omega)$ at $\omega=0$. If ε is diagonal in $\mathbf{G},\mathbf{G}'$, ε_M is the spatial average of the microscopic dielectric function ($\varepsilon_M = \lim_{\mathbf{q}\to 0}\varepsilon_{\mathbf{G}=0,\mathbf{G}'=0}$). This is in fact the case in the homogeneous electron gas. The time ordered independent particle polarizability is given by

$$\chi_{\mathbf{q}}^0(\mathbf{G},\mathbf{G}',\omega) = \frac{1}{\Omega}\sum_{nn'\mathbf{k}} 2w_{\mathbf{k}}(f_{n'\mathbf{k}-\mathbf{q}} - f_{n\mathbf{k}}) \times \frac{\langle\psi_{n'\mathbf{k}-\mathbf{q}}|e^{-i(\mathbf{q}+\mathbf{G})\mathbf{r}}|\psi_{n\mathbf{k}}\rangle\langle\psi_{n\mathbf{k}}|e^{i(\mathbf{q}+\mathbf{G}')\mathbf{r}'}|\psi_{n'\mathbf{k}-\mathbf{q}}\rangle}{\omega+\epsilon_{n'\mathbf{k}-\mathbf{q}}-\epsilon_{n\mathbf{k}}+i\eta sgn[\epsilon_{n'\mathbf{k}-\mathbf{q}}-\epsilon_{n\mathbf{k}}]}. \tag{5.6.4}$$

Here Ω is the volume of the primitive cell, $w_{\mathbf{k}}$ is the k-point weight, $f_{n'\mathbf{k}-\mathbf{q}}$ and $f_{n\mathbf{k}}$ are the one electron occupancies of the corresponding states, $\epsilon_{n\mathbf{k}}$ and $\epsilon_{n'\mathbf{k}-\mathbf{q}}$ are energies of one electron states $|\psi_{n\mathbf{k}}\rangle$ and $|\psi_{n'fk-\mathbf{q}}\rangle$, and η is an infinitesimal complex shift.
In (5.6.4), the summation is carried out over all possible pairs of occupied and unoccupied states, such as the calculation of the polarizability becomes time consuming. The computational procedure can be optimized by the use of the spectral representation in which the polarizability matrix takes the form of

$$\begin{aligned}\chi^{S}_{\mathbf{q}}(\mathbf{G},\mathbf{G}^{'},\omega^{'}) = \frac{1}{\Omega}\sum_{nn'\mathbf{k}} 2w_{\mathbf{k}} sgn(\omega^{'})\delta(\omega^{'}+\epsilon_{n\mathbf{k}}-\epsilon_{n'\mathbf{k}-\mathbf{q}}) \\ \times (f_{n\mathbf{k}}-f_{n'\mathbf{k}-\mathbf{q}})\langle\psi_{n'\mathbf{k}-\mathbf{q}}|e^{-i(\mathbf{q}+\mathbf{G})\mathbf{r}}|\psi_{n\mathbf{k}}\rangle \\ \times \langle\psi_{n\mathbf{k}}|e^{i(\mathbf{q}+\mathbf{G}^{'})\mathbf{r}^{'}}|\psi_{n\mathbf{k}-\mathbf{q}}\rangle,\end{aligned} \tag{5.6.5}$$

[71]. We arrive at the relationship between the spectral function and the imaginary part of the polarizability

$$\chi^{S}_{\mathbf{q}}(\mathbf{G},\mathbf{G}^{'},\omega^{'}) = \frac{1}{\pi}\mathrm{Im}\chi^{0}_{\mathbf{q}}(\mathbf{G},\mathbf{G}^{'},\omega). \tag{5.6.6}$$

For a given frequency $\omega^{'}$, each pair of states $n\mathbf{k}$, $n^{'}\mathbf{k}-\mathbf{q}$ contributes to χ at the frequency $\omega^{'} = \epsilon_{n'\mathbf{k}-\mathbf{q}} - \epsilon_{n\mathbf{k}}$, this makes the evaluation of the spectral function efficient for $\omega^{'}$. On using the Hilbert or Kramers-Kronig transformation the polarizability are obtained from the spectral functions as

$$\begin{aligned}\chi^{0}_{\mathbf{q}}(\mathbf{G},\mathbf{G}^{'},\omega) = \int_{0}^{\infty} d\omega^{'}\chi^{S}_{\mathbf{q}}(\mathbf{G},\mathbf{G}^{'},\omega^{'}) \\ \times\left(\frac{1}{\omega-\omega^{'}-i\eta}-\frac{1}{\omega+\omega^{'}+i\eta}\right)\end{aligned} \tag{5.6.7}$$

In general ω and $\omega^{'}$ are defined on different frequency grids but in the above Equation they are chosen to the same set.

5.7 Two particles Green's function

The quasiparticle picture in the GW approximation is generally sufficient to obtain accurate photoemission spectra, but this approximation is still inadequate for photoabsorption processes in which electron-holes are created (without addition or removal of electrons). This deficiency can be overcome by first treating the quasielectron and quasihole within the GW approximation and then accounting for their interaction by solving the Bethe-Salpeter equation (BSE) for the two particle Green's function. In this section the Bethe-Salpeter equation will be deduced in order to describe the two particles excitations.

5.8 Second iteration of Hedin's equation

Let's consider $\sum = iGW$ as our starting point, the second iteration of the Hedin's equation can be achieved though the inclusion of vertex Γ in (5.4.5) for P, we obtain

$$\Gamma(12,3) = \delta(12)\delta(13) + iW(1^+,2)\int d(45)G(14)G(52)\Gamma(45,3). \tag{5.8.1}$$

Here, the approximation $\delta\sum/\delta G = iW$ is used [72]. Now let us introduce a four point polarization function $P(1,2;3,4)$ such that the polarization of (5.4.5) is obtained as $P(1,1;2,2)$ while a four point screened interaction is $W(1,2;3,4) = W(1,2)\delta(13)\delta(24)$. In following Equations (5.4.1) and (5.8.1) we obtain the four-point polarization

$$P(1,2;3,4) = P^0(1,2;3,4) - \int d(5678)P(1,2;5,6)W(5,6;7,8)P^0(7,8;3,4) \tag{5.8.2}$$

From the solution of (5.8.2) the microscopic dielectric function with (5.6.2) and subsequently the macroscopic dielectric function with (8.1). From [72] we define the new polarization function $\bar{P}$ as:

$$\bar{P} = P + P\bar{v}P \tag{5.8.3}$$

where $\bar{v}$ is the bare Coulomb potential without the long range term that in reciprocal space reads:

$$\bar{v}_{\mathbf{G}} = \begin{cases} 0, & \mathbf{G}(\mathbf{q}) = 0 \\ v_{\mathbf{G}}(\mathbf{q}) & \mathbf{G} \neq 0 \end{cases}$$

The macroscopic dielectric function can be written in terms of the new polarizability function as

$$\varepsilon_M(\omega) = 1 - \lim_{\mathbf{q}\to 0}[v_0(\mathbf{q})\bar{P}_{00}(\mathbf{q},\omega)]. \tag{5.8.4}$$

Substituting (5.8.2), in (5.8.3) we arrive at the so-called Bethe-Salpeter equation (BSE) that in matrix form reads:

$$\bar{P} = P^0 + P^0K\bar{P}. \tag{5.8.5}$$

The Kernel of the Bethe-Slapeter equation is given by

$$K(1,2;3,4) = -i\delta(1,2)\delta(3,4)\bar{v}(1,3) + i\delta(1,3)\delta(2,4)W(1,2). \tag{5.8.6}$$

In Equation (5.8.6), the Kernel corresponds to the time dependent screened Hartree-Fock approximation, this Kernel has two terms; the first term is the exchange term, and the second term corresponds to the variation of the self energy with respect the one particle Green's function [73].
In summary, the Bethe-Salpeter approach to the calculation of two particle excited states is a straightforward extension of the GW approach for the calculation of one particle excited states; and it leads to an effective two particle Hamiltonian [72].

5.9 Excitonic Hamiltonian

We define the excitonic Hamiltonian as:

$$\mathcal{H}^{exc}_{(n_1,n_2)(n_3,n_4)} = (\epsilon_{n_2} - \epsilon_{n_1})\delta_{n_1,n_3}\delta_{n_1,n_3} + i(f_{n_2} - f_{n_1})K_{(n_1,n_2)(n_3,n_4)} \tag{5.9.1}$$

where f_n represents the occupation number. From (5.8.5), it can be shown that the polarizabity $\bar{P}$ can be expressed as:

$$\bar{P}_{(n_1,n_2)(n_3,n_4)} = [\mathcal{H}^{exc} - I\omega]^{-1}_{(n_1,n_2)(n_3,n_4)}\,(f_{n_4} - f_{n_3}) \tag{5.9.2}$$

where I is the identity matrix $I = \delta_{n_1,n_3}\delta_{n_1,n_3}$. We define the spectra representation by

$$[\mathcal{H}^{exc} - I\omega] = \sum_{\lambda,\lambda'} \frac{|\lambda\rangle S^{-1}_{\lambda,\lambda'}\langle\lambda'|}{E_\lambda - \omega} \tag{5.9.3}$$

where $|\lambda\rangle$ and E_λ indicate the eigenvalues and eigenvector of $\mathcal{H}^{exc}$, so

$$\mathcal{H}^{exc}|\lambda\rangle = E_\lambda|\lambda\rangle \tag{5.9.4}$$

and $S_{\lambda,\lambda'}$ is the overlap matrix:

$$S_{\lambda,\lambda'} = \langle\lambda'|\lambda\rangle. \tag{5.9.5}$$

We note that (5.9.3) holds for a general non-Hermitian matrix.
Explicitly, we define an effective two particle Schrödinger equation:

$$\mathcal{H}^{exc}_{(n_1,n_2)(n_3,n_4)}A^{(n_3,n_4)}_\lambda = E_\lambda A^{(n_1,n_2)}_\lambda \tag{5.9.6}$$

that can be solved by diagonalization. Equation (5.9.6) couples the different two particle configurations and the coefficients $A^{(n_1,n_2)}_\lambda$ of the state $|\lambda\rangle$ permits to identify the character of each excitation.
The exciton amplitude is given by

$$\Psi_\lambda(\mathbf{r}_1,\mathbf{r}_2) = \sum_{n_1,n_2} A^{(n_1,n_2)}_\lambda \phi^*_{n_1}(\mathbf{r}_1)\phi_{n_2}(\mathbf{r}_2). \tag{5.9.7}$$

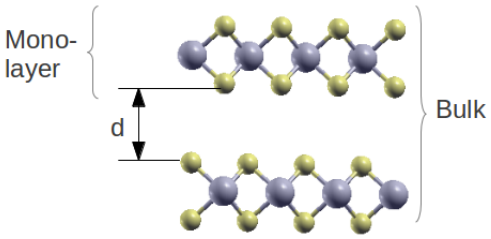
6. Structural properties

Molybdenum chalcogenides MoX_2 (X = S, Se, Te), with honeycomb structure offer many remarkable structural, mechanical, electronic and optical properties. The bulk crystals of the compounds crystallise in a 2H-MoX_2 (X = S, Se, Te) polytype in a hexagonal structure with space group $P6_3/mmc$ corresponding to space group number 194. The bulk 2H-MoX_2 (X = S, Se, Te) are composed of vertically stacked, weakly interacting layers held together by van der Waals interactions. Also each of these sheets are refereed to as a 1H-MoX_2 (X = S, Se, Te) monolayer. Many researchers have studied molybdenum disulfide. Thin films of MoS_2 particles have ultra low friction and wear, which stimulated some researchers, interest in the study of these materials. Jeffrey R. Lince investigated the electrical properties of the 2H-MoS_2 based coatings during tribological action [74]. Some properties of 2H-MoS_2 have been studied with theoretical methods. Jeffery A. Spirko investigated the defect structure of MoS_2 by density function methods [75]. S. Lebegue reported on ab initio calculations of the electronic structure of MoS_2 [76]. Also, Swashibrata Bhattacharya and Abhishek K. Singh studied semiconductor molybdenum dichalcogenide including 2H-MoX_2 (X = S, Se, Te) based on first principles calculations [77].
In this chapter, the structural properties and mechanical stability of layered molybdenum chalcogenides 2H-MoX_2 (X = S, Se, Te) compounds are studied using the self consistent Kohn-Sham method in DFT. Since the standard DFT is not able to describe correctly van der Waals interactions, we have added a semi-empirical dispersion potential to the Kohn-Sham DFT energy as suggested by Grimme (DFT-D2) [40, 41]. Also we have taken into account the non local correction functional for dispersion interaction proposed by Langreth and Lundqvist (vdW-DF) [42, 43] using the algoritm of Roman-Perez and Soler [78]. Layered molybdenum chalcogenides 2H-MoX_2 (X = S, Se, Te), have 2 Mo atoms and 4 X atoms in the unit cell. The full relaxation calculations were first performed to determine the accurate internal positions of the atoms. All atomic positions and lattice constants were optimized by using the conjugate gradient method. Numerical calculation was implemented in Viena Ab initio Simulation Package (VASP).

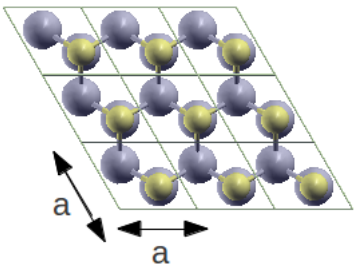
6.1 Cohesive energy

The cohesive energy is the work which is needed when a solid is decomposed into a free isolated atoms. The more negative the cohesive energy, the more stable the system, the expression of the cohesive energy is given in (4.3.1).
In order to find the structural parameters, such as the equilibrium lattice parameter a, c/a-ratio, the bulk modulus B_0 and its pressure derivative $B_0^{'}$, we have computed the cohesive energies in Equation (4.3.1) for each compound for different volumes. The cohesive energy as a function of volume are fitted with Birch Murnaghan's third order equation of state (EOS). The obtained cohesive energy versus volume data for different compounds 2H-MoX_2 (X = S, Se, Te) are visualized graphically in Figure (6.2), Figure (6.3), and Figure (6.4) respectively. The corresponding obtained structural parameters are

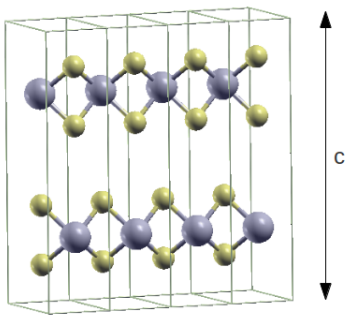
listed in Table (6.1) for these three compounds calculated with PBE, DFT-D2 and vdW-DF along with other results available. To estimate the stability of these compounds, it can be seen from Table (6.1), the calculated cohesive energies are negative, which indicate that these three compounds are structurally stable in these three different approximations.



(a)



(b)



(c)

Figure 6.1: (a) Molybdenum chalcogenides: Bulk 2H-MoX_2 (X = S, Se, Te) and monolayer 1H-MoX_2 (X = S, Se, Te). The big and small balls represent Mo and X (S, Se, Te) atoms respectively. The interlayer distance is denoted by d. (b) and (c), top and side view of the 2H-MoX_2 (X = S, Se, Te) unit cell.

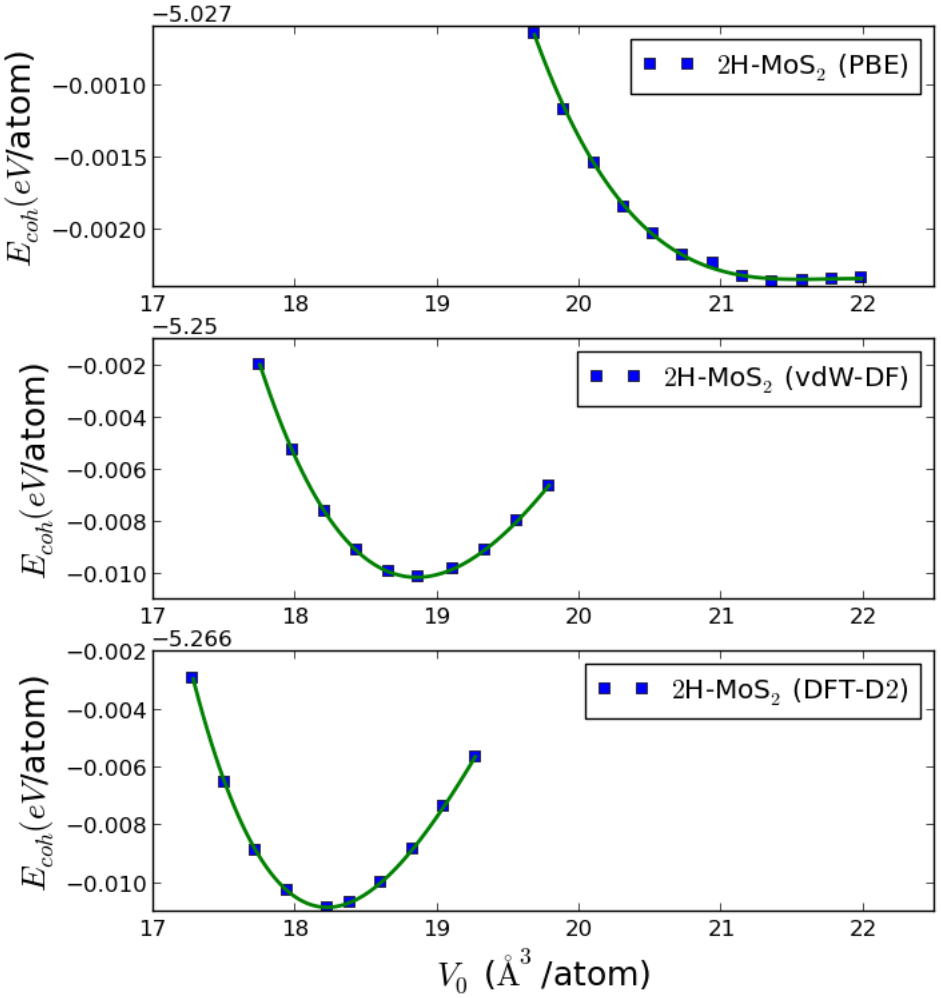


Figure 6.2: Cohesive energy E_{coh}(eV/atom) versus volume V(Å^3 /atom) for 2H-MoS$_2$ in three different approximations.

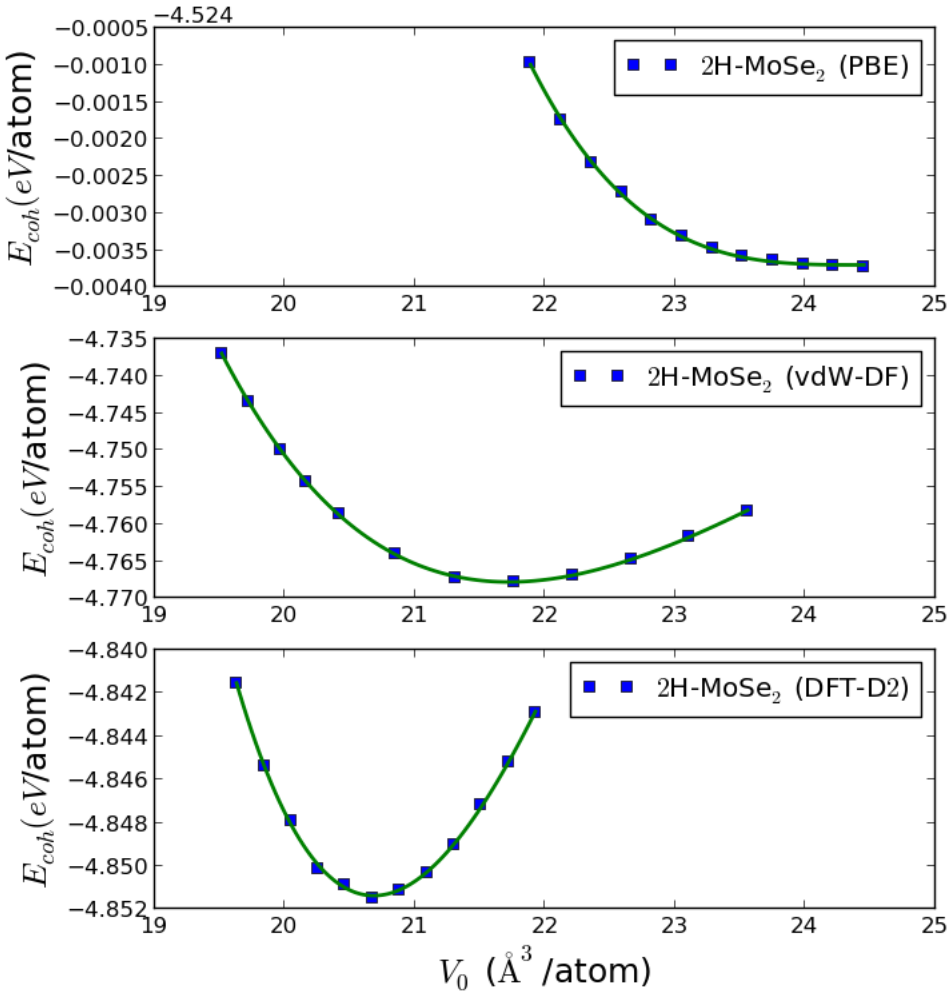


Figure 6.3: Cohesive energy E_{coh}(eV/atom) versus volume V(Å^3 /atom) for 2H-$MoSe_2$ in three different approximations.

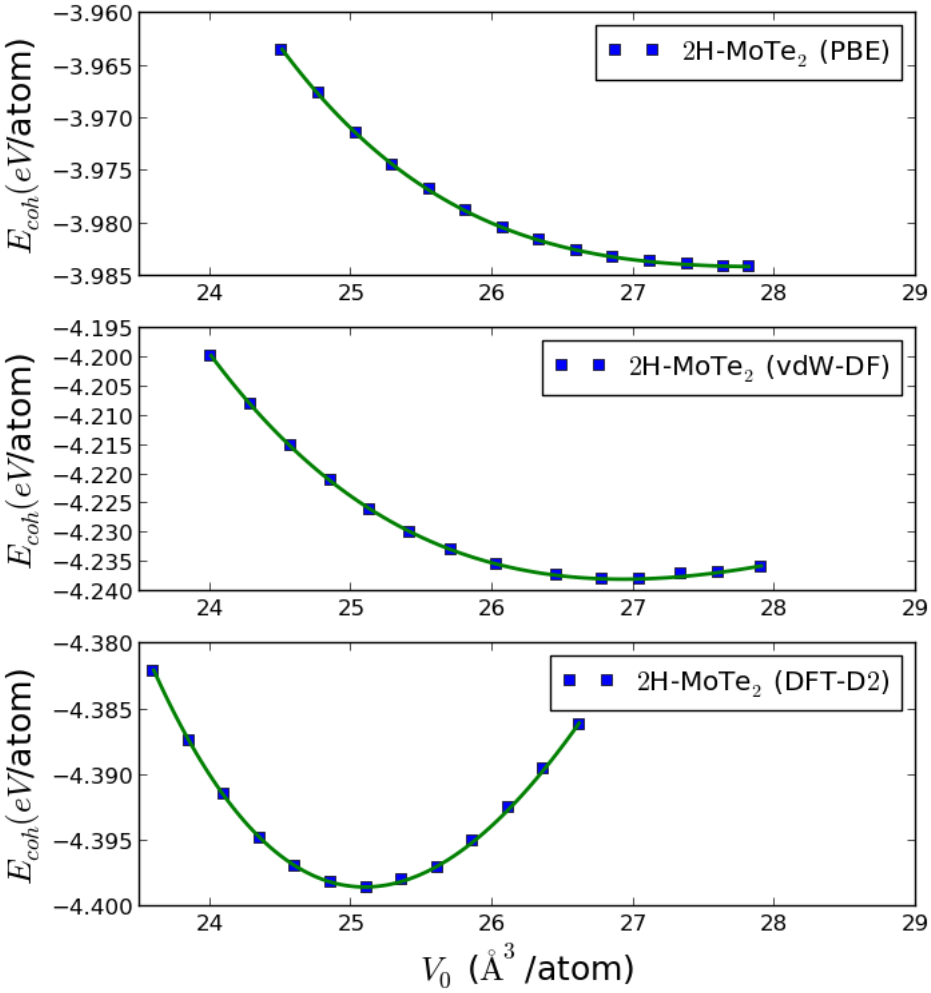


Figure 6.4: Cohesive energy E_{coh}(eV/atom) versus volume V(Å^3 /atom) for 2H-MoTe$_2$ in three different approximations.

Table 6.1: Equilibrium parameters: lattice parameter a, a/c-ratio, equilibrium volume, Bulk modulus B_0 and its pressure derivative $B_0^{'}$ at zero pressure are calculated in PBE, DFT-D2 and vdW-DF.

Material	a(Å)	c/a-ratio (Å)	V_0 (Å^3 /atom)	B_0 (GPa)	$B_0^{'}$	E_{coh}(eV/atom)
2H-MoS_2						
PBE	3.30	4.61	21.47	1.44	43.49	-5.02
vdW-DF	3.20	3.98	18.86	31.01	12.58	-5.26
DFT-D2	3.18	3.89	18.22	39.12	15.09	-5.27
Exp	3.16[a]	3.88[a]	17.76[a]	-	-	-
Other	3.13[b]	3.84[b]	-	-	-	-
2H-$MoSe_2$						
PBE	3.33	4.67	24.69	4.28	34.95	-4.52
vdW-DF	3.32	4.02	21.72	28.64	12.08	-4.76
DFT-D2	3.31	3.92	20.68	47.22	12.48	-4.85
Exp	3.28[a]	3.93[a]	20.13[a]	-	-	-
Other	3.30[b]	3.87[b]	-	-	-	-
2H-$MoTe_2$						
PBE	3.55	4.33	27.07	4.63	20.92	-3.98
vdW-DF	3.54	4.05	26.92	25.14	12.67	-4.23
DFT-D2	3.52	3.97	25.09	50.68	6.84	-4.39
Exp	3.51[a]	3.98[a]	24.96[a]	-	-	-
Other	3.50[b]	3.93[b]	-	-	-	-

[a]Reference [79]

[b]Reference [1]

Fitting data to the Birch Murnaghan's equation of state such as cohesive energy as a function of volume (at equilibrium) has become a common practice to deduce the structural parameters of materials. For all the 2H-MoX_2 (X = S, Se, Te) compounds, the PBE curves (cohesive energy versus volume) are flat at high volumes, this is because the PBE calculations do not take into account the weak van der Waals interaction (long range dispersion) between the layers of the compounds. Indeed to determine the equilibrium parameters of each compounds, we make an isotropic variation of the cell volume while ions with free internal parameters are allowed to search for minima on the Born Oppenheimer potential hyper-surface [80], until all Hellmann-Feynman force components [81] on each ion are smaller than 3×10^{-3} eV /Å. On increasing the volume, the layers move further apart and decouple, the ions in the layers become stable, thus, there is no change on the cohesive energy above a system dependent volume, consequently the curve becomes flat. Therefore it is difficult to see the equilibrium volume,

only a small local minimum volumes at 21.47 Å^3, 24.69 Å^3, and 27.07 Å^3 respectively, predicting a too large lattice constant a and c/a ratio when compared with our other calculations and the experimental values reported in reference [79]. As we can see, the PBE gives a $\sim 1\%$ - 4% error and consequently and error for $c/a \sim 8\%$ - 18% deviation when compared to experiment. On the contrary, dispersion effects included via atom pairewise interaction using the vdW-DF and DFT-D2 approximations, shift the minimum of the cohesive energy to lower volumes indicating an increased interaction between 2H-MoX_2 (X = S, Se, Te) layers, shrinking all the lattice parameters with respect to PBE. The vdW-DF curves start going up as a function of volume above a system dependent volume and the curvature becomes more clear in the DFT-D2 approximations so that we can easily see the equilibrium volume on the curve. There is a sensible improvement: the lattice constant a value, when compared to experiment, is corrected to within 0% - 1% and the c/a ratio to within 0% - 2%.

6.2 Formation energy

The relative stabilities of compounds can also be compared by means of their formation energies. In order to test the formation possibility under consideration as well as their stability, we have calculated the formation energy as expressed in Equation (4.4.2) for 2H-MoX_2 (X = S, Se, Te). We carried out the calculation using density function theory in PBE approximation, we have also taken into account the van der Waals interactions by using the vdW-DF and DFT-D2 approximations. All the calculations have been calculated at zero temperature (T $= 0$ K), and zero pressure (P $= 0$ GPa). Negative formation energy means an exothermic process and indicates that the compound is stable. The obtained formation energies E_f of these three compounds are given in Table (6.2) along with other available results, and shown graphically in Figure (6.5). It can be seen that our results are in good agreement with other results given in [79] and all the 2H-MoX_2 (X = S, Se, Te) compounds have negative formation energies, which means that the composing processes from the elemental forms are exothermic reactions and thus these 2H-MoX_2 (X = S, Se, Te) compounds are stable. Furthermore the formation energy is an important indicator of the strength of interlayer van der Waals interactions in bulk 2H-MoX_2 (X = S, Se, Te). The small formation energies indicate the ease to cleave a sheet of monolayer 1H-MoX2 (X = S, Se, Te) from bulk crystals [82]. Based on the obtained formation energies of the bulk 2H-MoX_2 (X = S, Se, Te) which are small, it can be deduced that, it is possible to fabricate monolayer 1H-MoX_2 (X = S, Se, Te) by reducing layers from bulk. Besides, it has been shown that monolayer 1H-MoX_2 (X = S, Se, Te) compounds are stable [82]. We extend our investigation in Chapter 7 to the electronic properties of monolayer 1H-MoX_2 (X = S, Se, Te). These monolayer materials have attracted significant potential applicatons [76, 83].

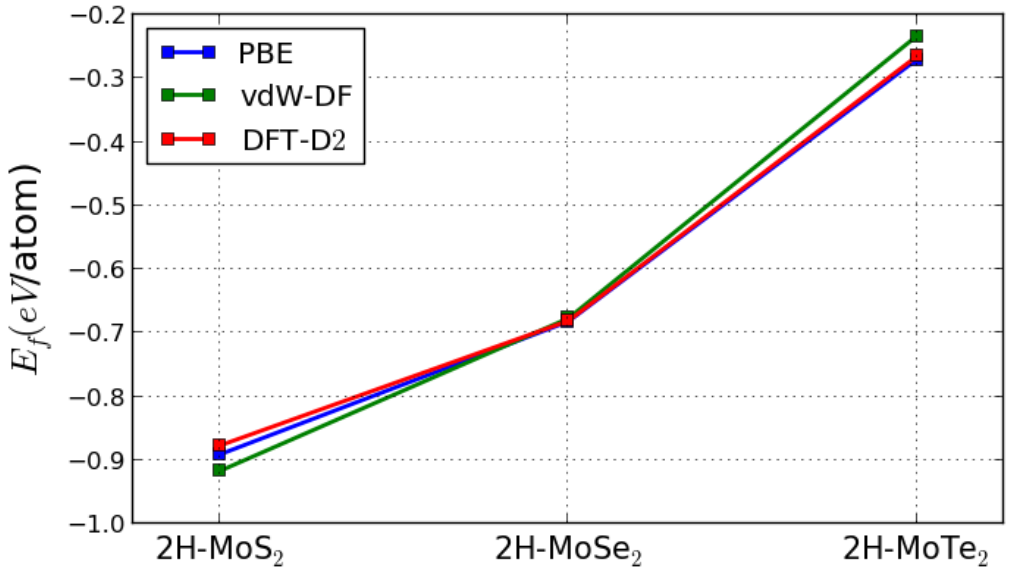


Figure 6.5: Formation energy E_f(eV/atom) versus 2H-MoX$_2$ (X = S, Se, Te) in PBE, vdW-DF and DFT-D2, the more negative the energy is, the more favourable the stability. It can be seen that E_f(2H-MoS$_2$) $< E_f$(2H-MoSe$_2$) $< E_f$(2H-MoTe$_2$), thus at zero temperature 2H-MoSe$_2$, and 2H-MoTe$_2$ have higher formation energies than 2H-MoS$_2$.

Table 6.2: Formation energy E_f (eV/atom) of 2H-MoX$_2$ (X = S, Se, Te) in three different approximations.

	2H-MoS$_2$			2H-MoSe$_2$			2H-MoTe$_2$		
	PBE	vdW-DF	DFT-D2	PBE	vdW-DF	DFT-D2	PBE	vdW-DF	DFT-D2
E_f	-0.891	-0.917	-0.877	-0.682	-0.677	-0.681	-0.270	-0.233	-0.265
Other	-0.863[a]	-	-	-0.670[a]	-	-	-0.270[a]	-	-

[a]Reference [79]

6.3 Mechanical stability

We present in this part the mechanical stability of 2H-MoX$_2$ (X = S, Se, Te) using elastic constants calculated from linear response. We have computed elastic constants using density functional theory in the GGA approximation parametrized by PBE, and with inclusion of van der Walls interaction proposed by vdW-DF, and DFT-D2. The linear elastic constants form a 6×6 symmetric matrix, having 27 different components and 21 of which are independents. However, the number of independent components may

be reduced for a given structure. For bulk 2H-MoX_2 (X = S, Se, Te), having hexagonal structure, the elastic independent elastic tensor reduces to 5 elastic constants: $C_{11} = C_{22}$, C_{12}, $C_{13} = C_{23}$, C_{33}, and $C_{44} = C_{55}$, in Voigt notation. All these values are calculated and listed in Table (6.3). The Born stability criteria for mechanical stability of hexagonal system are:

$$C_{11} > 0 \tag{6.3.1}$$

$$C_{44} > 0 \tag{6.3.2}$$

$$C_{11} - |C_{12}| > 0 \tag{6.3.3}$$

$$(C_{11} + C_{12})C_{33} - 2C_{13}^2 > 0 \tag{6.3.4}$$

All these four conditions for mechanical stability given in above Equations (6.3.1)-(6.3.4) are simultaneously satisfied and this clearly indicates that the predicted compounds are mechanically stable. These elastic constants are related to bulk modulus B and the four shear constants $(C_{11} + C_{12}, C_{11} - C_{12}, 1/2C_{33}$, and $C_{44})$. In order to determine all the constants we arrive at a set of equations where the first equation involves calculating the bulk modulus B, which is related to the elastic constants by:

$$B = \frac{2}{9}\left[C_{11} + C_{12} + 2C_{13} + \frac{1}{2}C_{33}\right]. \tag{6.3.5}$$

The anisotropic shear modulus

$$G = \frac{1}{2}(G_v + G_R) \tag{6.3.6}$$

where G_v is Voigt's shear modus corresponding to the upper bound of G values given by:

$$G_v = \frac{1}{30}(M + 12C_{44} + 12C_{66}) \tag{6.3.7}$$

where

$$M = C_{11} + C_{12} + 2C_{33} - 4C_{13}. \tag{6.3.8}$$

And G_R is Reuss's shear modulus corresponding to the lower bound of G values, which can be written as:

$$G_R = \frac{5}{2}\frac{C^2 C_{44} C_{66}}{3B_v C_{44} C_{66} + C^2(c_{44} + C_{66})}. \tag{6.3.9}$$

Then

$$G = \frac{1}{2}(G_v + G_R) \tag{6.3.10}$$

where

$$B_v = \frac{1}{9}\left[2(C_{11} + C_{12}) + C_{13} + C_{33}\right] \tag{6.3.11}$$

$$C^2 = (C_{11} + C_{12})C_{33} - C_{13}^2 \tag{6.3.12}$$

$$C_{66} = \frac{1}{2}(C_{11} - C_{12}) \tag{6.3.13}$$

In the formulae, subscript v denotes the Voigt bound, R denotes the Reuss bound.
The Young's modulus Y, and the Poisson's ratio ν, are also calculated in terms of the computed data and take the form of

$$Y = \frac{9GB}{3B + G} \tag{6.3.14}$$

and

$$\nu = \frac{1}{2}\left[\frac{3B - 2G}{3B + G}\right]. \tag{6.3.15}$$

In summary, the elastic constants have been investigated using PBE, vdW-DF, and DFT-D2 approximations. It has been found that all elastic constants satisfied the mechanical stability of these compounds. The highest bulk moduli values in Table (6.1) and in Table (6.3), the shear moduli in Table (6.3) are small compared to the polycrystalline moduli of the diamond (with 459 GPa as bulk modulus and 478 GPa for shear modulus at room temperature [84, 85], indicating that these compounds are soft materials. Apart from the mechanical stability, we have investigated other quantities related to the mechanical properties such as the Young's modulus Y which is defined as the ratio between stress and strain and is used to provide a measure of the stiffness of solids. The larger the value of Y is, the stiffer the material. The calculated Young's modulus Y in Equation (6.3.14) and listed in Table (6.3) indicates that the typical compounds having Young's modulus below $280 - 380$ are less stiffer than diamond [86]. The Poisson's ratio is also calculated in Equation (6.3.15), which can quantify the stability of the solid against shear. This ratio can formally take values in the range -1 to 0.5, where $\nu = -1$ indicates that the material does not change its shape, and $\nu = 0.5$ means that the volume remains unchanged, this occurs when an incompressible material deformed elastically at small strains [87]. The 2H-MoX_2 (X = S, Se, Te) compounds, have a slightly different Poisson's ratio as demonstrated in Table (6.3), and overall the obtained values are below 0.33 , which means that these compounds are brittle [88]. The brittleness (ductility), of the materials can also be predicted by applying Pugh's criteria [89] according to which a high (low) G/B value is associated with brittleness (ductility), i.e., the material is brittle if G/B is great than 0.57 otherwise the materials is ductile. From the calculated results in Table (6.3), it can be deduced that 2H-MoX_2 (X = Se, Te) are brittle materials. Our results on elastic constants are in disagreement with theoretical calulations for 2H-MoS_2 [90] (see Table (6.3)). The discrepancy with our results and others in Table (6.3) is probably due to the method used. In reference [90], Li, Chen Jun-Fang et al used the Castep program, based on density function theory with the PBE approximation to evaluate exchange correlation energy and a plane wave cutoff energy of 340 was employed throughout. Also non-local ultra-soft pseudo-potentials were used to describe the valence electrons.
Their results are consistentent with the mechanical stability, although our results are numerically differents but the conclusions are the same.

Table 6.3: Elastic constants C_{ij} (GPa), Bulk modulus B (GPa), Poisson's ratio ν, Young's modulus Y (GPa), Shear modulus (GPa) are calculated at zero pressure

	2H-MoS_2				2H-$MoSe_2$			2H-$MoTe_2$		
	PBE	vdW-DF	DFT-D2	Other	PBE	vdW-DF	DFT-D2	PBE	vdW-DF	DFT-D2
C_{11}	181.70	204.97	211.20	211.22[c]	142.22	182.05	183.11	107.62	113.04	131.92
C_{12}	45.41	53.40	56.58	49.38[c]	33	47.27	48.50	725.82	30.41	34.37
C_{13}	2.46	7.67	8.46	3.078[c]	1.31	16	17.89	2.11	8.93	23.87
C_{33}	3.82	34.96	44.10	36.73[c]	3.46	63.54	70.52	7.13	33.72	89.29
C_{44}	2.45	11.72	13.27	30.04[c]	2.87	26.55	28.15	5.36	15.64	33.47
B	51	64.71	68.17	63.36[c]	39.91	65.16	67.26	31.38	36.62	57.48
G	19.90	32.94	35.39	55.11[c]	16.66	42.87	44.29	15.62	25.54	41.17
Y	52.93	84.49	90.50	199.52[c]	43.89	105.49	108.96	40.21	63.08	99.71
ν	0.27	0.28	0.32	-	0.31	0.23	0.23	0.28	0.23	0.21

[c]Reference [90]

7. Electronic properties

In this part we are going to investigate the electronic properties both for bulk molybdenum chalcogenides 2H-MoX_2 (X = S, Se, Te) and for monolayer 1H-MoX_2 (X = S, Se, Te). Bulk monolybdenum chalcogenides 2H-MoX_2 (X = S, Se, Te) as well as monolayer molybdenum chalcogenides 1H-MoX_2 (X = S, Se, Te) are a rich source two dimensional (2D) crystals.

There has been a resurgence of interest in properties of these materials, specifically in their 2D crystalline form, for nanoscale electronics and photonics applications. These materials have band gaps falling in the visible or near-infrared regime so that they are promising for efficient solar-energy conversion. In their bulk states, 2H-MoX_2 (X = S, Se, Te) molybdenum chalcogenides are indirect gap semiconductors. It is well documented in the case of 2H-MoS_2, through both theory and experiment, that the material remains an indirect-gap semiconductor with a band gap of 1.29 eV until samples are thinned down to a monolayer, at which point the band gap becomes direct with a band gap energy of 1.90 eV [91].

Besides, electronic band structure is one of the most important parameters for a semiconductor to be used in solar-energy conversion [9].

Because of their relatively simple structure and the ease to form well-defined surfaces, electronic properties of the molybdenum chalcogenides have been intensively studied by direct and inverse photoemission. Reducing the slab thickness systematically from bulk to a monolayer causes a shift in the band gap energies, resulting in tunability of the electronic band gap. This tunability in the electronic band gap and transitions from indirect to direct band make these materials potential candidates for solar cell absorbers. In this chapter, we present the electronic properties of molybdenum chalcogenides compounds in two sections as follows.

In the first section we present a characterization of the electronic band structure for the bulk 2H-MoX_2 (X = S, Se, Te) via DFT calculations in three different approximations, PBE, DFT-D2 and vdW-DF in order to confirm the existence of the energy band gap of these compounds.

In the second section we present the energy band gap for the bulk and monolayer for molybdenum chalcogenides compounds within the GW approximation in order to predict quasiparticle band gap which is directly accessible through experimental techniques such as photoemission spectroscopy.

7.1 Band Structure and Projected Density of States in DFT

The electronic band structure has been calculated along the high symmetry points $\Gamma - M - K - \Gamma - A - L - H - A - L - M - K - H$ in the Brillouin zone, see Figure (7.2). The band structure of bulk molybdenum chalcogenides 2H-MoX_2 (X = S, Se, Te) compounds as well as the projected density of state (PDOS) in three different approximations are represented graphically in Figures (7.3)-(7.11)

We notice that for all of them, the conduction band has several different local minima, and the valence band has also several local maxima at high symmetry points. The energy gap i.e., the minimum separation between conduction and valence bands, is given by the difference in energy between the minimum of the conduction band and the maximum of the valence band. Because the extrema of conduction and valence bands lie at different **k**-points, this kind of band gap is called an indirect band gap, i.e., a change in the momentum is required for an electron to make a transition from the top of the valence band to the bottom of the conduction band. Therefore bulk 2H-MoX_2 (X = S, Se, Te) is indirect band gap semiconductor. These compounds have similar features in the band structure as well as the projected density of state.

The obtained band gaps of 2H-MoX_2 (X = S, Se, Te) in three different approximations are listed in Table (7.1) along with other theoretical and experimental values. Our calculated band gaps are in good agreement with the calculated gaps of 0.75 eV and 0.88 eV in [1, 9] but smaller than the experimental gaps reported in [92, 10, 76]. The difference in the band gap energies with other reported results is that, most of the results reported have been calculated with different approximations. Indeed the band gaps of 0.75 eV, 0.80 eV, and 0.66 eV reported in reference [1] for these three compounds respectively have been obtained using DFT with Troullier Martin, norm-conserving, relativistic pseudopotentials in fully-separable Kleinman and Bylander form [93, 94]. The exchange and correlation energies were treated within the local density approximation (LDA) according to the Ceperlay Alder (CA) parametrisation, where the geometry optimisation, numerical atomic orbitals with double zeta polarization (DZP) basis sets with a confinement energy of 30 meV were used. Also the convergence condition for energy was chosen as 10^{-5} eV between two consecutive self-consistent field (SCF) steps and $15\times15\times15$ Monkhorst-Pack of **k**-points was used while in our calculations a $9 \times 9 \times 2$ Monkhorst-Pack of **k**-points was used. The band gaps of 0.88 eV and 0.80 eV reported in reference [9] for 2H-MoX_2 (X = S, Se) have been obtained by employing the WIEN2k package [95] in which Kohn-Sham DFT equations are solved in the full-potential linearized augmented plane-wave (FP-LAPW) approach [96]. In these calculations, the following parameters have been used for the FP-LAPW basis: the muffin-tin (MT) radii R_{MT} are 2.15 Bohr for Mo, and 2.0 Bohr for S and Se; the LAPW basis functions with the angular quantum number of l up to $l_{max} = 0$ in the MT region. The Brillioun zone was sampled by a k-mesh of $12 \times 12 \times 2$.

Our results underestimate the experimental gaps by about 29%-40%. In fact, the underestimation of the band gap is the well known drawback of DFT calculations [61, 62, 63].
We note that the error of DFT for these materials is significantly smaller than those in the ZrS_2 family [18], where a typical error of about 70% has been observed. This can be attributed to the intra-atomic

nature of the band gap in these materials [9].

The band structure and the projected density of states (PDOS) for 2H-MoX$_2$ (X = S, Se, Te) can be divided into two regions of bands and states. The projected density of states (PDOS) curves around -4 eV to -7 eV are mainly derived from molybdenum Mo (p orbitals) which contribute to the bonding of Mo-X (X = S, Se, Te). The region originating from about -4 eV to the Fermi level is derived from the contribution of the p orbitals of the chalcogen X and small contribution of p and d orbitals of the molybdenum Mo. The region from the Fermi level to 4 eV is derived from d and p orbitals of Mo, also from 4 eV to 7 eV is mainly dominated by p orbital of Mo. Overall, the region up to the band gap in the valence bands and the region above the band gap are mainly contributed to by p orbitals of the chalcogen X and p, and d orbitals of molybdenum Mo.

However, the band gap energies for 2H-MoX$_2$ (X = S, Se, Te) decrease as we go from sulphides to the tellurium of molybdenum Mo. This is because as we go from S to Te, the electronegativity decreases and the orbital radii increase [1]. In fact the electronegativity (X in Pauling's units) is a measure of the ability of an atom to attract electrons to itself [97]. The electronegativity difference between two atoms forming a compound is proposed as a measure of the type of binding; the lager the electronegativity difference, the greater the ionic contribution to the binding. Various values for electronegativities have been investigated by W. Gordy and W. J. O. Thomas, included those of S, Se and Te, where $X_S > X_{Se} > X_{Te}$ [98]. It has been observed that electronegativity differences are greatest for compounds in which the component atoms come from widely separated columns in the Periodic Table [97]. Also for atoms in given column, electronegativity tends to decrease with increasing atomic number. This empirical observation was translated into a simple linear relationship between band gap and position of the components of a compound in the Periodic Table on the assumption that increased electronegativity difference means increased ionic contribution to the bonding, which in turn means increased band gap.
We also notice that the band gaps increase with the increased volumes as demonstrated in Figure (7.1). The calculated equilibrium volumes are 21 Å^3, 24 Å^3, and 27.07 Å^3 respectively. These values are larger when compared to experimental values which are localized at 17.76 Å^3, 20.13 Å^3, and 24.96 Å^3 in Figure (7.1).

In order to compare the band gaps calculated with their respective approximations, we have calculated the band gaps in the PBE using the DFT-D2 volumes. Indeed the PBE equilibrium volumes are too large (in comparison to experiment) but the DFT-D2 volumes are closest to experiment. Once again the band gaps in PBE approximation still larger than those of DFT-D2 but smaller than those of vdW-DF and the experimatal ones. For PBE, the DFT-D2 volumes were used (volumes closest to the experiment volumes) and the vdW-DF calculations have been performed with the equilibrium volumes listed in Table (6.1) which are also closest to the experiment volumes but a bit larger than the DFT-D2.

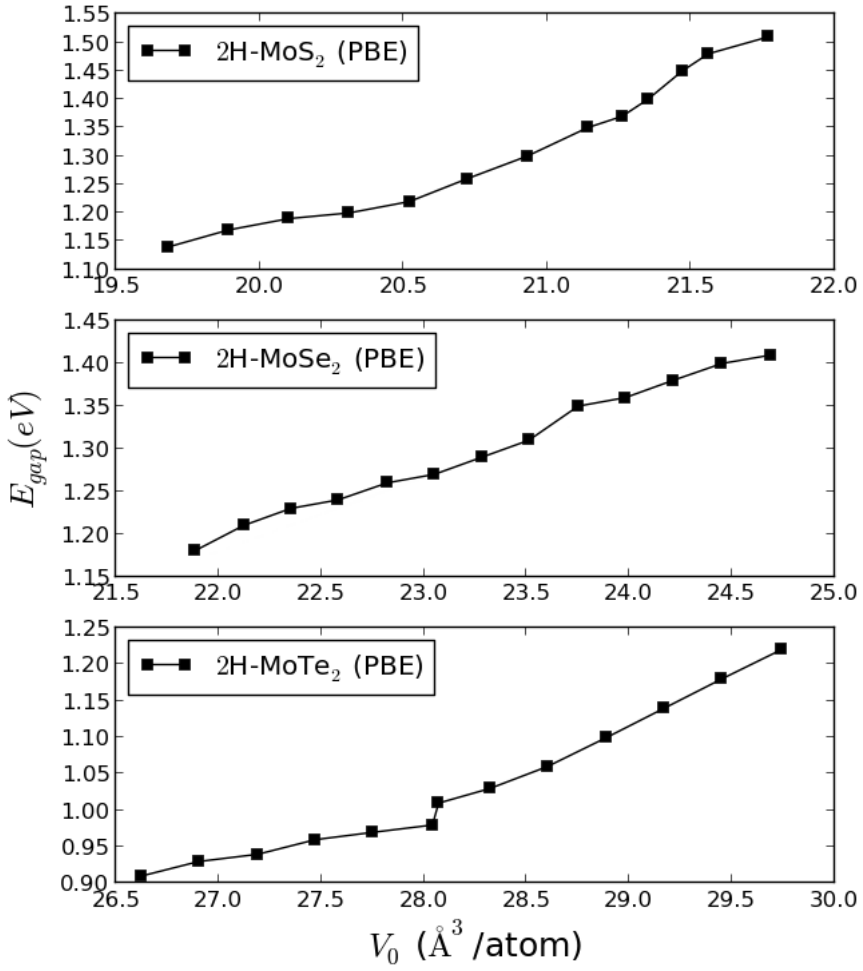


Figure 7.1: Band gap energies E_{gap} (eV) versus volume V(Å^3 /atom) for 2H-MoSX$_2$ (X = S, Se, Te) in PBE approximation.

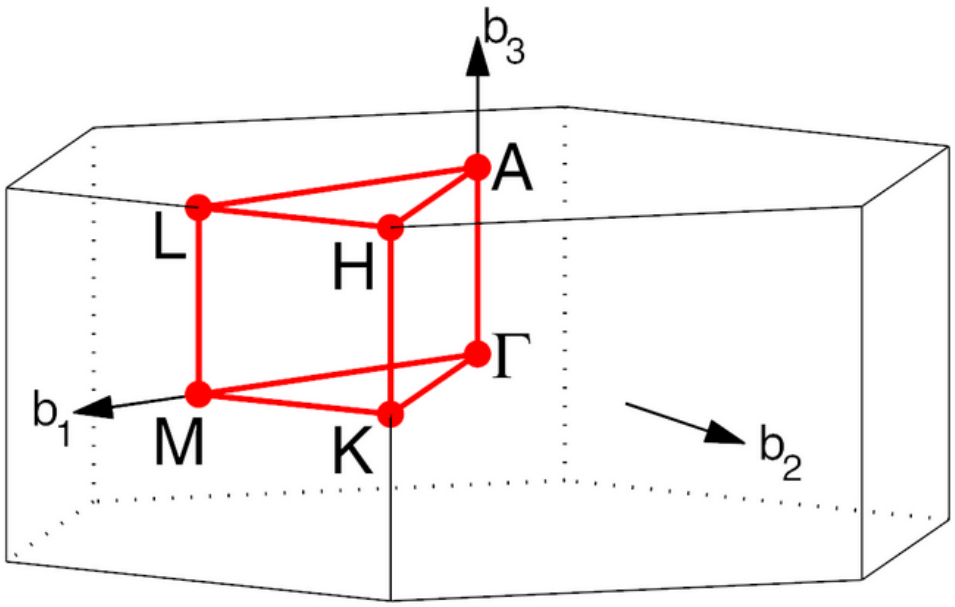


Figure 7.2: Brillouin zone with high symmetry points ($\Gamma - M - K - \Gamma - A - L - H - A$), b_1, b_2, and b_3 represent the lattices vectors.

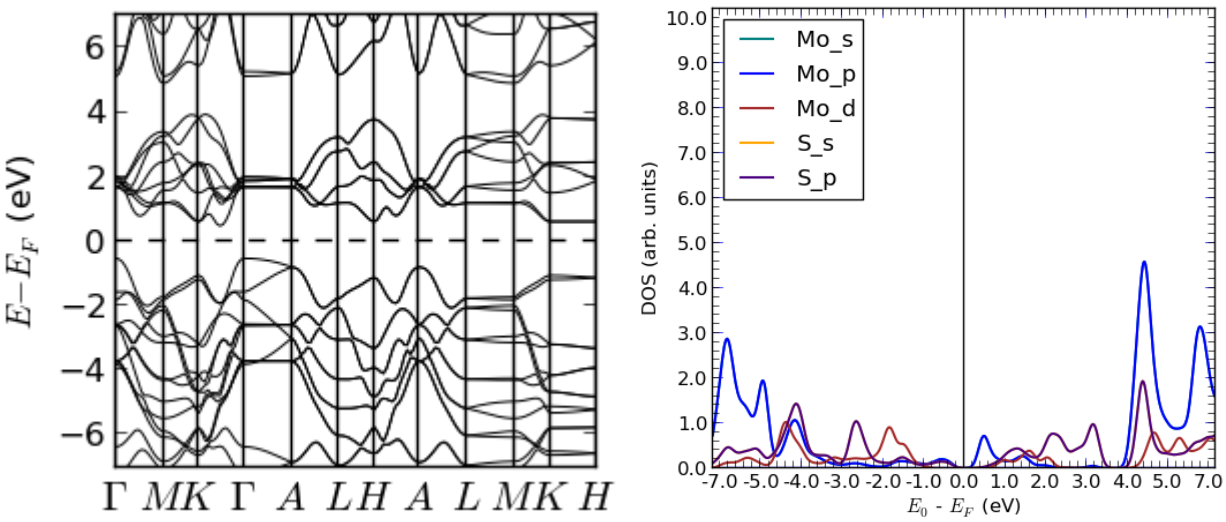


Figure 7.3: DFT in PBE approximation: Left, band structure for 2H-MoS_2 at zero pressure. The minimum of conduction band is at 0.48 eV, at the K high symmetry point and the maximum of the valence band is at -0.52 eV, at the Γ high symmetry point, thus an indirect band gap of 1.0 eV. Right, the projected density of state (PDOS).

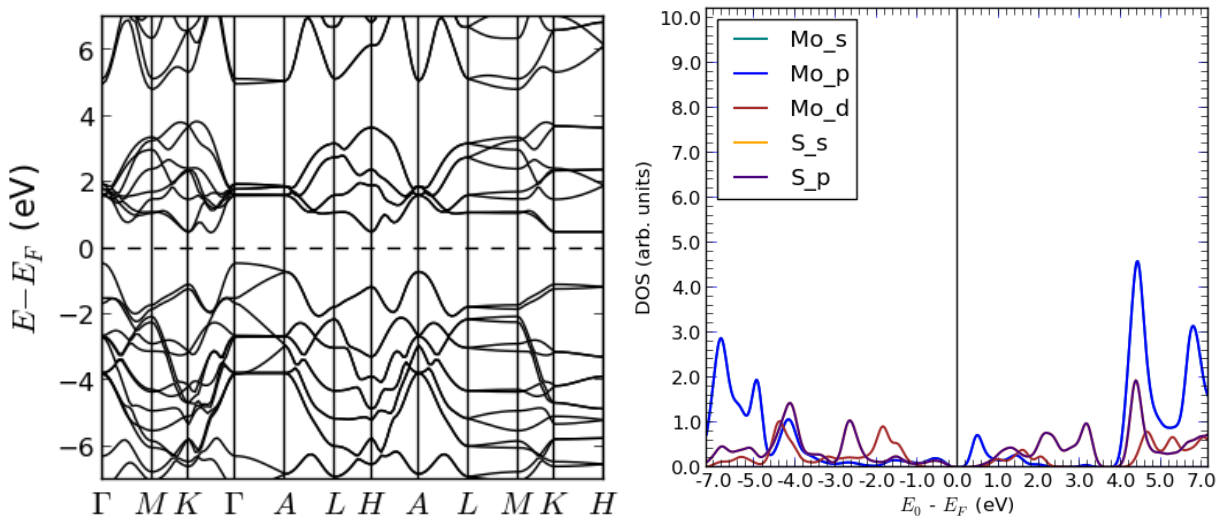


Figure 7.4: DFT in DFT-D2 approximation: Left, band structure for 2H-MoS_2 at zero pressure. The minimum of conduction band is at 0.48 eV, at the K high symmetry point and the maximum of the valence band is at -0.43 eV, at the Γ high symmetry point, thus an indirect band gap of 0.91 eV. Right, the projected density of state (PDOS).

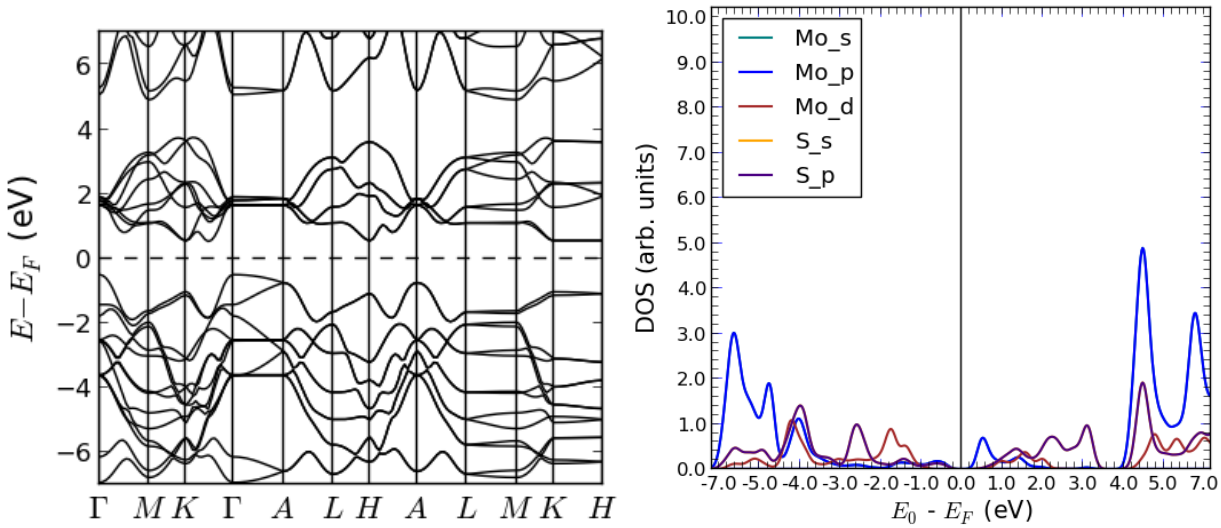


Figure 7.5: DFT in vdW-DF approximation: Left, band structure for 2H-MoS_2 at zero pressure. The minimum of conduction band is at 0.53 eV, at the K high symmetry and the maximum of the valence band is at -0.49 eV, at the Γ high symmetry, thus an indirect band gap of 1.02 eV. Right, the projected density of state (PDOS).

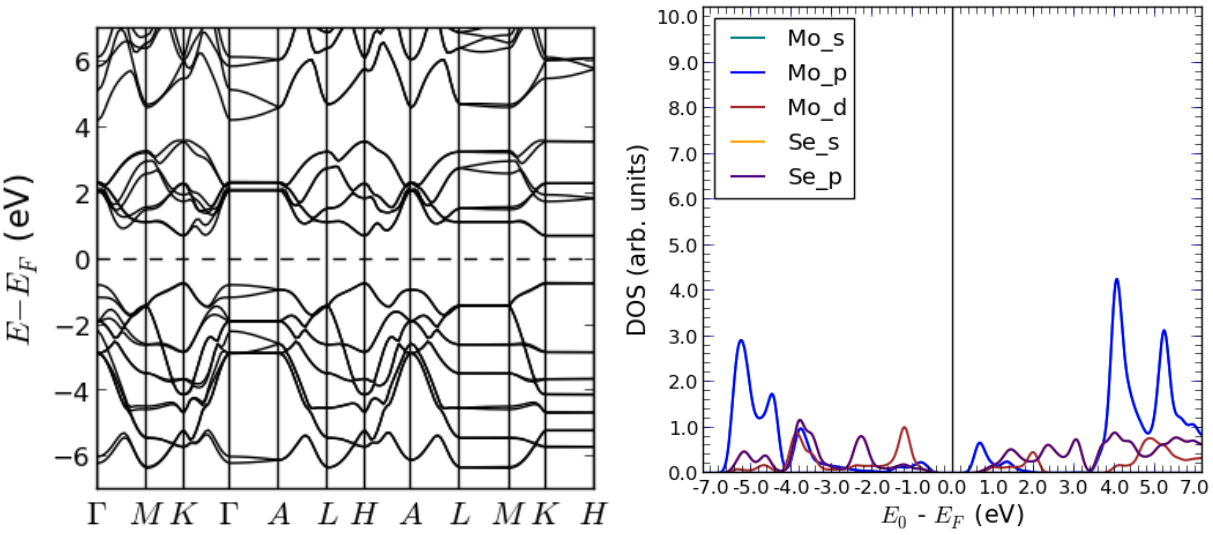


Figure 7.6: DFT in PBE approximation: Left, band structure for 2H-$MoSe_2$ at zero pressure. The minimum of conduction band is at 0.44 eV, at the K high symmetry point, and the maximum of the valence band is at -0.45 eV, at the Γ high symmetry point, thus an indirect band gap of 0.89 eV. Right, the projected density of state (PDOS).

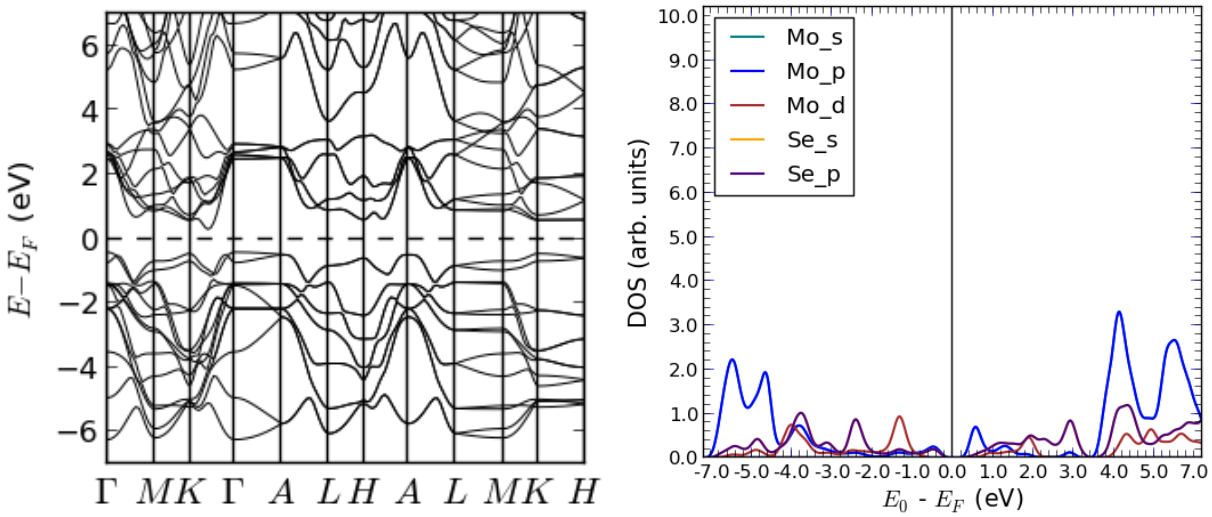


Figure 7.7: DFT in DFT-D2 approximation: Left, band structure for 2H-$MoSe_2$ at zero pressure. The minimum of conduction band is at 0.45 eV, at the K high symmetry point, and the maximum of the valence band is at -0.42 eV at the Γ high symmetry point, thus an indirect band gap of 0.87 eV. Right, the projected density of state (PDOS).

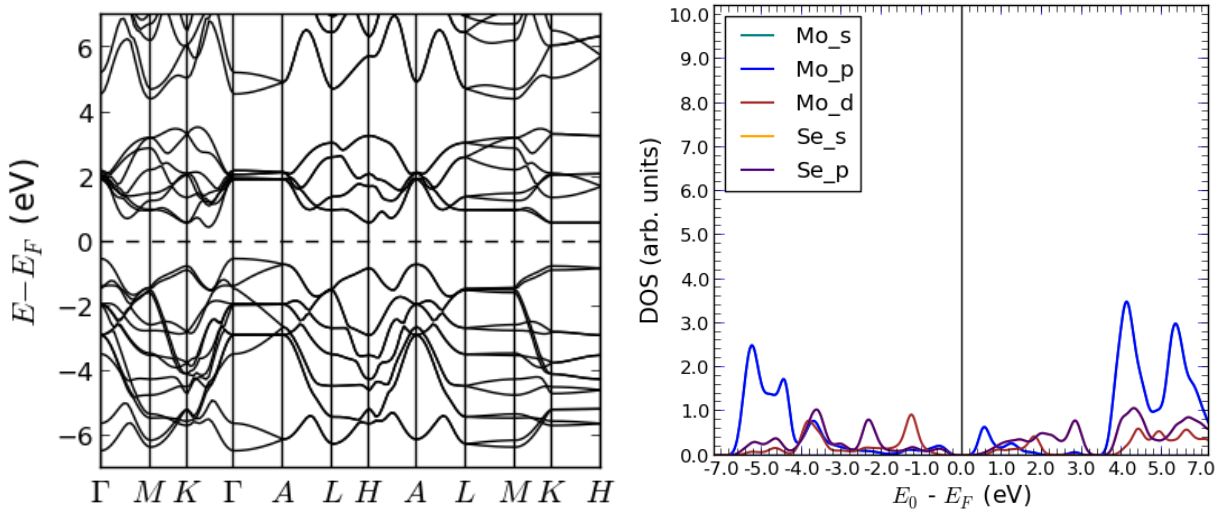


Figure 7.8: DFT in vdW-DF approximation: Left, band structure for 2H-$MoSe_2$ at zero pressure. The minimum of conduction band is at 0.45 eV, at the K high symmetry point and the maximum of the valence band is at -0.50 eV, at the Γ high symmetry point, thus an indirect band gap of 0.95 eV. Right, the projected density of state calculated (PDOS).

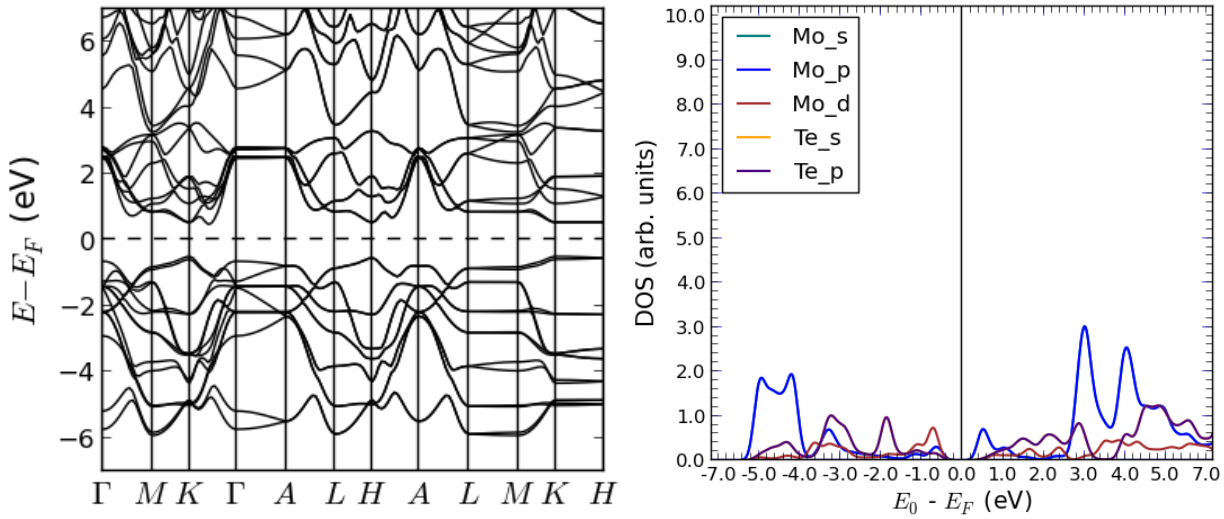


Figure 7.9: DFT in PBE approximation: Left, band structure for 2H-$MoTe_2$ at zero pressure. The minimum of conduction band is at 0.29 eV, at the K high symmetry point, and the maximum of the valence band is at -0.42 eV, at the Γ high symmetry point, thus an indirect band gap of 0.71 eV. Right, the projected density of state (PDOS).

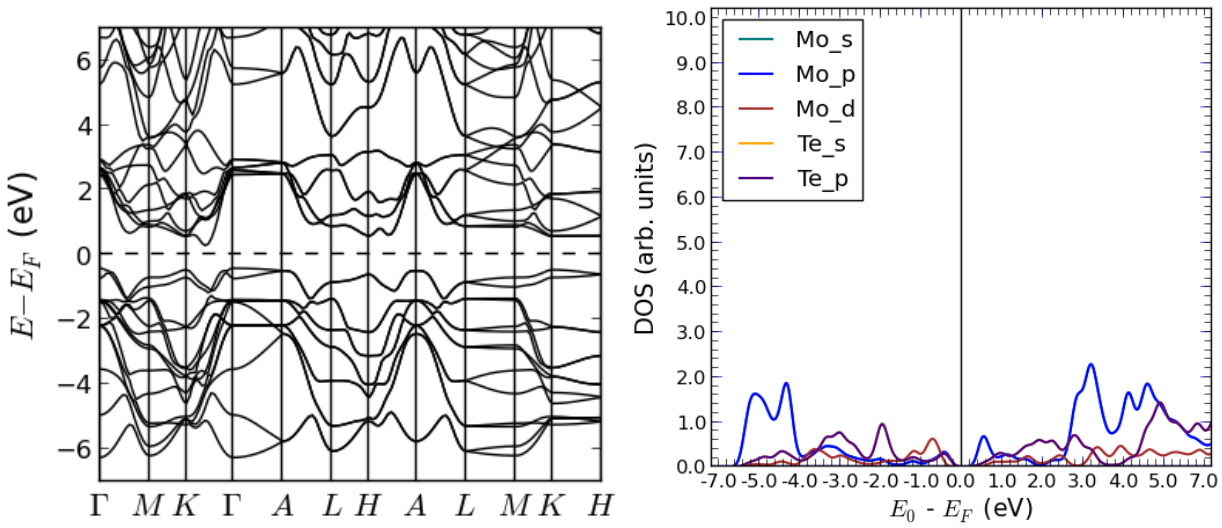


Figure 7.10: DFT in DFT-D2 approximation: Left, band structure for 2H-$MoTe_2$ at zero pressure. The minimum of conduction band is at 0.29 eV, at the K high symmetry point, and the maximum of the valence band is at -0.41 eV, at the Γ high symmetry point, thus an indirect band gap of 0.70 eV. Right, the projected density of state (PDOS).

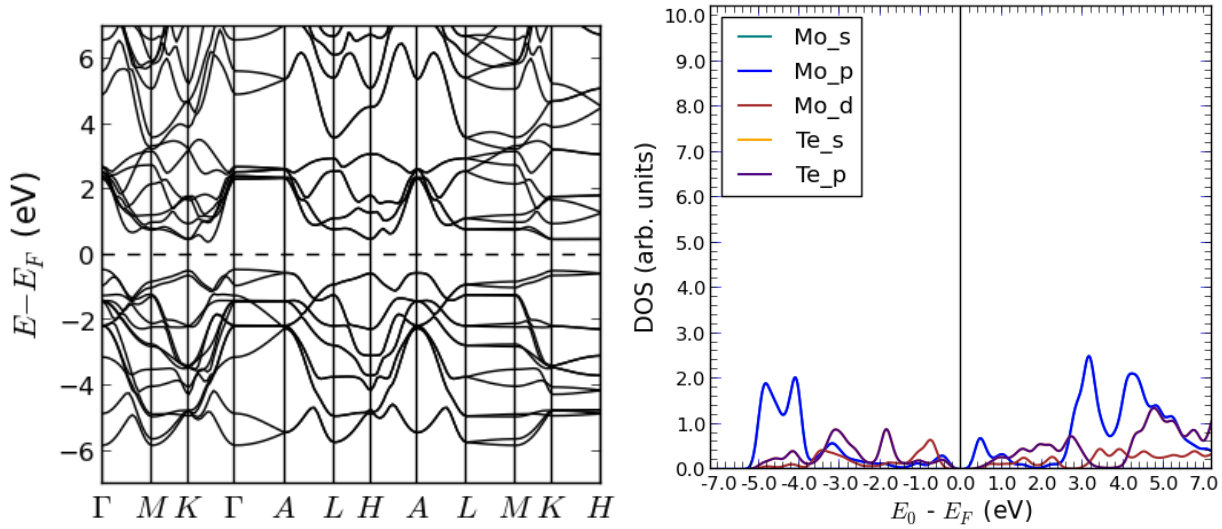


Figure 7.11: DFT in vdW-DF approximation: Left, band structure for 2H-$MoTe_2$ at zero pressure. The minimum of conduction band is at 0.40 eV, at K high symmetry point, and the maximum of the valence band is at -0.43 eV at Γ high symmetry point, thus an indirect band gap of 0.83 eV. Right, the projected density of state (PDOS).

Table 7.1: Energy band gaps E_{gap} for 2H-MoX_2 (X = S, Se, Te) compounds calculated in DFT within three different approximations.

	This work				
	PBE	DFT-D2	vdW-DF	Other	Exp
2H-MoS_2					
E_{gap}	1.0	0.91	1.02	0.75[d]	1.23[g]
				0.88[e]	1.29[h]
2H-$MoSe_2$					
E_{gap}	0.89	0.87	0.95	0.80[d]	1.09[h]
				0.84[e]	1.10[g]
2H-$MoTe_2$					
E_{gap}	0.71	0.70	0.83	0.70[f]	1.0[g]

[d] Reference [1]
[e] Reference [9]
[f] Reference [99]
[g] Reference [92]
[h] Reference [10]

7.2 Energy band gap in the GW approximation

We have seen the band structure and density of states of 2H-MoX_2 (X = S, Se, Te) in DFT approach. Our results are represented in Table (7.1) and underestimated the experimental values, and as mentioned before in section 7.1, the underestimation of the band gap is the well known drawback of DFT calculations. In order to correct the band gap energy, we have to go beyond DFT calculations by the use of a more accurate method. The main goal of this part is to attempt to solve the energy band gap problem of bulk 2H-MoX_2 (X = S, Se, Te) by a more accurate method. The GW approximation has proven to be a powerful tool to calculate the electronic structure of solid systems, by offering a strong formal basis for obtaining the band gap energy using the single-particle Greens function. Various reports of molybdenum chalcogenides for monolayers using GW approximation have been published [100, 9, 101]. We present in this part the electronic energy band gap of 2H-MoX_2 (X = S, Se, Te) calculated in GW approach on top of PBE, DFT-D2 and vdW-DF as well as the bandstructure for monolayer 1H-MoX_2 (X = S, Se, Te) calculated in GW approximation on top of PBE, DFT-D2 and vdW-DF DFT calculations.

7.3 Computational methods

Our calculations were performed with the Vienna Ab Initio Package (VASP). Core and valence electrons were treated using the Projector Augmented Wave (PAW) method. The so-called GW version of the PAW potentials supplied with VASP were employed here for all atoms; these potentials are designed to provide improved scattering properties at high energies. At the DFT level, electron exchange and correlation were treated using the PBE, DFT-D2, and vdW-DF. From convergence tests (bulk calculations), the kinetic energy cutoff was set at 520 eV, and the brillouin zone sampled with a $9 \times 9 \times 1$ Γ - centered **k**-point (see Appendix E). The Kohn-Sham DFT electronic structures obtained have served as a starting point for the excited state calculations. We have found that about 1008 bands for the response function are sufficient to converge the GW band gap to within 3×10^{-2} eV.

The calculations reported in this work were based on the partially self-consistent GW_0 using DFT in three different approximation (PBE, DFT-D2, and vdW-DF) eigenvalues as inputs. The quasiparticle energies were obtained by iterating G at least 4 times in the self-consistency cycle while deeping W fixed at its initial DFT W_0 as discussed in sections 5.2, 5.3, and 5.4.

In the case of a monolayer the structure is displayed in Appendix C. Each unit cell contains one Mo atom and two X atoms. A vacuum space of 19 Å between layers was enough to decouple a possible periodic interaction. The electron exchange and correlation were treated using the PBE, DFT-D2, and vdW-DF at the DFT level. From convergence tests, a kinetic energy cutoff of 400 eV was found to be enough to reach convergence and the Brillouin zone sampled with $12 \times 12 \times 1$ Γ - center **k**-points mesh was used in all the calcualtions (see Appendix E). 184 bands for the response function bands are sufficient to converge the GW gaps. The calculations reported in this work for monolayer structures were based on the single shot GW (G_0W_0) using DFT in three different approximation (PBE, DFT-D2, and vdW-DF) eigenvalues as inputs.

7.4 Quasiparticles in the GW approximation

Here we show the effect of the modified number of bands on the calculation of the quasiparticle band gap in the GW approximation for the bulk 2H-MoX_2 (X = S, Se, Te). The single shot GW (usually called G_0W_0) has a tendency of producing small gaps compared to experiments. [102]. It is believed that calculations beyond the usual single shot approximation will remedy this problem [103]. However, GW calculations with a full update of Greens function G and screened interaction W carried for the free-electron gas [104], and more recently for silicon (Si) semiconductor [105] show a significant overestimation of the bandwith and band gap. Such poor performance is usually explained by a shift of intensity from quasiparticle peaks into satellites, with a concomitant reduction of the screening. Technically, fully self-consistent GW calculations are exceedingly demanding. Beside, partially self-consistent GW (GW_0) calculations yield larger gaps than the single shot G_0W_0 method for a wide range of materials, at least within the applied approximations (model dielectric function and plasmon pole) [103].
We calculate the ground state electronic properties using the DFT in VASP. The calculations are performed in three different approximations (DFT-D2, PBE and vdW-DF). The DFT-D2 (PBE and vdW-DF) eigenvalues and eigenfunctions are then used to construct the Random Phase Approximation (RPA) screened coulomb interaction W in Equation (5.6.1) and the GW self Energy $\sum$ described in Equations (5.5.5) and (5.5.6). Thus the quasiparticle energies are obtained from Equations (5.3.12) and (5.3.13).

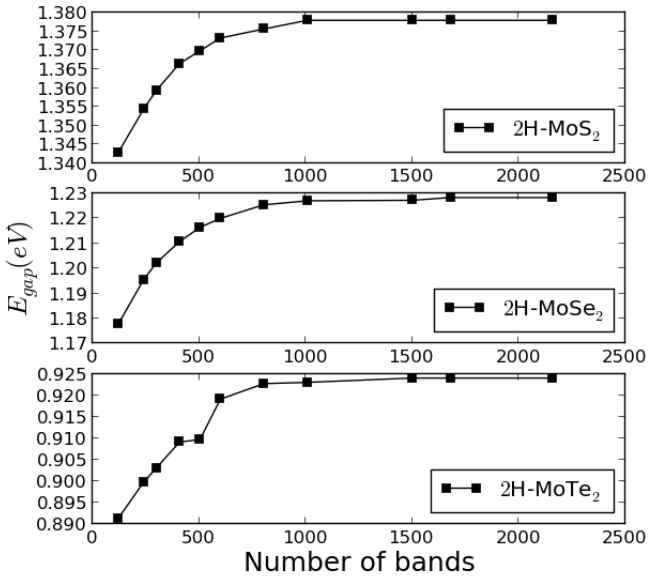


Figure 7.12: Band convergence of the quasiparticle band gap of 2H-MoX_2 (X = S, Se, Te) employing a $9 \times 9 \times 1$ **k**-point set in G_0W_0 with the DFT-D2 eigenvalues and wave functions as inputs approximation

The convergence of the quasiparticle gaps for these three compounds are calculated in the G_0W_0 approximation. This approximation is obtained from a single iteration of the Dyson in (5.4.3), starting from a Green function G_0. The self-energy is given as $\sum_{xc}[G_0] = -G_0W_0$ where W_0 is calculated by inserting G_0 into (5.4.5) and solving (5.4.2) with this irreducible polarization. The Dyson equation (5.4.3) is then solved with this self-energy to obtain an improved Green function G from which band gaps are calculated. We further consider a partially self-consistent scheme (GW_0) in calculating band gaps, in which we write the self-energy as $\sum_{xc}[G, G_0] = -GW_0$, where the Green function G is determined fully self-consistently by repeated solution of the Dyson equation and where W_0 is calculated from G_0 in the same way as for the G_0W_0 approximation.

The energy band gap as a function of number of bands is graphically represented in Figure (7.12). We have chosen 1008 as a converge number of bands in G_0W_0, and further updated in 4 iterations type of calculations corresponding to the partial GW (GW_0). The band gap energies are listed in Table (7.2) for these compounds in three different approximations. It can be observed from Table (7.2) that the band gap energies calculated using the GW approximation are larger than those calculated using DFT calculations. Our results overestimate the experimental gaps with about 6% - 18%. The GW approximation describe more reliably the excitation energies than DFT. The discrepancy between the calculated band gap in this work and the reported ones in references [9, 92, 10] is probably due to different approximation levels. In this work we used three different approximations for exchange-correlation energy and the lattice parameters are different from those used in [9, 92, 10]. For other results in Table (7.2), the experimental lattice constants have been used, where the atomic positions in the lattice were obtained by minimizing the total energy using the full-potential linearised muffin-tin orbital method (FP-LMTO) within the local density approximation (LDA) and performed with an $8 \times 8 \times 2$ k-points mesh [106]. We note that most of the experimental gaps listed in this work are obtained from optical absorption spectroscopic data.

Table 7.2: Energy band gaps E_{gap} for 2H-MoX_2 (X = S, Se, Te) compounds calculated in GW (GW_0) within three different approximations

	This work				
	PBE	DFT-D2	vdW-DF	Other	Exp
2H-MoS_2					
E_{gap}	1.37	1.37	1.46	1.23[e]	1.23[g] 1.29[h]
2H-$MoSe_2$					
E_{gap}	1.23	1.22	1.32	1.11[e]	1.09[e] 1.10[g]
2H-$MoTe_2$					
E_{gap}	0.93	0.93	1.06		1.0[g]

[e] Reference [9]
[g] Reference [92]
[h] Reference [10]

7.5 Band Structure of monolayer 1H-MoX_2 (X = S, Se, Te) in the GW approximation

The bulk 2H-MoX_2 (X = S, Se, Te) structure is composed of two dimensional sheets held together by weak van der Waals forces and strong intralayer bonds. Therefore the formation of ultra thin crystal of 2H-MoX_2 (X = S, Se, Te) known as monolayer 1H-MoX_2 (X = S, Se, Te) by micromechanical cleavage technique is possible. As demonstrated by Novoselov et al, individual sheets can be isolated by an exfoliation technique similar to those used to produce graphene [4]. Besides it has been shown that the band gap of the bulk 2H-MoX_2 (X = S, Se, Te) increases dramatically when the sample thickness is changed to a monolayer. Monolayer 1H-MoX_2 (X = S, Se, Te) is a highly interesting two dimensional system with a finite band gap and has recently been proposed for nanoelectronic and solar cell applications [7, 17]. Monolayer 1H-MoX_2 (X = S, Se, Te) unit cell contains 3 atoms (1 atom of Mo and 2 of X). The structure is uniquely determined by the lattice constant a (hexagonal lattice constant). For a structural relaxation of a monolayer a vacuum space of 19 Å between layers was enough to decouple a possible periodic interaction. The electron exchange and correlation were treated using the PBE, DFT-D2, and vdW-DF at the DFT level. From convergence tests, a kinetic energy cutoff of 400 eV was found to be enough to reach convergence and the Brillouin zone sampled with $12 \times 12 \times 1$ Γ - center **k**-points mesh was used in all the calcualtions (see Appendix E).
The equilibrium lattice constants were obtained by finding the minima of the total energy as a function of the lattice constant. The latter total energy is obtained by varying the lattice constant in the plane. Mo is fixed in three directions while X is allowed to move only in the z direction perpendicular to the plane of the Mo atoms. The lattice constants a are listed in Table (7.3). One can see that our results agree with other calculations [100].

We further present in this part convergence studies on quasiparticle energies as a function of number of bands in order to obtain reliable band gap energies for monolayer 1H-MoX_2 (X = S, Se, Te). The convergence has been studied in the same way (G_0W_0) as the convergence of the bulk and represented graphically in Figure (7.13). It can be seen that the quasiparticle bandgap decrease with increase of the number of bands which is contrary to the bulk results where the quasiparticle bandgaps increased with an increase of the number of bands. Convergence has been obtained with 180 valence bands, in contrast to the bulk case where about 1008 valence bands are necessary for convergence.
The quasiparticle energies were then employed to obtain the G_0W_0 band structure through Wannier interpolation using the WANNIER90 program [107]. The GW_0 approximation has not been applied in the case of monolayer systems because of the large computational effort involved when compared to the bulk systems.
Due to the similarity on the band structure in these three approximations we have plotted only the band structure calculated with DFT-D2 approximation for 1H-MoX_2 (X = S, Se, Te) but the band gap energies of these compounds are listed in Table (7.3) in three different approximations.

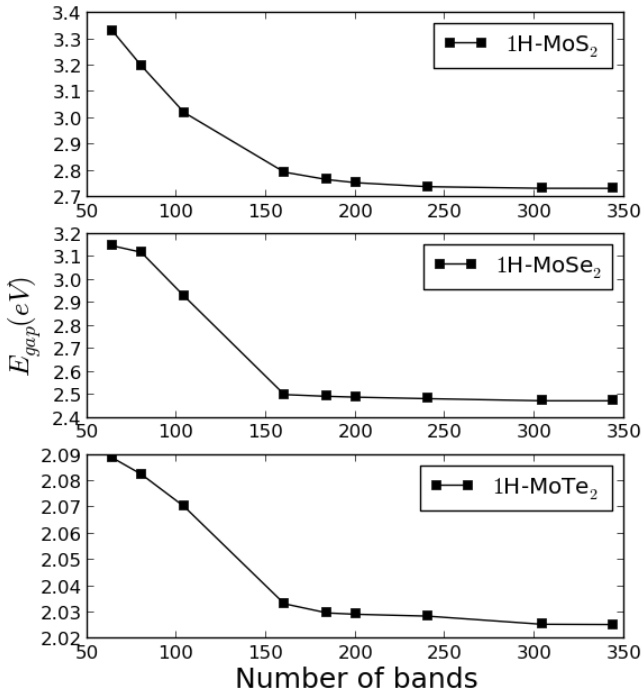


Figure 7.13: Band convergence of the quasiparticle band gap of 1H-MoX_2 (X = S, Se, Te) employing a $12\times12\times1$ **k**-point set in G_0W_0 with the DFT-D2 eigenvalues and wave functions as inputs approximation

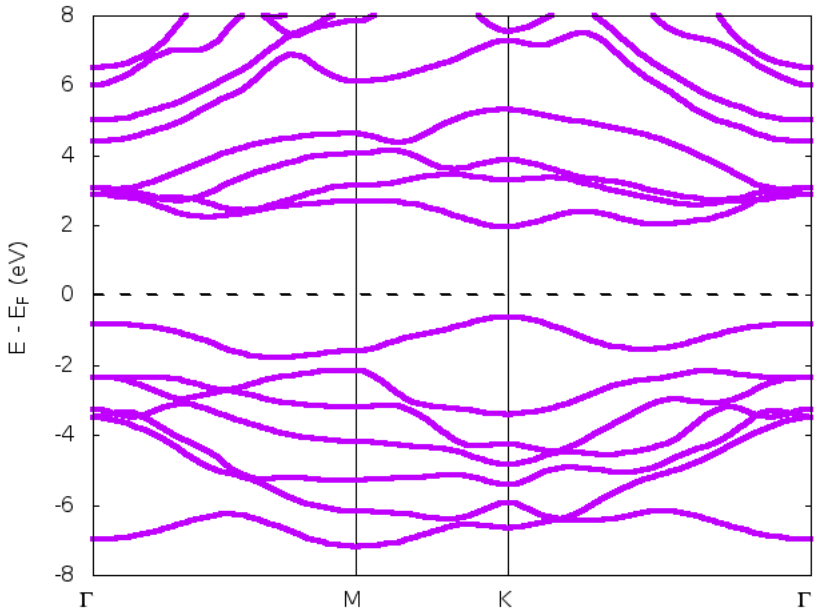


Figure 7.14: Quasiparticle band structure for 1H-MoS_2 at zero pressure. The minimum of conduction band is at 1.95 eV and the maximum of the valence band is at -0.85 eV, thus a direct band gap of 2.80 eV at K high symmetry point.

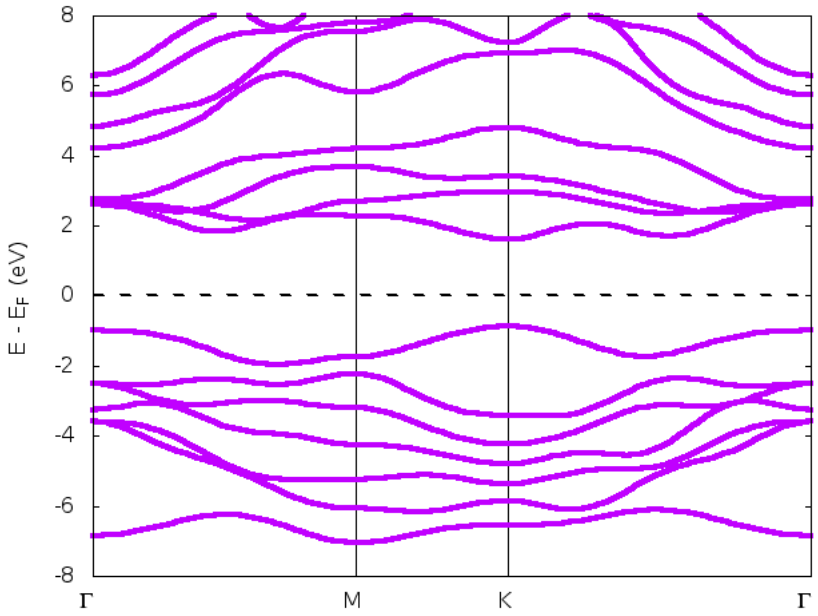


Figure 7.15: Quasiparticle band structure for 1H-$MoSe_2$ at zero pressure. The minimum of conduction band is at 1.61 eV and the maximum of the valence band is at -0.87 eV, thus a direct band gap of 2.48 eV at K high symmetry point.

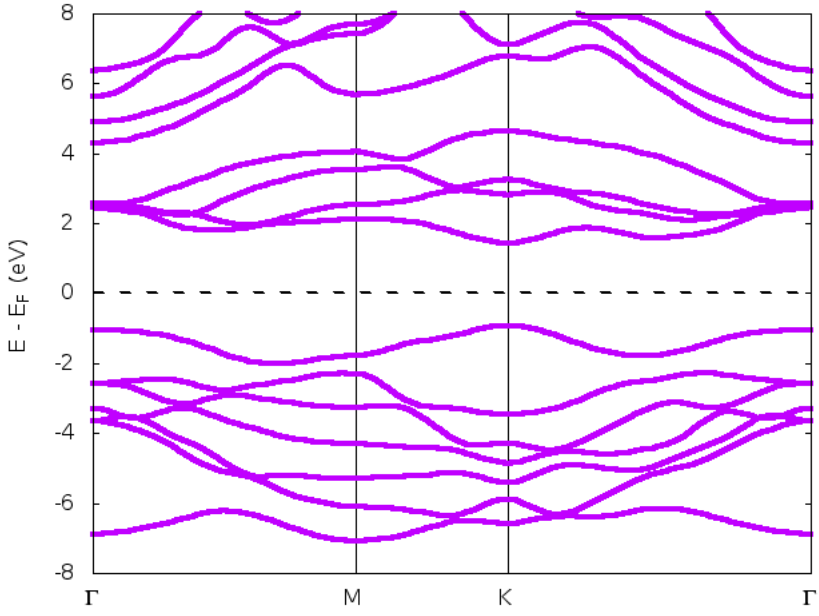


Figure 7.16: Quasiparticle bandand structure for 1H-$MoTe_2$ at zero pressure. The minimum of conduction band is at $0.1.43$ eV and the maximum of the valence band is at -0.92 eV, thus a direct band gap of 2.18 eV at K high symmetry point.

The electronic band structure for 1H-MoX_2 (X = S, Se, Te) has been calculated along the high symmetry points $\Gamma - M - K - \Gamma$ (see Figure (7.2)), and are represented graphically in above Figures (7.14) - (7.16). For all these compounds; we find a direct band gap. For instance, the band structure of 1H-MoS_2 is calculated at the lattice constant of 3.18 Å and by our G_0W_0 calculation is a K to K direct band gap semiconductor with a band gap of 2.80 eV using DFT-D2. The same value has been obtained with vdW-DF, but with the difference of 0.01 eV using PBE DFT input wavefunctions and energies calculation. Overall, the different approximations do not have a large effect on the result as far as the band gaps are calculated.
This prediction is in excellent agreement with the recent calculation for monolayer 1H-MoS_2 at the experimental lattice constant of 3.16 Å using full-potential linearized muffin-tin-orbital method (FP-LMTO), which predicted a K to K direct band gap of 2.76 eV. The band gap also agrees with the reported gaps in reference [106]. The difference in the band gaps with other results reported in Table (7.3) is probably due to the numeral methods used. In fact in reference [100], the calculations have been done at the same lattice constant of 3.18 Å (our calculation) but $6 \times 6 \times 1$ Γ - centered **k**-points mesh was used, and the subsequent non-self-consistent with spin-orbit coupling (SOC) calculation.

Also it has been shown that using G_0W_0, the band gap of 1H-MoS_2 is indirect with the value of 2.49 eV with a lattice parameter of 3.16 Å [108] while the direct band gap of 2.80 eV has been found with a lattice parameter of 3.19 Å [101].
In reference [9] , the band gaps have been obtained using the experimental lattice of 3.16 Å, the calculations were performed using FHI-gap (Green's function with Augmented plave waves) package to WIEIN2K with Brillouin zone k - mesh of $6 \times 6 \times 1$.

Besides, for monolayer 1H-MoX_2 (X = Se, Te) the discrepancy of band gaps , with other results is mostly due to the difference on the lattice constants and the numerical method used. Comparing GW (G_0W_0) and experimental values, we can see that, in general the GW direct gaps are consistently larger than the experimental ones, obtained from direct fitting of the absorption data, by about $0.45 - 1.1$ eV. The question of how well the one-shot G_0W_0 approximation describes the true electronic structure of these systems remains open. Partially self-consistent GW_0 and fully self-consistent GW calculations for 1H-MoS_2 have been shown to consistently yield direct band gaps of $2.75 - 2.80$ eV [101] which are in good agreement with our results (G_0W_0).

Table 7.3: Relaxed lattice parameter a (Å) and band gap energy E_{gap} (eV) for 1H-MoX_2 (X = S, Se, Te) compounds calculated in GW (G_0W_0) within three different approximations.

	This work				
	PBE	DFT-D2	vdW-DF	Other	Exp
1H-MoS_2					
a	3.20	3.18	3.18	3.18[i]	3.16[a]
E_{gap}	2.81	2.80	2.80	2.07[e]	1.90[k]
				2.77[i]	-
				2.82[j]	-
1H-$MoSe_2$					
a	3.32	3.31	3.31	3.32[j]	
E_{gap}	2.48	2.48	2.47	1.83[e]	1.38[l]
				2.41[j]	-
1H-$MoTe_2$					
a	3.18	3.18	3.22	3.55[j]	
E_{gap}	2.36	2.35	2.35	1.77[j]	-

[a] Reference [79]
[e] Reference [9]
[i] Reference [101]
[j] Reference [100]
[k] Reference [91]
[l] Reference [92]

8. Optical properties

Molybdenum chalcogenides in its monolayer structure 1H-MoX$_2$ (X = S, Se, Te) were successfully fabricated using a micromechanical cleavage method in 2005 [4]. Since then, these monolayer materials have attracted significant applications [76, 83]. For example, monolayer 1H-MoS$_2$ has been employed successfully in the fabrication of low-power field effect transistors [7], logic circuits [109], and phototransitors [110]. Besides, optical properties of 1H-MoS$_2$, which are directly accessible through experimental techniques such as photoabsorption, and photoluminescence spectroscopy, have been thoroughly studied experimentally [111, 112]. The absorption spectra shows two distinct low energy peaks at 1.88 eV and 2.06 eV for 1H-MoS$_2$ [113], at 1.57 eV and 1.82 eV for 1H-MoSe$_2$ and at 1.10 eV and 1.48 eV for 1H-MoTe$_2$ [113]. These peaks are denoted by A and B respectively and derived from direct transitions between a valence band and the conduction band at the K point of the Brillouin zone. Recall that we showed in a previous chapter that the monolayer 1H-MoX$_2$ (X = S, Se, Te) compounds all have a quasiparticle direct gap at the K point.

The goal of this chapter is to accurately predict the optical spectra of monolayer molybdenum chalcogenides 1H-MoX$_2$ (X = S, Se, Te). As discussed in section 4.6, it is well known that density functional theory (DFT) is ill equipped to describe photoemission as the Kohn-Sham energies do not correspond to quasiparticle energies, which are required to correctly describe electron addition or removal events. As mentioned before, a widely employed and efficient means to overcome this problem is the GW approximation, which goes beyond the mean-field, independent particle DFT approach and properly accounts for many-body electron-electron interactions. While quasiparticle calculations are generally sufficient to obtain accurate photoemission and inverse photoemission spectra, it is still inadequate to describe photoabsorption processes [72, 114, 115] in which electron-hole pairs are created (without actual addition or removal of an electron). This deficiency in DFT and GW approaches can be addressed by first calcualting the quasielectron and quasihole eigenvalues and eigenfunctions within the GW approximation and then accounting for their interaction by solving the Bethe-Salpeter equation (BSE) for the two particle Green's function. In the past couple of years a number of theoretical studies of the electronic band structure and optical excitations in monolayer 1H-MoS$_2$ have been published [100, 101]. These studies are based on many-body perturbation theory in the GW approximation (mainly the non-self consistent G$_0$W$_0$ approach) for the band structure and Bethe-Salpeter equation (BSE) with a statically screened electron-hole interaction for optical excitation [72, 114, 115].

While each additional level of theory in the GW-BSE ladder inevitably increases computational cost, this process cannot be dispensed with for the monolayer molybdenum chalcogenides of interest here, given the pre-existing evidence for strong exciton binding in 1H-MoS$_2$ [106]. Therefore, this sequence of calculations is systematically undertaken for each monolayer molybdenum chalcogenides in the following. Standard Kohn-Sham DFT calculations with DFT (PBE, DFT-D2, and vdW-DF) exchange correlation approximations were first performed for structural relaxation of the molybdenum chalcogenides monolayers. DFT calculations for the relaxed structures were then performed to get the DFT eigenvalues

and wave functions as input to the GW calculations. Full frequency dependent GW calculations were performed at the non-self-consistent G_0W_0 level, which involves only calculation of quasiparticle energies while preserving the DFT input wave functions. As a final step, BSE calculations were performed in the basis of the G_0W_0 quasielectron and quasihole wave functions to obtain optical absorption spectra for the monolayers samples.

Due to the similarity of the results of the different approximations, in this chapter we present the BSE spectra for DFT-D2 calculations only. BSE results for all three DFT exchange correlation approximations as starting point are listed in Table (8.1) .

An important aspect of optical properties can be discussed by means of the dielectric function, which depends on the momentum transfer **q** in the photon-electron interaction and the energy ω.
At lower energies (like that of solar radiation), one can assume $\mathbf{q} = 0$ and consider only the dielectric-dipole approximation. The total dielectric function is :

$$\varepsilon(\omega) = \varepsilon_1(\omega) + \varepsilon_2(\omega), \tag{8.0.1}$$

where ε_1 is the frequency dependent real part while ε_2 corresponds to the imaginary part.
Direct interband transitions, which are important for semiconducting materials, contribute to the imaginary part $\varepsilon_2(\omega)$. Considering the appropriate transition matrix elements, $\varepsilon_2(\omega)$ is calculated from transitions from the occupied to unoccupied states:

$$\varepsilon_2^{\alpha,\beta}(\omega) = \frac{4\pi^2 e^2}{\Omega} \lim_{q\to 0} \frac{1}{q^2} \sum_{c,\mu,\mathbf{k}} 2\mathbf{w_k} \delta(\varepsilon_{c\mathbf{k}} - \varepsilon_{\mu\mathbf{k}} - \omega) \times \langle u_{c\mathbf{k}+e_{\alpha\mathbf{q}}} | u_{\mu\mathbf{k}} \rangle \langle u_{c\mathbf{k}+e_{\beta\mathbf{q}}} | u_{\mu\mathbf{k}} \rangle, \tag{8.0.2}$$

where the band indices c and μ refer to conduction and valence band states respectively. The vectors u_α are the unit vectors for the three cartesien directions, Ω is the volume of the unit cell, and $u_{c\mathbf{k}}$ is the cell periodic part of the orbitals at the k-point **k**. The real part of the dielectric matrix $\varepsilon_1(\omega)$ is obtained by the Kramers-Kronig relation. Mathematically,

$$\varepsilon_1^{\alpha,\beta}(\omega) = 1 + \frac{2}{\pi} P \int_0^\infty \frac{\varepsilon_2^{\alpha,\beta}(\omega')\omega'}{\omega'^2 - \omega^2 + i\eta} d\omega', \tag{8.0.3}$$

where P denotes the principal value of the integral and η the complex shift.
The knowledge of both the real and imaginary parts of the dielectric matrix allows one to calculate other important optical spectra such as the absorption coefficient $\alpha(\omega)$:

$$\alpha(\omega) = \omega \sqrt{2\sqrt{\varepsilon_1^2(\omega) + \varepsilon_2^2(\omega)} - \varepsilon(\omega)} \tag{8.0.4}$$

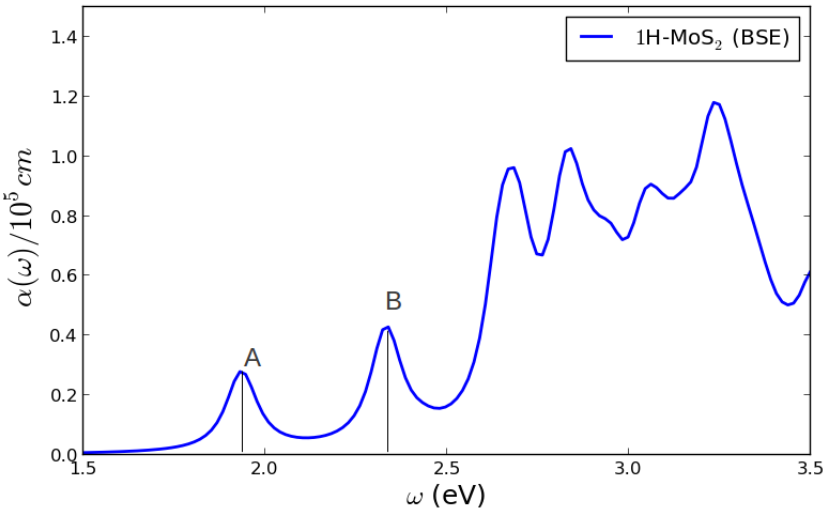


Figure 8.1: Absorption coefficient spectra from BSE calculations for monolayer 1H-$MoTe_2$, as a function of photon energy (ω).

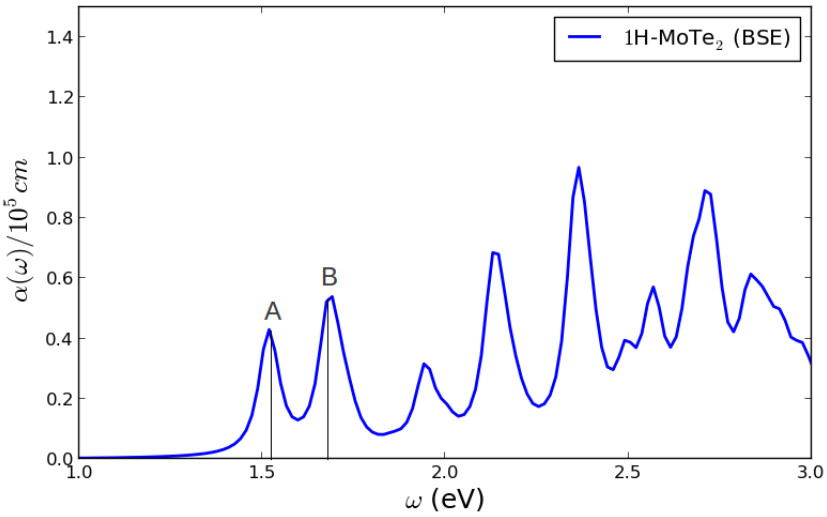


Figure 8.2: Absorption coefficient spectra from BSE calculations for monolayer 1H-$MoSe_2$, as a function of photon energy (ω).

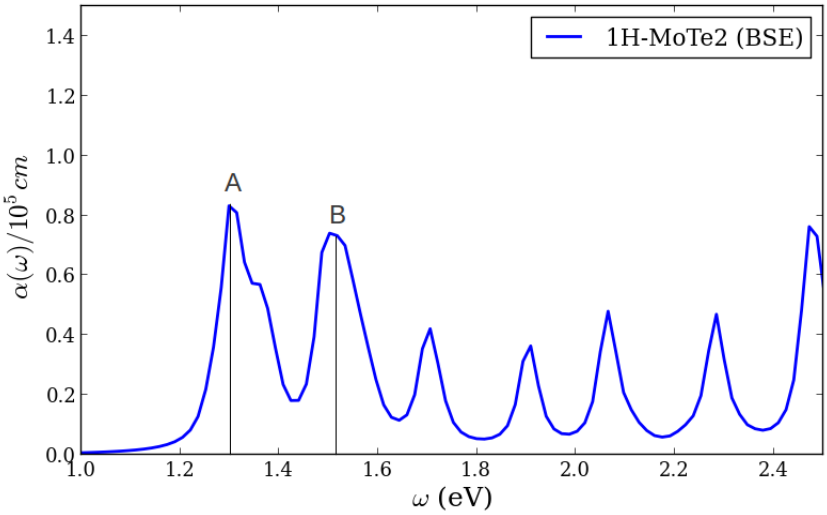


Figure 8.3: Absorption coefficient spectra from BSE calculations for monolayer 1H-$MoTe_2$, as a function of photon energy (ω).

As a first approximation molybdenum chalcogenides monolayers can be treated as 2D materials. The dielectric properties of atomically thin 2D materials are quite different from their 3D counterparts. For example plasmons in 2D metals have acoustic dispersion relations ($\omega_p(q) \longrightarrow 0$ as $q \longrightarrow 0$), and screening is generally much weaker leading to strong exciton binding energies in 2D semiconductors.

The main goal of this part is to attempt to reproduce the experimental absorption spectrum and to examine the exciton binding energy for the 1H-MoX_2 (X = S, Se, Te) family of compounds. In this work, BSE calculations were performed using the VASP implementation in the basis of the G_0W_0 quasielectron and quasihole wave functions. The five highest valence bands and the five lowest conduction bands were used as a basis for excitonic eigenstates, which as been found sufficient to converge the energies of the A and B peaks.

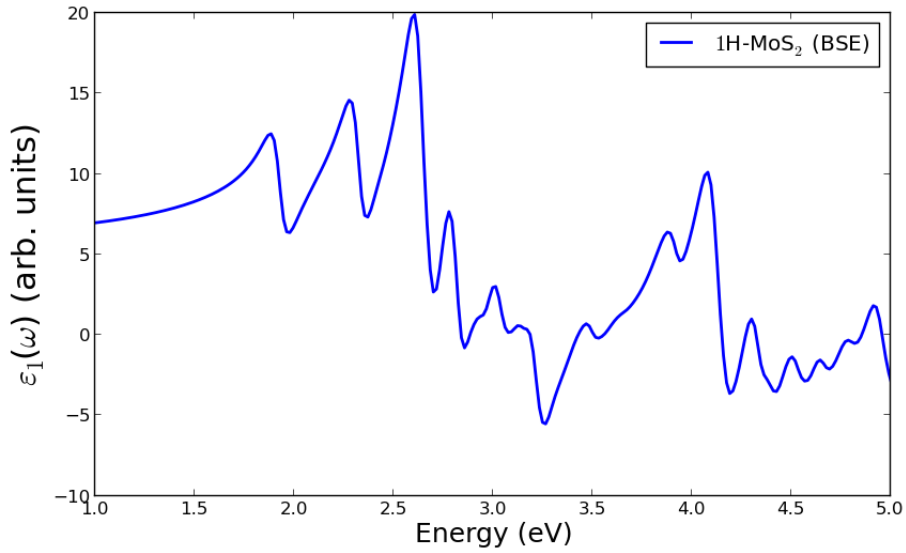


Figure 8.4: Real part of dielectric constant for monolayer 1H-MoS_2, as a function of photon energy ($\hbar\omega$). Computed spectra are presented at the BSE level.

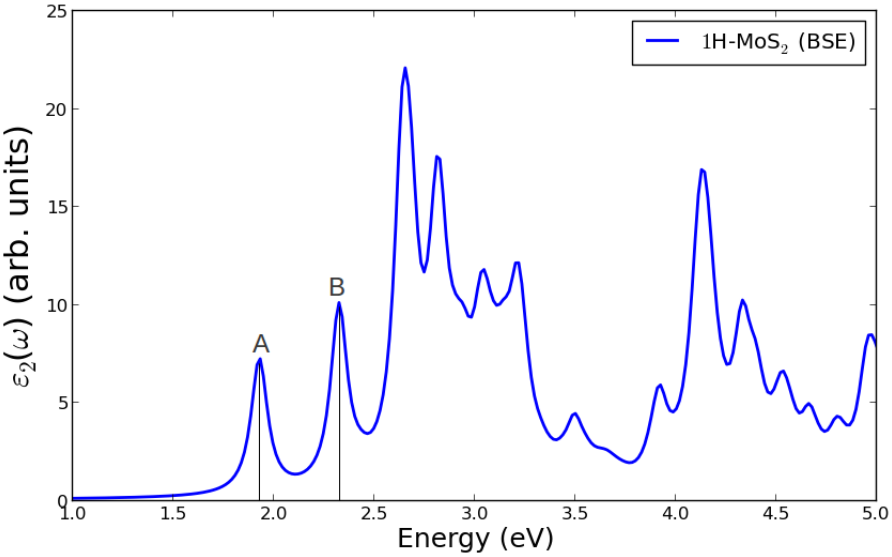


Figure 8.5: Imaginary part of dielectric constant for monolayer 1H-MoS_2, as a function of photon energy ($\hbar\omega$). Computed spectra are presented at the BSE level. The two energy peaks in the spectrum from 1 eV to 2.5 eV correspond to the A and B excitons.

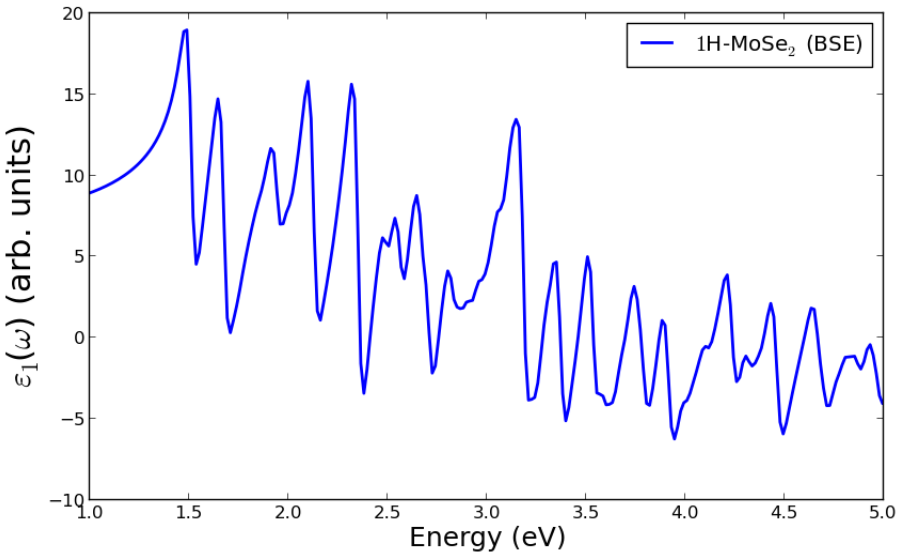


Figure 8.6: Real part of dielectric constant for monolayer 1H-$MoSe_2$, as a function of photon energy ($\hbar\omega$). Computed spectra are presented at the BSE level.

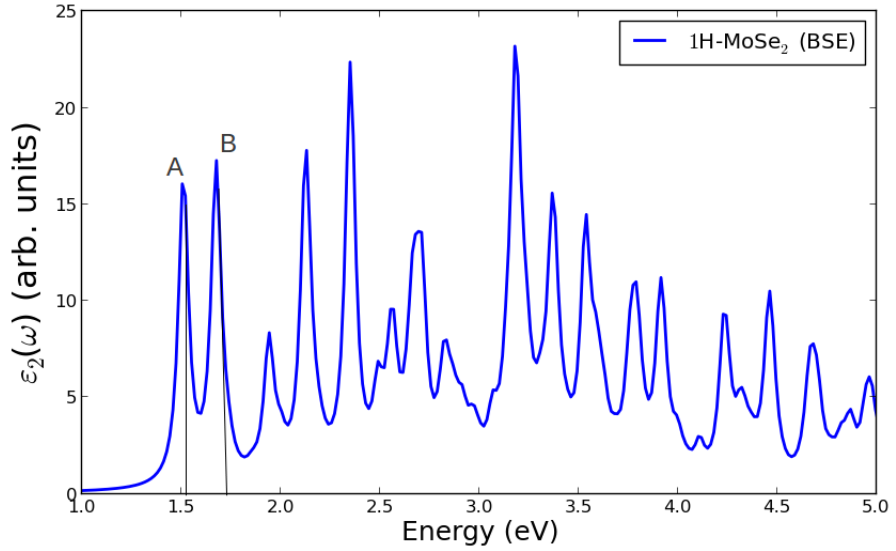


Figure 8.7: Imaginary part of dielectric constant for monolayer 1H-$MoSe_2$, as a function of photon energy ($\hbar\omega$). Computed spectra are presented at the BSE level. The two energy peaks in the spectrum from 1 eV to 2.3 eV correspond to the A and B excitons.

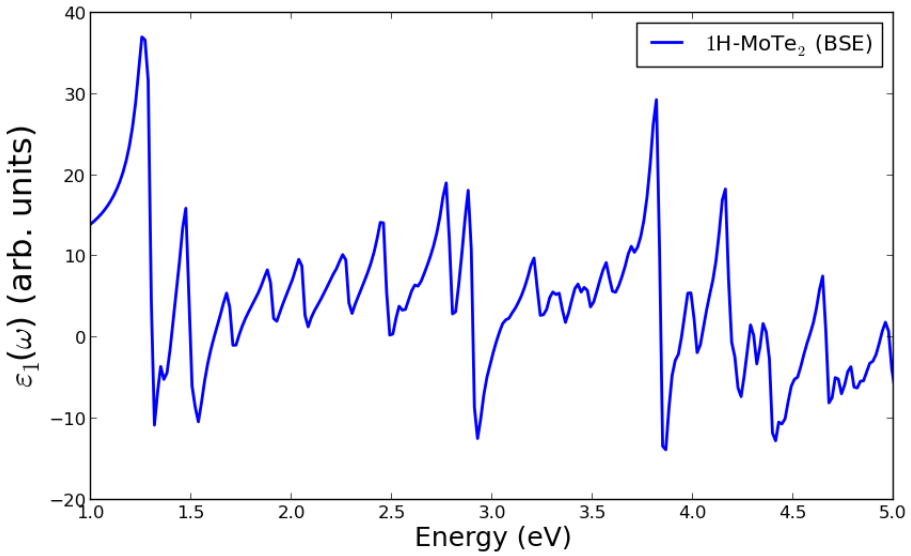


Figure 8.8: Real part of dielectric constant for monolayer 1H-MoTe$_2$, as a function of photon energy ($\hbar\omega$). Computed spectra are presented at the BSE level.

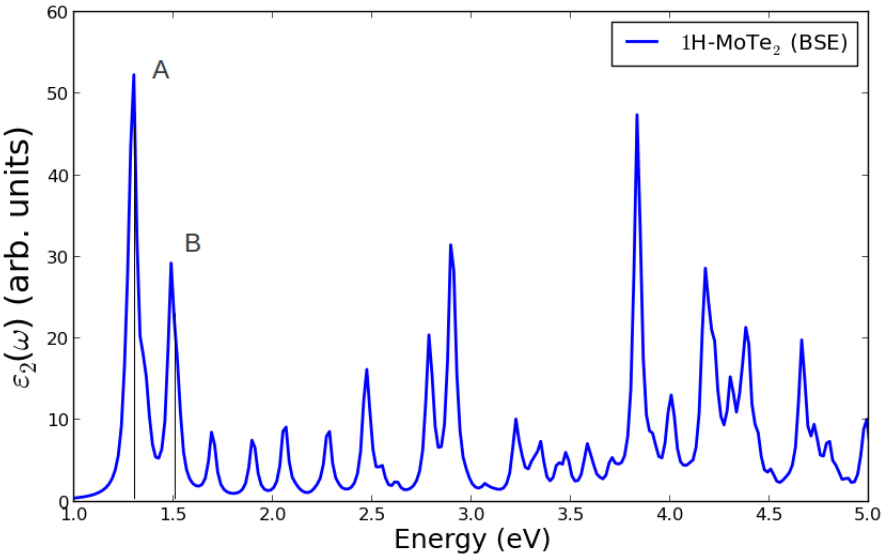


Figure 8.9: Imaginary part of dielectric constant for monolayer 1H-MoTe$_2$, as a function of photon energy ($\hbar\omega$). Computed spectra are presented at the BSE level. The two energy peaks in the spectrum from 1 eV to 1.5 eV correspond to the A and B excitons.

The absorption spectrum of monolayer 1H-MoS_2 is represented graphically in Figure (8.5), which displays the imaginary part of the frequency-depend dielectric constant $\varepsilon_2(\omega)$, in the long wave length limit $q \longrightarrow 0$, which corresponds to interaction with an electromagnetic wave in the plane of the monolayer. We can see the appearance of two distinct absorption peaks at 1.93 eV and 2.32 eV for 1H-MoS_2. Similarly for for 1H-$MoSe_2$ there are absorption peaks at 1.51 eV and 1.78 eV as can be seen in Figure (8.7) 1.29 eV and at from Figure (8.9) there are peaks at 1.49 eV for 1H-$MoTe_2$. These peaks lie within the corresponding G_0W_0 band gaps and correspond to the strongly bound A and B excitons (direct-gap transition at **k**-point of the Brillouin zone between the maximum of the valence band and the minimum of the conduction band) respectively. The positions of these peaks are in good quantitative agreement with experiments as confirmed by the values listed in Table (8.1). Note that the calculated peak energies are insensitive to the DFT approximations used to calculate the DFT input for the GW and BSE calculations.

The difference between our results and the results of reference [100] is probably due to the method used. The authors of reference [100] included of spin-orbit coupling. However, it has previously been shown that the spin-orbit does not have a large effect on the exciton binding energy [108].

Overall we conclude that all monolayer molybdenum chalcogenides 1H-MoX_2 (X =S, Se, Te) studied in this work display the presence of two exciton peak with excitation energies ranging from 1 eV to 2.5 eV, which would suggest possible optical applications in the near-IR to red regime.

Table 8.1: Data from BSE calculations for monolayers 1H-MoX_2 (X = S, Se, Te) calculated in DFT-D2. Transition energy E(eV) for A and B excitons.

	E_A	E_B	Other	Exp (E_A, E_B)
1H-MoS_2				
PBE	1.93	2.32	(1.78 , 1.96)^j	(1.88 , 2.06)^m
DFT-D2	1.93	2.31	(1.78 , 1.96)^j	-
vdW-DF2	1.94	2.33	(1.78 , 1.96)^j	-
1H-$MoSe_2$				
PBE	1.50	1.70	(1.50 , 1.75)^j	(1.57 , 1.82)^n
DFT-D2	1.51	1.78	(1.50 , 1.76)^j	-
vdW-DF2	1.51	1.77	(1.50 , 1.77)^j	-
1H-$MoTe_2$				
PBE	1.29	1.49	(1.06 , 1.36)^j	(1.10 , 1.48)^n
DFT-D2	1.29	1.49	(1.06 , 1.36)^j	-
vdW-DF	1.30	1.50	(1.06 , 1.36)^j	-

^{j}Reference [100]
^{m}Reference [111]
^{n}Reference [113]

We also determined the binding energies for the excitons. The binding energy can be estimated from the difference between the GW band gap and the lowest BSE absorption peaks (Transition energy). The binding energy of the A exciton for 1H-MoS_2 is then estimated to be $E_b^A = E_{gap}^{G_0W_0} - 1.93 = 0.87$ and for the B exciton is estimated to be $E_b^B = E_{gap}^{G_0W_0} - 2.32 = 0.48$. The binding energy of all excitons are listed in Table (8.2). Note that the binding energies are also insensitive to the DFT approximations used in the DFT-GW-BSE ladder of calculations.

Table 8.2: Binding energy E_b for 1H-MoX_2 (X = S, Se, Te) compounds for each exciton in three different approximations.

	Binding energy		
	PBE	DFT-D2	vdW-DF
1H-MoS_2			
E_b^A	0.88	0.87	0.87
E_b^B	0.49	0.49	0.47
1H-$MoSe_2$			
E_b^A	0.98	0.97	0.96
E_b^B	0.70	0.70	0.70
1H-$MoTe_2$			
E_b^A	1.07	1.06	1.06
E_b^B	0.87	0.86	0.86

These results provide direct evidence for strong exciton binding in the 1H-MoX_2 (X = S, Se, Te) monolayers, which was previously inferred in reference [100] using the Mott-Wannier model in conjugaison with GW calculations. Overall, we can say that the G_0W_0-BSE ladder, as employed here, is clearly capable of providing accurate absorption spectra for monolayer molybdenum chalcogenides.

9. Conclusion

In this work we have investigated structural, electronic and optical properties of molybdenum chalcogenides within first principles calculations. We first studied the structural properties for molybdenum chalcogenides in the bulk state 2H-MoX_2 (X = S, Se, Te). DFT calculations in the PBE approximation does not take into account of the long range disperse (van der Waals interaction) forces which are the main form of interaction between layers in these compounds. As a consequence the equilibrium structures calculated with the PBE approximation have too large volumes per unit cell when compared to experiment. However, the inclusion of the van der Waals interaction in the DFT-D2 and vdW-DF approximations significantly improve the structural parameters. Our calculated lattice parameters for the 2H-MoX_2 (X = S, Se, Te) compounds determined with the vdW-DF and DFT-D2 approximations are in good agreement. This confirms that the PBE approximations fails in systems where van der Waals forces are important.

In addition the cohesive energy and the formation energy have shown that these materials are stable and can in principle be synthesized.

In addition the cohesive energy and the formation energy have suggested that these materials are thermodynamically stable and can in principle be synthesized.

Mechanical stability of these compounds have also been investigated using elastic constants. All three 2H-MoX_2 (X = S, Se, Te) compounds were found to be mechanically stable in all three approximations for the exchange correlation used.

The well known band gap problem in which DFT usually underestimates the band gap energy has been confirmed. Our results underestimate the experimental gaps by about 29% - 40%. Also we have shown that the band gap energy increases with increasing volume, thus the obtained gaps from the PBE calculations were found to be larger than with other approximations as well as the experimental values. For comparison we computed the band gaps for PBE at the same volume as the value calculated with DFT-D2 in order to compare these approximations. Again the PBE gaps were larger than DFT-D2 results but smaller than the vdW-DF as well as the experimental ones.

We have demonstrated that many-body perturbation theory in the GW approximation describe the fundamental band gap energy for these compounds more accurately than DFT. The calculated results from GW are larger than to those of DFT. The GW fundamental gaps overestimate the experimental gaps by about 6% - 18%, but the error is significantly lower than for the DFT results.

In their monolayer state 1H-MoX_2 (X = S, Se, Te), GW approximations have been applied as well and the obtained results are in good agreement with the previous results. We have confirmed the observation that the band gap increases when we move from the bulk to a monolayer system. The band gaps calculated for monolayer are larger than the corresponding bulk values by about 1 eV to 1.44 eV. Also the fundamental band gaps (G_0W_0) for monolayer 1H-MoX_2 (X = S, Se, Te) calculated here are much larger than the measured energies for the A and B excitons. Naturally, fundamental band gaps obtained from the GW approach should not be compared with optical transition energies due to the missing electron-hole interaction (excitonic effects). For proper comparison with experiments, we have

calculated the optical transition energies through BSE. Therefore, the last part of our study was focused on the optical properties of monolayer molybdenum chalcogenides within the BSE approximation. The results of the DFT-GW-BSE ladder of calculations were found to be insensitive to the approximation used in the DFT part of the calculations. The presence of strongly bound excitons in monolayer 1H-MoX_2 (X $=$ S, Se, Te) were directly confirmed from these calculations and were shown to be in good agreement with experimental measurements. Overall, the absorption spectra of all monolayers studied in this work indicate the presence of two strongly bound excitonic peaks, which correspond to the excitation energies and are predicted to range from 1 eV to 2.5 eV, which suggests potential applications in the near-IR to the red regime. As experiments on monolayers 1H-MoS_2 have already demonstrated, molybdenum chalcogenides ought to display strong photoluminescence upon thinning down to a monolayer due to an indirect to direct gap transition. Therefore, there is potential for turning electronic and optical properties both via quantum confinement of carriers as well as chemical composition, which then offers promise for new optoelectronic devices.

Appendix A

Bloch Theorem

In the self consistence Kohn-Sham approach, the large number of electrons in a system (macroscopic crystal) prohibits a direct solution of the Schrödinger equation. However, the solid has the periodic symmetry, and this can be accessed to reduce the size of the problem significantly using Bloch's theorem which allows the use of mapping the Schrödinger equation for an infinite periodic solid by solving the Schrödinger equation in a unit cell with a sery of different boundary conditions. The wave function of one electron is symmetric, and can be written as

$$\Psi_{\mathbf{k}}(\mathbf{r}+\mathbf{R}) = e^{i\mathbf{kR}}\Psi_{\mathbf{k}}(\mathbf{r}). \tag{9.0.1}$$

where **R** is the translation vector and can be written as:

$$\mathbf{R} = n_1 a_1 + n_2 a_2 + n_3 a_3 \tag{9.0.2}$$

with $n_i, i = 1, 2, 3$ are integers and a_i, are primitive lattice vectors and collect all equivalent points in space. This set of points is referred to as the Bravais lattice. The primitive unit cell is defined as the volume enclosed by the three primitive vectors:

$$\Omega = |a_1.(a_2 \times a_3)|. \tag{9.0.3}$$

The reciprocal lattice vectors are defined as:

$$a_i b_j = 2\pi\delta_{ij} \tag{9.0.4}$$

where $b_i, i = 1, 2, 3$, the volume of the reciprocal space is given by

$$|b_1.(b_2 \times b_3)| = \frac{(2\pi)^3}{|a_1.(a_2 \times a_3)|} = \frac{(2\pi)^3}{\Omega}. \tag{9.0.5}$$

Similarly to Equation (9.0.2) the vectors which connect all equivalent points in reciprocal space can be defined as

$$\mathbf{G} = m_1 b_1 + m_2 b_2 + m_3 b_3, \tag{9.0.6}$$

where $m_i, i = 1, 2, 3$. We can construct the dot product of any **R** vectors with **G**

$$\mathbf{RG} = 2\pi l, \quad l = n_1 m_1 + n_2 m_2 + n_3 m_3. \tag{9.0.7}$$

Consequently, $e^{i\mathbf{GR}} = 1$. For all **R** and **G** in the Bravais lattice, any function that has a periodicity can be written as

$$f(\mathbf{r}) = \sum_{\mathbf{G}} e^{i\mathbf{Gr}} f(\mathbf{G}) \tag{9.0.8}$$

with $f(\mathbf{G})$ Fourier transform components. Beside, Bloch's theorem assumes that when the potential in the one electron Hamiltonian has the translational periodicity of the Bravais lattice reads

$$V(\mathbf{r}+\mathbf{R}) = V(\mathbf{r}), \tag{9.0.9}$$

the one electron wave function has the same symmetry, so Equation (9.0.1) can be expressed as a product of the phase factor $\exp(i\mathbf{kr})$ multiplied by the function $u_{\mathbf{k}}(\mathbf{r})$ reads

$$\Psi_{\mathbf{k}}(\mathbf{r}) = e^{i\mathbf{kr}} u_{\mathbf{k}}(\mathbf{r}), \quad u_{\mathbf{k}}(\mathbf{r}+\mathbf{R}) = u_{\mathbf{k}}(\mathbf{r}). \tag{9.0.10}$$

The subscript $\mathbf{k}$ is an index for identifying the wave function. Bloch's theorem has two equivalent formulations whose the proof can be found in the book of solid state physics [23].

Projector augmented wave

Projector augmented wave (PAW) has been developed by P. Blöchl in 1994 [107, 53]. Since the wave functions for real materials in different regions of space have very different signatures, for example the bonding region, the wave function is fairly smooth, while close to the nucleus the wave function oscillates rapidly. The idea is to divide the wave function into parts and find a transformation on the wave functions which uses the fictitious wave functions with less oscillations close to the nucleus. It seeks to move from the Hilbert space of wave functions $\{|\Psi_n\rangle\}^4$ solutions of kohn-Sham equations to a pseudo-space (PS) of the wave function of Hilbert $\{|\tilde{\Psi}_n\rangle\}$ which are more softer by a linear transformation:

$$|\Psi_n\rangle = \mathcal{T}|\tilde{\Psi}_n\rangle. \tag{9.0.11}$$

The Kohn-Sham equations take the form

$$\mathcal{T}^\dagger \hat{\mathcal{H}}_s \mathcal{T}|\tilde{\Psi}_n\rangle = \epsilon_n \mathcal{T}^\dagger \mathcal{T}|\tilde{\Psi}_n\rangle, \tag{9.0.12}$$

since the wave function oscillates rapidly near the nuclei we can defined the projector $\mathcal{T}$ as

$$\mathcal{T} = \mathbb{I} + \sum_i \mathcal{T}_{\mathbf{R}_i} \tag{9.0.13}$$

where $\mathbb{I}$ is the identity operator, and $\mathcal{T}_{\mathbf{R}_i}$ is an operator acting within the sphere $\mathcal{S}_{\mathbf{R}_i}$ which surrounds the nuclei i at the points $\mathbf{R}_i$. Thus the wave functions $|\Psi_n\rangle$ and $|\tilde{\Psi}_n$ are identical except in the core regions. In order to define $\mathcal{T}_{\mathbf{R}_i}$, we consider two local basis centred on the nuclei i. The first basis $\{|\phi_i\rangle\}$ is related to the true wave function $|\Psi_n\rangle$ and the second $\{|\tilde{\phi}_i\rangle\}$ to $|\tilde{\Psi}_n\rangle$, therefore we are inside of $\mathcal{S}_{\mathbf{R}_i}$ and we obtain

$$|\Psi_n\rangle = \sum_i c_i|\phi_i\rangle \quad \text{and} \quad |\tilde{\Psi}_n\rangle = \sum_i \tilde{c}_i|\tilde{\phi}_i\rangle \tag{9.0.14}$$

The choice of these basis is define the local transformation the following expression of $|\phi_i\rangle$ as

$$|\phi_i\rangle = (\mathbb{I} + \mathcal{P}_{\mathbf{R}_i})\,|\tilde{\phi}_i\rangle, \tag{9.0.15}$$

therefore

$$\mathcal{T}_{\mathbf{R}_i}|\tilde{\phi}_i\rangle = |\phi_i\rangle - |\tilde{\phi}_i\rangle. \tag{9.0.16}$$

Also, there is no overlapping sphere of PAW, thus inside $\mathcal{S}_{\mathbf{R}_i}$ the wave function of the global system is given by

$$|\phi_i\rangle = \mathcal{T}|\tilde{\phi}_i\rangle = \sum_i \tilde{c}_i|\phi_i\rangle. \tag{9.0.17}$$

On using the unicity $c_i = \tilde{c}_i$, we notice that the wave functions $|\phi_n\rangle$ and $|\tilde{\phi}_n\rangle$ are the same in their basis. In addition $\mathcal{T}$ needs to be linear, it is necessary that c_i must also be linear to $|\tilde{\Psi}\rangle$ i.e there exists a family of projectors $\{|p_i\rangle\}$ such as:

$$c_i = \langle\tilde{p}_i|\tilde{\Psi}_n\rangle. \tag{9.0.18}$$

These projectors respect various properties. It turns out that the spheres of PAW do not overlap, inside of $\mathcal{S}_{\mathbf{R}_i}$ we obtain

$$|\tilde{\Psi}_n\rangle = \sum_i |\tilde{\phi}_n\rangle\langle\tilde{p}_i|\tilde{\Psi}_n\rangle. \tag{9.0.19}$$

Equation (9.0.19) leads to the closure relation reads

$$\sum_i |\tilde{\phi}_i\rangle\langle\tilde{p}_i| = \mathbb{I} \tag{9.0.20}$$

and the orthogonality gives

$$\langle\tilde{p}_i|\tilde{\phi}_j\rangle = \delta_{i,j}. \tag{9.0.21}$$

We do not have the constraint outside of the PAW sphere for the projectors and can be taken as zero in this case the local projector can be written as

$$\mathcal{T}_{\mathbf{R}_i} = \sum_i T_{\mathbf{R}_i}|\tilde{\phi}_i\rangle\langle\tilde{p}_i| \tag{9.0.22}$$

$$= \sum_i \left(|\phi_i\rangle - |\tilde{\phi}_i\rangle\right)\langle\tilde{p}_i|. \tag{9.0.23}$$

In summing considering all nucleus and boundaries conditions the global projector is given by

$$\mathcal{T} = \mathbb{I} + \sum_i \left(|\phi_i\rangle - |\tilde{\phi}_i\rangle\right)\langle\tilde{p}_i|. \tag{9.0.24}$$

In terms of wave functions and their projectors in the real space we obtain

$$\Psi_n(\mathbf{r}) = \tilde{\Psi}_n(\mathbf{r}) + \sum_i \sum_j \phi_j(\mathbf{r} - \mathbf{R}_i) - \tilde{\phi}_j(\mathbf{r} - \mathbf{R}_i)\langle\tilde{p}_j|\tilde{\Psi}_n\rangle \tag{9.0.25}$$

where $\tilde{\Psi}_n$ is obtained from Equation (9.0.12). In summary, the transformation of PAW method is given by Equation (9.0.25). The solutions of Kohn-Sham equations $\hat{\mathcal{H}}_s|\Psi_n\rangle = \epsilon_n|\Psi_n\rangle$, are functions which oscillate slowly far from the nuclei but rapidly close to the core, and they are decomposed as follows

- One part oscillates slowly with $\tilde{\Psi}_n$, solution of $\mathcal{T}^\dagger\hat{\mathcal{H}}_s\mathcal{T}|\Psi_n\rangle = \epsilon_n\mathcal{T}^\dagger\mathcal{T}|\Psi_n\rangle$ and requires a grid in Fourier space much coarser therefore a low cutoff energy.

- Another part oscillates rapidly but localized near the nuclei, which is deduced by projection on a local basis.

This method allows a gain of time for simulation and there is non loss of information on the real wave function.

Observable in the PAW method

We saw that PAW method calculates the wave function on a Fourier space in such a way that it transforms the local problem of eigenvalues of Kohn-Sham. In this part we are going to show how to obtain the observable quantities as expectation values of the pseudo-space wave functions. Let A be an operator and $\tilde{A}$ the associate pseudo-operator. The expectation value is independent on the basis and can be expressed by

$$\langle A\rangle = \sum_n f_n \langle \tilde{\Psi}_n|\tilde{A}|\tilde{\Psi}_n\rangle, \tag{9.0.26}$$

alternatively or as:

$$\langle A\rangle = \sum_n f_n \langle \tilde{\Psi}_n|\tilde{A}|\tilde{\Psi}_n\rangle \tag{9.0.27}$$

where n is the band index and f_n is the occupation of the state. The PS operator takes the form

$$\tilde{A} = \mathcal{T}^\dagger A \mathcal{T} \tag{9.0.28}$$

$$= A + \sum_{i,j} |\tilde{p}_i\rangle \left(\langle \phi_i|A|\phi_j\rangle - \langle \tilde{\phi}_i|A|\tilde{\phi}_j\rangle \right) \langle \tilde{p}_j|. \tag{9.0.29}$$

Also we can add an additional term arbritary in Equation (9.0.28) as:

$$B - \sum_{i,j} |\tilde{p}_i\rangle \langle \tilde{\phi}_i|B|\tilde{\phi}_j\rangle \langle \tilde{p}_j|, \tag{9.0.30}$$

where B is the operator localized in the PAW spheres. This latter equation does not change $\langle A\rangle$ but offers an additional degree of freedom to smooth pseudo-wave function. If we consider the projection operator $|\mathbf{r}\rangle\langle,\mathbf{r}|$ we obtain the charge density which follows the description given in Equation (9.0.28), hence the charge density is given by

$$n(\mathbf{r}) = \tilde{n}(\mathbf{r}) + n^1(\mathbf{r}) - \tilde{n}^1(\mathbf{r}), \tag{9.0.31}$$

where $\tilde{n}(\mathbf{r})$ is soft PS charge density given by

$$\tilde{n}(\mathbf{r}) = \sum_n f_n \langle \tilde{\Psi}_n|\mathbf{r}\rangle\langle \mathbf{r}|\tilde{\Psi}_n\rangle. \tag{9.0.32}$$

The quantities $\tilde{n}(\mathbf{r})$ and $\tilde{n}(\mathbf{r})$ are defined as

$$n^1(\mathbf{r}) = \sum_i \sum_{(n,j),k} f_n \langle \tilde{\Psi}_n|\tilde{p}_j\rangle\langle \phi_j|\mathbf{r}\rangle\langle \mathbf{r}|\phi_k\rangle\langle \tilde{p}_k|\tilde{\Psi}_n\rangle, \tag{9.0.33}$$

and

$$\tilde{n}^1(\mathbf{r}) = \sum_i \sum_{(n,j),k} f_n \langle \tilde{\Psi}_n | \tilde{p}_j \rangle \langle \tilde{\phi}_j | \mathbf{r} \rangle \langle \mathbf{r} | \tilde{\phi}_k \rangle \langle \tilde{p}_k | \tilde{\Psi}_n \rangle. \tag{9.0.34}$$

Equation (9.0.31) represents the charge density at point **r**, it is the expectation value of the real space projection operator $|\mathbf{r}\rangle\langle\mathbf{r}|$ and described one of the physical quantity in the PAW method.

Appendix B

Brillouin zone and k-points

The Bloch'stheorem changes the problem of calculating an infinite number of electronic wave functions to one of calculating a finite number of electronic wave functions at an infinite number of **k** points [116]. Beside the Brillouin zone is the volume in which the boundaries are defined by the planes that bisect vectors from the origin of the reciprocal lattice to its closest reciprocal unit cell. The volume of the the Brillouin zone is equal to that of the reciprocal unit cell [117], evaluation of many quantities such as energy or density requires the integration over the brillouin zone with discrete set of **k** points [19]. Chad and Cohen have discussed methods for finding sets of **k** points [118]. Nowadays the most widely used method has been proposed by Monkhorst and Pack which provides an accurate integration and leads to an uniform set of **k** points determined by the formulation valid for any crystal (in three dimensions)

$$\mathbf{k}_{n_1,n_2,n_3} = \sum_{i}^{3} \frac{2n_i - N - 1}{2N} G_i \tag{9.0.35}$$

where G_i are the primitive vectors of the reciprocal lattice, $n_i = 1, 2, \ldots, N$. The energy is more difficult to calculate for metallic system because the metals require careful integration near the Fermi surface, thus **k** points are required to define the Fermi surface precisely, and lattice constants of solids [64, 119].

Ionic center and Pseudopentials

Now we have seen an approximation which allows us to calculate the total energy of a system with the approach of Kohn-Sham in DFT. Moreover, to solve the equations of Kohn-Sham we use the self-consistency as pointed in section $2.4.3$ from which we consider the development of wave functions in the plane wave basis sets $e^{i(\mathbf{K}+\mathbf{G})\mathbf{r}}$. The choice of the plane wave basis sets is done by considering that all plane waves whose kinetic energy is less than a certain limit called the cutoff energy, so that

$$\mathbf{K}^2 + \mathbf{G}^2 \leq E_{cutoff}. \tag{9.0.36}$$

The complete plane wave basis sets is obtained by increasing E_{cutoff} which is the critical parameter for the time calculation. Thus to optimize the simulation we must find how to reduce E_{cutoff}. However, it is near the nucleus that the most rapid variations of the electronic wave function are expected. Indeed, near the nucleus the coulomb potential tends to infinity. In quantum mechanics, the more the potential is deeper the more the wave function oscillates at high frequency. We can not deal with the part close to the nucleus, this is particularly where the electrons are core and play an important role in electronic structure. Several techniques have been proposed for electronic structure calculation in DFT, from orthogonalized plane wave methods [120] to the norm-conserving pseudopotential [94, 93] which provide better transferability of pseudopotential for different cases such as isolated atom, molecules ions,

and crystal. A brief description of these techniques can be found in the book of R.Martin [19] as well as their advantages and disadvantages. One major disadvantage is that there is a loss of information between the real wave function and the calculated wave function. In this work we have used an efficient method for describing electrons valence based on rigorous mathematical transformation called projector augmented wave method (PAW see annex A).

Appendix C

The crystal structure of molybdenum chalcogenides

At room temperature and normal pressure, the bulk crystal of molybdenum chalcogenides MoX_2 (X = S, Se, Te) crystallise in the 2H-MoX_2 hexagonal structure (Figure (9.1)) with space group $P6_3/mmc$ corresponding to space group number 194. They are made up of layered van der Walls-bonded X-Mo-X units. Each of these stable units is referred to as a 1H-MoX_2 monolayer, consisting of two hexagonal planes of chalcohogen (X) atoms and an interaction hexagonal plane of molybdenum (Mo). Also Mo atom falls in the center of the trigonal prismatic coordination. Since the interactions between the layers are weak and strong within the layers, an interesting anisotropic behaviour, the formation of ultrathin crystals of 1H-MoX_2 by the micromechanical cleavage technique has been achieved by Novoselov et al. They extracted 6.5 Å thick monolayers with a honeycomb structure.

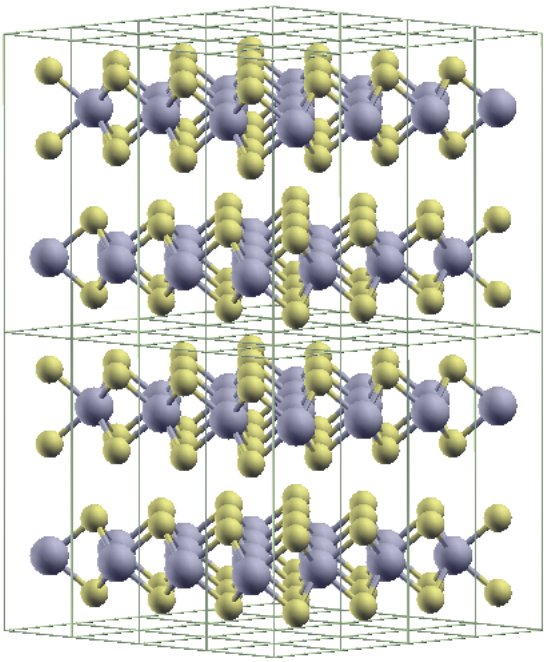


Figure 9.1: Side view of 2H-MoX_2 structure where the big and small balls represent Mo and X (S, Se, Te) atoms respectively.

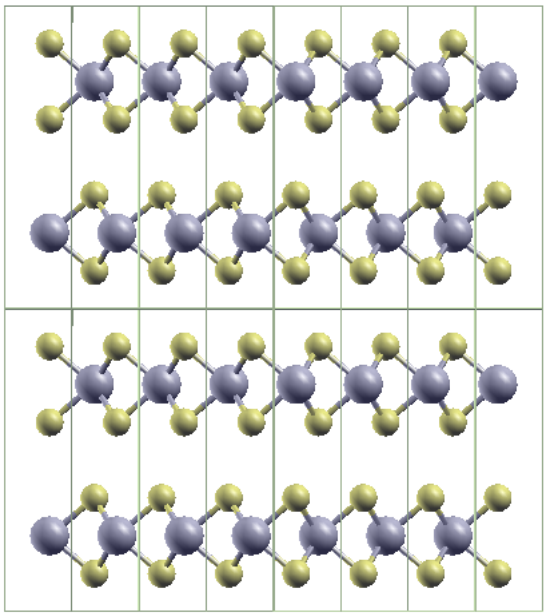


Figure 9.2: Top view of 2H-MoX_2 structure where the big and small balls represent Mo and X (S, Se, Te) atoms respectively.

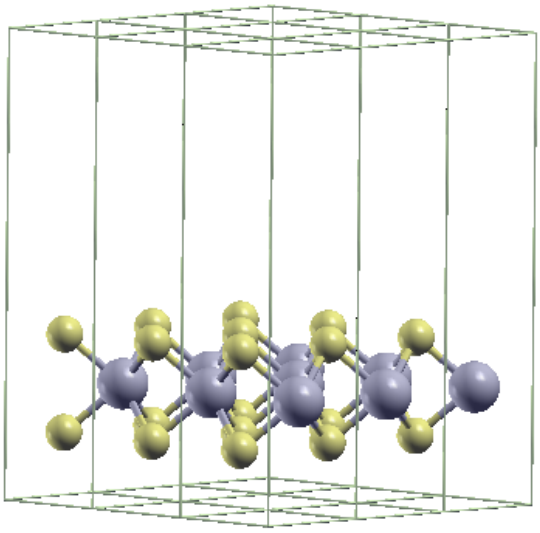


Figure 9.3: Side view of 1H-MoX_2 structure where the big and small balls represent Mo and X (S, Se, Te) atoms respectively.

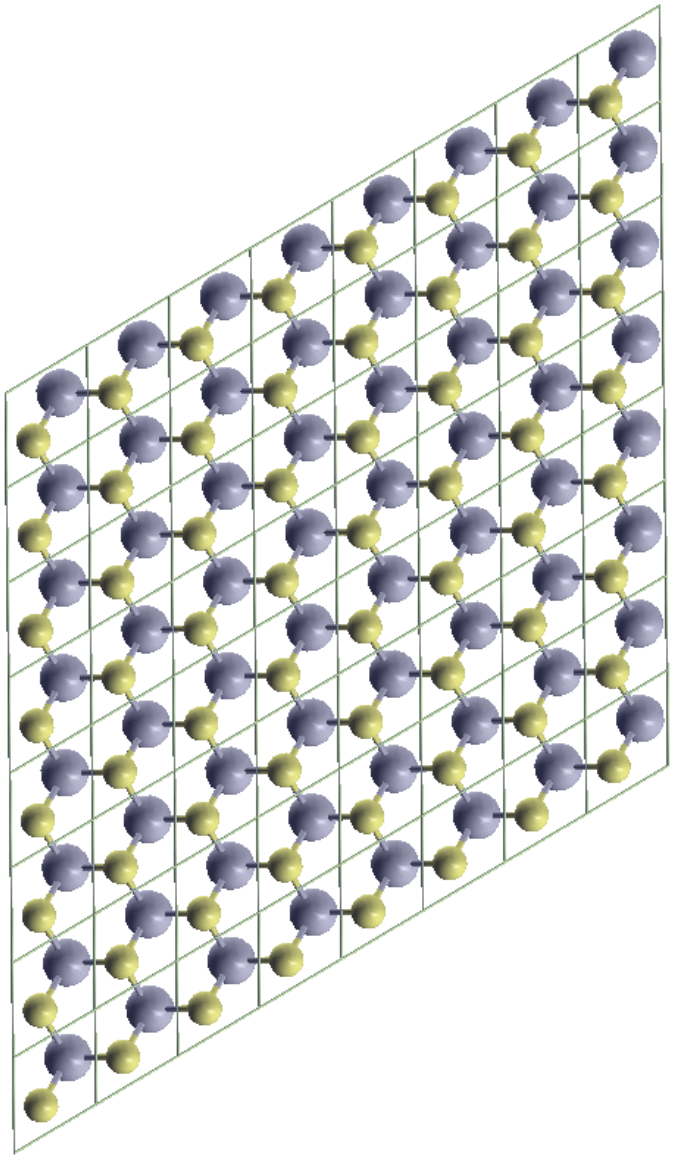


Figure 9.4: Top view of 1H-MoX_2 structure where the big and small balls represent Mo and X (S, Se, Te) atoms respectively.

Appendix D

Charge density

We present in this part the charge density calculated in the 110 plane for both bulk 2H-MoX_2 (X = S, Se, Te) and monolayer 1H-MoX_2 (X = S, Se, Te). The charge density is graphically represented in the Figures (9.5), (9.6), and (9.7). The latter Figures describe the electron localization function (ELF) that allows us to quantitatively analyse the nature of the chemical bounding. Therefore in both systems the grade of the (ELF) [121] has the same features. If we consider more specially the Figure (9.5), the ELF is encoded using a colour scheme in which high values correspond to green and low values to red. The site of the Mo cation is characterized by the low values of ELF; whereas X sites display green annular regions. The difference in ELF is a signature of an ionic kind of chemical bonding [122].
Besides that, there are also lobes between the adjacent X anions either in the same layer or in two layers. Thus, the bonding between Mo and X is a mixture of ionic and covalent bonds, and there are also slight covalent characteristic bonds between the adjacent X anions.

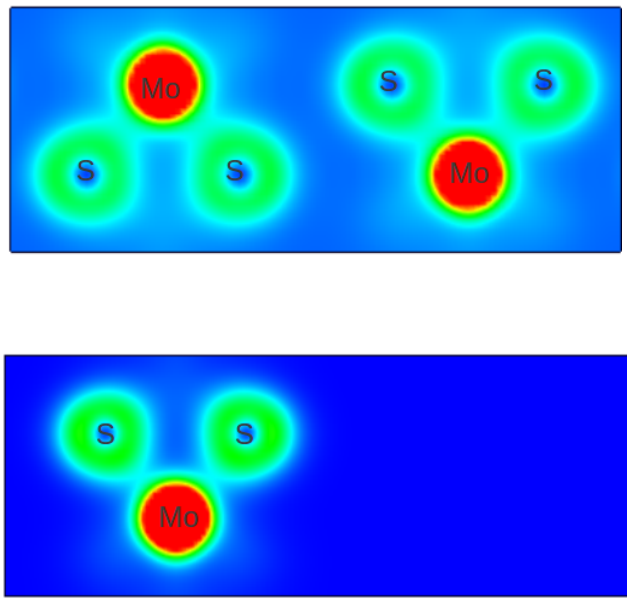


Figure 9.5: Top, charge density for 2H-MoS_2 and bottom, charge density for 1H-MoS_2 calculated in 110 plane .

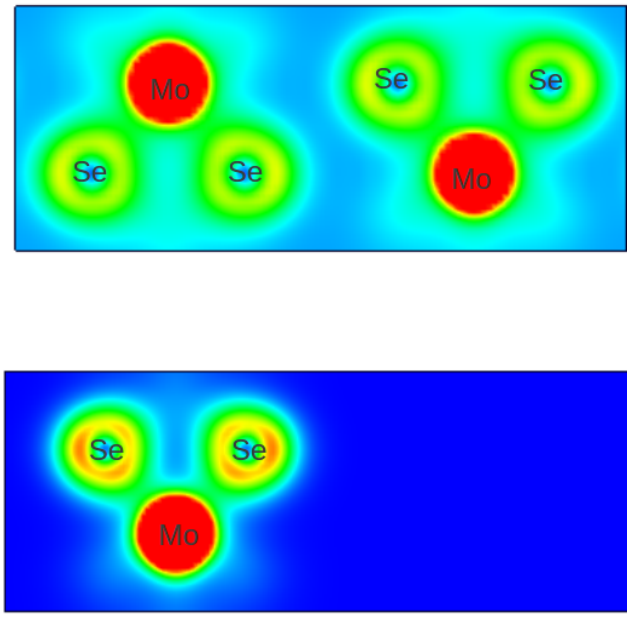


Figure 9.6: Top, charge density for 2H-$MoSe_2$ and bottom, charge density for 1H-$MoSe_2$ calculated in 110 plane .

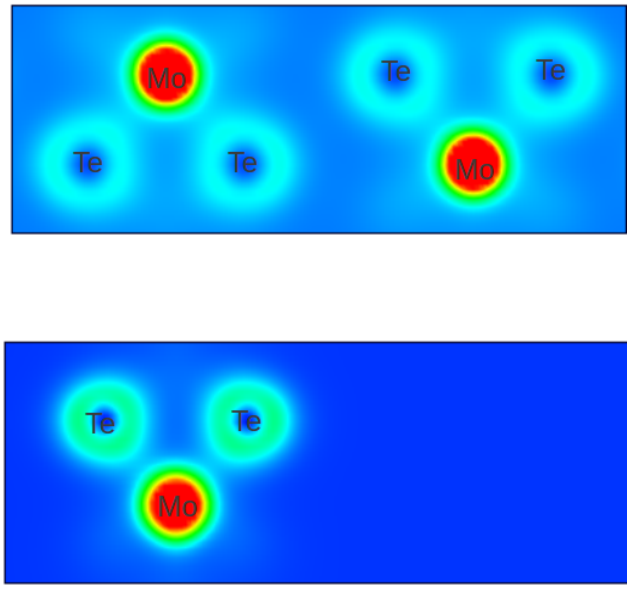
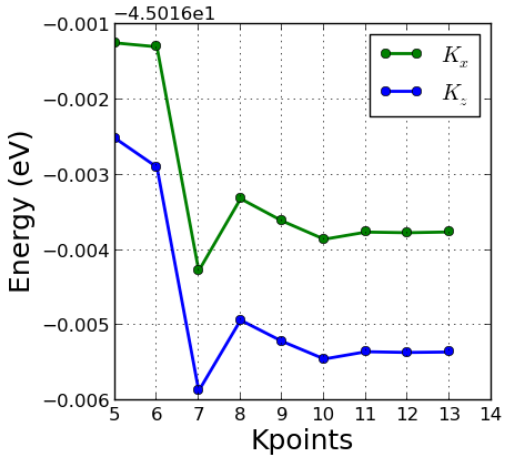


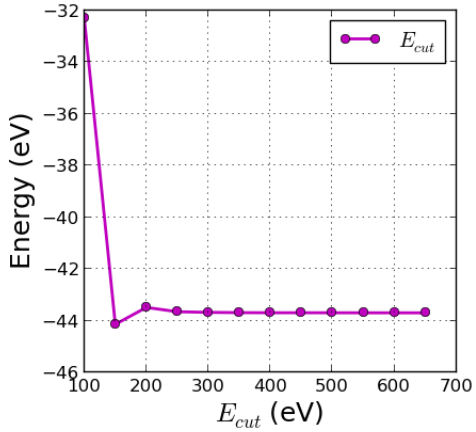
Figure 9.7: Top, charge density for 2H-$MoTe_2$ and bottom, charge density for 1H-$MoTe_2$ calculated in 110 plane .

Appendix E

Convergence Test

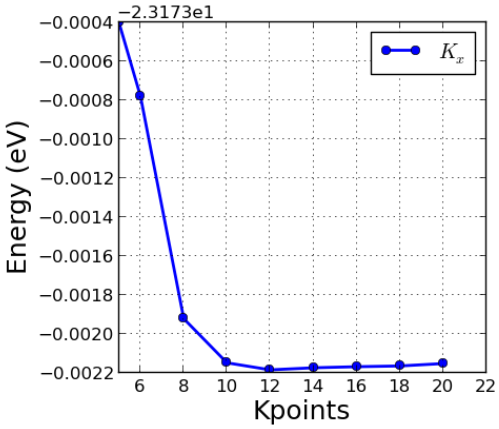


(a)

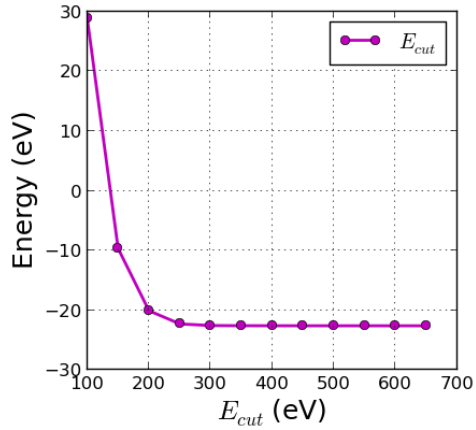


(b)

Figure 9.8: Convergence test for bulk 2H-MoX_2 (X = S, Se, Te): (a), total energy E versus Kpoints (K_x represents the component of kpoints along x direction, and K_z represents the component of kpoints along z direction). (b), total energy E versus energy cuttoff (E_{cut}, using $9 \times 9 \times 1$, and $9 \times 9 \times 2$ Γ - centered Monkorst-Pack mesh)



(c)



(d)

Figure 9.9: Convergence test for monolayer 1H-MoX_2 (X = S, Se, Te): (c), total energy E versus Kpoints (K_x represents the component of kpoints along x direction). (d), total energy E versus energy cuttoff (E_{cut}, using $12 \times 12 \times 1$ Γ - centered Monkorst-Pack mesh)

References

[1] A. Kumar and P. Ahluwalia, "Electronic structure of transition metal dichalcogenides monolayers $\mathrm{MX_2}$ ($\mathrm{M = Mo, W;\ X = S, Se, Te}$) from ab-initio theory: new direct band gap semiconductors," *The European Physical Journal B-Condensed Matter and Complex Systems*, vol. 85, no. 6, pp. 1–7, 2012.

[2] O. Sedelnikova, L. Bulusheva, and A. Okotrub, "Ab initio study of dielectric response of rippled graphene," *The Journal of chemical physics*, vol. 134, no. 24, pp. 244707–244707, 2011.

[3] D. Late, B. Liu, H. Matte, C. Rao, and V. Dravid, "Rapid characterization of ultrathin layers of chalcogenides on $\mathrm{SiO_2}/Si$ substrates," *Advanced Functional Materials*, 2012.

[4] K. Novoselov, D. Jiang, F. Schedin, T. Booth, V. Khotkevich, S. Morozov, and A. Geim, "Two-dimensional atomic crystals," *Proceedings of the National Academy of Sciences of the United States of America*, vol. 102, no. 30, pp. 10451–10453, 2005.

[5] A. Ayari, E. Cobas, O. Ogundadegbe, and M. Fuhrer, "Realization and electrical characterization of ultrathin crystals of layered transition-metal dichalcogenides," *Journal of applied physics*, vol. 101, no. 1, pp. 014507–014507, 2007.

[6] B. Miremadi and S. Morrison, "The intercalation and exfoliation of tungsten disulfide," *Journal of applied physics*, vol. 63, no. 10, pp. 4970–4974, 1988.

[7] B. Radisavljevic, A. Radenovic, J. Brivio, V. Giacometti, and A. Kis, "Single-layer $\mathrm{MoS_2}$ transistors," *Nature nanotechnology*, vol. 6, no. 3, pp. 147–150, 2011.

[8] B. Van Zeghbroeck, "Principles of electronic devices," *University of Colorado*, 2011.

[9] H. Jiang, "Electronic band structures of molybdenum and tungsten dichalcogenides by the *GW* approach," *The Journal of Physical Chemistry C*, vol. 116, no. 14, pp. 7664–7671, 2012.

[10] T. Böker, R. Severin, A. Müller, C. Janowitz, R. Manzke, D. Voß, P. Krüger, A. Mazur, and J. Pollmann, "Band structure of $\mathrm{MoS_2}$, $\mathrm{MoSe_2}$, and α-$\mathrm{MoTe_2}$: Angle-resolved photoelectron spectroscopy and ab initio calculations," *Physical Review B*, vol. 64, no. 23, p. 235305, 2001.

[11] M. Ernzerhof and G. Scuseria, "Assessment of the perdew–burke–ernzerhof exchange-correlation functional," *The Journal of chemical physics*, vol. 110, p. 5029, 1999.

[12] A. Seidl, A. Görling, P. Vogl, J. Majewski, and M. Levy, "Generalized kohn-sham schemes and the band-gap problem," *Physical Review B*, vol. 53, no. 7, p. 3764, 1996.

[13] F. Aryasetiawan and O. Gunnarsson, "The *GW* method," *Reports on Progress in Physics*, vol. 61, no. 3, p. 237, 1999.

[14] S. M. Delphine, M. Jayachandran, C. Sanjeeviraja, and A. Almusallam, "Study on $(\mathrm{Mo/W})$ $\mathrm{Se_2}$ layered compound semi conductors useful for photoelectrochemical solar cells," *International Journal of ChemTech Research*, vol. 3, pp. 846–852, 2011.

[15] C. BALLIF, "Electrical, and optical properties of thin films of $\mathrm{WS_2}$ et $\mathrm{MoS_2}$ for photovoltaic applications.,"

[16] J. I. Pankove, *Optical processes in semi-conductors*. DoverPublications. com, 1971.

[17] X. Mathew, J. Enriquez, A. Romeo, and A. Tiwari, "$\mathrm{CdTe/CdS}$ solar cells on flexible substrates," *Solar energy*, vol. 77, no. 6, pp. 831–838, 2004.

[18] H. Jiang, "Structural and electronic properties of $\mathrm{ZrX_2}$ and $\mathrm{HfX_2}$ $(\mathrm{X = S}$ and $\mathrm{Se})$ from first principles calculations," *The Journal of Chemical Physics*, vol. 134, p. 204705, 2011.

[19] R. Martin, *Electronic structure: basic theory and practical methods*. Cambridge university press, 2004.

[20] J. Hafner, C. Wolverton, and G. Ceder, "Toward computational materials design: the impact of density functional theory on materials research," *MRS bulletin*, vol. 31, no. 09, pp. 659–668, 2006.

[21] J. Thijssen, *Computational physics*. Cambridge University Press, 2007.

[22] P. Murdin, "Pauli exclusion principle," *Encyclopedia of Astronomy and Astrophysics*, vol. 1, p. 4896, 2000.

[23] E. Kaxiras, *Atomic and electronic structure of solids*. Cambridge University Press, 2003.

[24] P. Hohenberg and W. Kohn, "Inhomogeneous electron gas," *Physical Review*, vol. 136, no. 3B, p. B864, 1964.

[25] J. Kohanoff, *Electronic structure calculations for solids and molecules: theory and computational methods*. Cambridge University Press, 2006.

[26] M. Levy, "Electron densities in search of hamiltonians," *Physical Review A*, vol. 26, no. 3, p. 1200, 1982.

[27] W. Kohn and L. Sham, *Self-consistent equations including exchange and correlation effects*. APS, 1965.

[28] W. Koch, M. C. Holthausen, and M. C. Holthausen, *A chemist's guide to density functional theory*, vol. 2. Wiley-Vch Weinheim, 2001.

[29] P. Dirac, "Note on exchange phenomena in the thomas atom," in *Proceedings of the Cambridge Philosophical Society*, vol. 26, p. 376, 1930.

[30] U. von Barth and L. Hedin, "A local exchange-correlation potential for the spin polarized case," *Journal of Physics C: Solid State Physics*, vol. 5, no. 13, p. 1629, 1972.

[31] D. Ceperley and B. Alder, "Ground state of the electron gas by a stochastic method," *Physical Review Letters*, vol. 45, no. 7, pp. 566–569, 1980.

[32] S. H. Vosko, L. Wilk, and M. Nusair, "Accurate spin-dependent electron liquid correlation energies for local spin density calculations: a critical analysis," *Canadian Journal of Physics*, vol. 58, no. 8, pp. 1200–1211, 1980.

[33] J. P. Perdew, K. Burke, and Y. Wang, "Generalized gradient approximation for the exchange-correlation hole of a many-electron system," *Physical Review B*, vol. 54, no. 23, p. 16533, 1996.

[34] J. Perdew, "Electronic structure of solids 91, edited by *Ziesche, P. and Eschrig, H.*(berlin: Akademie-verlag) p. 11;*Perdew, JP and Wang, Y.*, 1992," *Phys. Rev. B*, vol. 45, no. 13, p. 244, 1991.

[35] J. Hafner, "Ab-initio simulations of materials using vasp: Density-functional theory and beyond," *Journal of computational chemistry*, vol. 29, no. 13, pp. 2044–2078, 2008.

[36] M. Molepo, *Computational study of the structural phase transitions and pressure dependent electronic structure of* ZnO. PhD thesis, School of Physics, University of the Witwatersrand, 2012.

[37] R. Armiento, "From exchange-correlation functional design to applied electronic structure calculations," 2005.

[38] S. Park, B. Lee, S. H. Jeon, and S. Han, "Hybrid functional study on structural and electronic properties of oxides," *Current Applied Physics*, vol. 11, no. 3, pp. S337–S340, 2011.

[39] J. Paier, M. Marsman, K. Hummer, G. Kresse, I. C. Gerber, and J. G. Ángyán, "Screened hybrid density functionals applied to solids," *The Journal of chemical physics*, vol. 124, p. 154709, 2006.

[40] S. Grimme, "Semiempirical *GGA*-type density functional constructed with a long-range dispersion correction," *Journal of computational chemistry*, vol. 27, no. 15, pp. 1787–1799, 2006.

[41] S. Grimme, J. Antony, S. Ehrlich, and H. Krieg, "A consistent and accurate ab initio parametrization of density functional dispersion correction (*DFT-D*) for the 94 elements *H-Pu*," *The Journal of Chemical Physics*, vol. 132, p. 154104, 2010.

[42] U. Zimmerli, M. Parrinello, and P. Koumoutsakos, "Dispersion corrections to density functionals for water aromatic interactions," *The Journal of chemical physics*, vol. 120, p. 2693, 2004.

[43] H. Rydberg, M. Dion, N. Jacobson, E. Schröder, P. Hyldgaard, S. Simak, D. C. Langreth, and B. I. Lundqvist, "Van der waals density functional for layered structures," *Physical review letters*, vol. 91, no. 12, p. 126402, 2003.

[44] J. Klimeš, D. R. Bowler, and A. Michaelides, "Van der waals density functionals applied to solids," *Physical Review B*, vol. 83, no. 19, p. 195131, 2011.

[45] K. Lee, É. D. Murray, L. Kong, B. I. Lundqvist, and D. C. Langreth, "Higher-accuracy van der waals density functional," *Physical Review B*, vol. 82, no. 8, p. 081101, 2010.

[46] R. P. SINGH and R. K. SINGH, "Structural, elastic and electronic properties of neodymium chalcogenides (NdX, $\mathrm{X} = \mathrm{S}, \mathrm{Se}, \mathrm{Te}$): First principles study," *Chalcogenide Letters*, vol. 8, no. 5, pp. 325–340, 2011.

[47] M. Rabah, S. Benalia, D. Rached, B. Abidri, H. Rached, and G. Vergoten, "Prediction of stabilities phase and elastic properties of palladium carbide," *Computational Materials Science*, vol. 48, no. 3, pp. 556–562, 2010.

[48] G. Pilania and V. Sharma, "First principles investigations of structural, electronic, elastic, and dielectric properties of $\mathrm{KMgF_3}$," *Journal of Materials Science*, vol. 48, no. 21, pp. 7635–7641, 2013.

[49] L. Fast, J. Wills, B. Johansson, and O. Eriksson, "Elastic constants of hexagonal transition metals: Theory," *Physical Review B*, vol. 51, no. 24, p. 17431, 1995.

[50] M. Levy, H. Bass, and R. Stern, *Modern acoustical techniques for the measurement of mechanical properties*, vol. 39. Academic Press, 2001.

[51] E. Tsymbal, "Physics 927: Introduction to solid state physics course lectures $1-5$, web site: http://physics. unl. edu /teaching/ssp927," *Section*$\%2005$ *Vibrations. pdf*.

[52] G. Kresse and J. Furthmuller, "Vasp the guide," *Vienna University of Technology, Vienna*, 2001.

[53] G. Kresse and D. Joubert, "From ultrasoft pseudopotentials to the projector augmented-wave method," *Physical Review B*, vol. 59, no. 3, p. 1758, 1999.

[54] P. Vinet, J. H. Rose, J. Ferrante, and J. R. Smith, "Universal features of the equation of state of solids," *Journal of Physics: Condensed Matter*, vol. 1, no. 11, p. 1941, 1989.

[55] P. Vinet, J. R. Smith, J. Ferrante, and J. H. Rose, "Temperature effects on the universal equation of state of solids," *Physical Review B*, vol. 35, no. 4, p. 1945, 1987.

[56] A. F. Guillermet, "Thermodynamic properties of the generalized murnaghan equation of state of solids," *International journal of thermophysics*, vol. 16, no. 4, pp. 1009–1026, 1995.

[57] M. S. Suleiman, M. P. Molepo, and D. P. Joubert, "A theoretical investigation of structural, electronic and optical properties of bulk copper nitrides," *arXiv preprint arXiv:1211.0179*, 2012.

[58] J. Calloway and G. G. Johnson Jr, "Energy band theory," *Physics Today*, vol. 17, p. 61, 1964.

[59] J. P. Perdew, "Density functional theory and the band gap problem," *International Journal of Quantum Chemistry*, vol. 28, no. S19, pp. 497–523, 1985.

[60] M. Chan and G. Ceder, "Efficient band gap prediction for solids," *Physical review letters*, vol. 105, no. 19, p. 196403, 2010.

[61] C. Wang and W. Pickett, "Density-functional theory of excitation spectra of semiconductors: Application to si," *Physical review letters*, vol. 51, no. 7, pp. 597–600, 1983.

[62] M. S. Hybertsen and S. G. Louie, "Electron correlation in semiconductors and insulators: Band gaps and quasiparticle energies," *Physical Review B*, vol. 34, no. 8, p. 5390, 1986.

[63] R. Godby and R. Needs, "Metal-insulator transition in kohn-sham theory and quasiparticle theory," *Physical review letters*, vol. 62, no. 10, pp. 1169–1172, 1989.

[64] C. Fiolhais, F. Nogueira, and M. Marques, *A primer in density functional theory*, vol. 620. Springer, 2003.

[65] L. Sham and M. Schlüter, "Density-functional theory of the energy gap," *Physical Review Letters*, vol. 51, no. 20, p. 1888, 1983.

[66] M. Dresselhaus, "Optical properties of solids," *Proceedings of the International School of Physics" Enrico Fermi," J. Tauc, Editor (Academic Press. NY. 1966)*, 1966.

[67] D. Varsano, *First principles description of response functions in low dimensional systems*. PhD thesis, Thesis, University of the Basque Country, 2006.

[68] C. Friedrich and A. Schindlmayr, "Many-body perturbation theory: The *GW* approximation," *NIC Series*, vol. 31, p. 335, 2006.

[69] R. Godby, M. Schlüter, and L. Sham, "Self-energy operators and exchange-correlation potentials in semiconductors," *Physical Review B*, vol. 37, no. 17, p. 10159, 1988.

[70] D. Turnbull, *Solid state physics*, vol. 9. Academic Press, 1959.

[71] M. Shishkin and G. Kresse, "Implementation and performance of the frequency-dependent *GW* method within the paw framework," *Physical Review B*, vol. 74, no. 3, p. 035101, 2006.

[72] G. Onida, L. Reining, and A. Rubio, "Electronic excitations: density-functional versus many-body greens-function approaches," *Reviews of Modern Physics*, vol. 74, no. 2, p. 601, 2002.

[73] S. Albrecht, L. Reining, R. Del Sole, and G. Onida, "Ab initio calculation of excitonic effects in the optical spectra of semiconductors," *arXiv preprint cond-mat/9803194*, 1998.

[74] J. R. Lince, H. I. Kim, P. M. Adams, D. J. Dickrell, and M. T. Dugger, "Nanostructural, electrical, and tribological properties of composite $\mathrm{Au\ MoS_2}$ coatings," *Thin Solid Films*, vol. 517, no. 18, pp. 5516–5522, 2009.

[75] J. A. Spirko, M. L. Neiman, A. M. Oelker, and K. Klier, "Electronic structure and reactivity of defect $\mathrm{MoS_2}$: I. relative stabilities of clusters and edges, and electronic surface states," *Surface science*, vol. 542, no. 3, pp. 192–204, 2003.

[76] S. Lebegue and O. Eriksson, "Electronic structure of two-dimensional crystals from ab initio theory," *Physical Review B*, vol. 79, no. 11, p. 115409, 2009.

[77] S. Bhattacharyya and A. K. Singh, "Semiconductor-metal transition in semiconducting bilayer sheets of transition-metal dichalcogenides," *Physical Review B*, vol. 86, no. 7, p. 075454, 2012.

[78] G. Román-Pérez and J. M. Soler, "Efficient implementation of a van der waals density functional: application to double-wall carbon nanotubes," *Physical review letters*, vol. 103, no. 9, p. 096102, 2009.

[79] S. P. Ong, W. D. Richards, A. Jain, G. Hautier, M. Kocher, S. Cholia, D. Gunter, V. L. Chevrier, K. A. Persson, and G. Ceder, "Python materials genomics (pymatgen): A robust, open-source python library for materials analysis," *Computational Materials Science*, vol. 68, pp. 314–319, 2013.

[80] M. Born and R. Oppenheimer, "Zur quantentheorie der molekeln," *Annalen der Physik*, vol. 389, no. 20, pp. 457–484, 1927.

[81] R. Feynman, "Forces in molecules," *Physical Review*, vol. 56, no. 4, p. 340, 1939.

[82] H. L. Zhuang and R. G. Hennig, "Computational search for single-layer transition-metal dichalcogenide photocatalysts," *The Journal of Physical Chemistry C*, vol. 117, no. 40, pp. 20440–20445, 2013.

[83] T. Li, "Ideal strength and phonon instability in single-layer $\mathrm{MoS_2}$," *Physical Review B*, vol. 85, no. 23, p. 235407, 2012.

[84] M. Hebbache, "First-principles calculations of the bulk modulus of diamond," *Solid state communications*, vol. 110, no. 10, pp. 559–564, 1999.

[85] H. McSkimin and P. Andreatch Jr, "Elastic moduli of diamond as a function of pressure and temperature," *Journal of Applied Physics*, vol. 43, no. 7, pp. 2944–2948, 2003.

[86] G. S. Manyali, "Ab-initio study of elastic and structural properties of layered nitride materials," MSc dissertation, School of Physics, University of the Witwatersrand,.

[87] N. Wang, W.-Y. Yu, B.-Y. Tang, L.-M. Peng, and W.-J. Ding, "Structural and mechanical properties of $\mathrm{Mg_{17}\ Al_{12}}$ and $\mathrm{Mg_{24}Y_5}$ from first-principles calculations," *Journal of Physics D: Applied Physics*, vol. 41, no. 19, p. 195408, 2008.

[88] J. Haines, J. Leger, and G. Bocquillon, "Synthesis and design of superhard materials," *Annual review of materials research*, vol. 31, no. 1, pp. 1–23, 2001.

[89] S. Pugh, "Xcii. relations between the elastic moduli and the plastic properties of polycrystalline pure metals," *Philosophical Magazine*, vol. 45, no. 367, pp. 823–843, 1954.

[90] L. Wei, C. Jun-Fang, H. Qinyu, and W. Teng, "Electronic and elastic properties of $\mathrm{MoS_2}$," *Physica B: Condensed Matter*, vol. 405, no. 10, pp. 2498–2502, 2010.

[91] A. Splendiani, L. Sun, Y. Zhang, T. Li, J. Kim, C.-Y. Chim, G. Galli, and F. Wang, "Emerging photoluminescence in monolayer $\mathrm{MoS_2}$," *Nano letters*, vol. 10, no. 4, pp. 1271–1275, 2010.

[92] K. Kam and B. Parkinson, "Detailed photocurrent spectroscopy of the semiconducting group vib transition metal dichalcogenides," *The Journal of Physical Chemistry*, vol. 86, no. 4, pp. 463–467, 1982.

[93] N. Troullier and J. L. Martins, "Efficient pseudopotentials for plane-wave calculations," *Physical Review B*, vol. 43, no. 3, p. 1993, 1991.

[94] D. Hamann, M. Schlüter, and C. Chiang, "Norm-conserving pseudopotentials," *Physical Review Letters*, vol. 43, pp. 1494–1497, 1979.

[95] P. Blaha, K. Schwarz, G. Madsen, D. Kvasnicka, and J. Luitz, "Wien2k," *An augmented plane wave plus local orbitals program for calculating crystal properties, Vienna University of Technology, Austria*, 2001.

[96] K. Schwarz, P. Blaha, and S. Trickey, "Electronic structure of solids with wien2k," *Molecular Physics*, vol. 108, no. 21-23, pp. 3147–3166, 2010.

[97] R. Bube, *Electronic properties of crystalline solids: an introduction to fundamentals*. Elsevier, 1974.

[98] W. Gordy and W. O. Thomas, "Electronegativities of the elements," *The Journal of Chemical Physics*, vol. 24, p. 439, 1956.

[99] W. Dawson and D. Bullett, "Electronic structure and crystallography of $\mathrm{MoTe_2}$ and $\mathrm{WTe_2}$," *Journal of Physics C: Solid State Physics*, vol. 20, no. 36, p. 6159, 1987.

[100] A. Ramasubramaniam, "Large excitonic effects in monolayers of molybdenum and tungsten dichalcogenides," *Physical Review B*, vol. 86, no. 11, p. 115409, 2012.

[101] F. Hüser, T. Olsen, and K. S. Thygesen, "On the convergence of many-body excited state calculations for monolayer $\mathrm{MoS_2}$," *arXiv preprint arXiv:1311.1384*, 2013.

[102] M. Usuda, N. Hamada, T. Kotani, and M. van Schilfgaarde, "All-electron *GW* calculation based on the *method*: Application to wurtzite ZnO," *Physical Review B*, vol. 66, no. 12, p. 125101, 2002.

[103] M. Shishkin and G. Kresse, "Self-consistent *GW* calculations for semiconductors and insulators," *Physical Review B*, vol. 75, no. 23, p. 235102, 2007.

[104] B. Holm and U. von Barth, "Fully self-consistent *GW* self-energy of the electron gas," *Physical Review B*, vol. 57, no. 4, p. 2108, 1998.

[105] W.-D. Schöne and A. G. Eguiluz, "Self-consistent calculations of quasiparticle states in metals and semiconductors," *Physical review letters*, vol. 81, no. 8, p. 1662, 1998.

[106] T. Cheiwchanchamnangij and W. R. Lambrecht, "Quasiparticle band structure calculation of monolayer, bilayer, and bulk MoS_2," *Physical Review B*, vol. 85, no. 20, p. 205302, 2012.

[107] P. E. Blöchl, "Projector augmented-wave method," *Physical Review B*, vol. 50, no. 24, p. 17953, 1994.

[108] H. Shi, H. Pan, Y.-W. Zhang, and B. I. Yakobson, "Quasiparticle band structures and optical properties of strained monolayer MoS_2 and WS_2," *Physical Review B*, vol. 87, no. 15, p. 155304, 2013.

[109] B. Radisavljevic, M. B. Whitwick, and A. Kis, "Integrated circuits and logic operations based on single-layer $\mathrm{MoS2}$," *ACS nano*, vol. 5, no. 12, pp. 9934–9938, 2011.

[110] S. Wu, Z. Zeng, Q. He, Z. Wang, S. J. Wang, Y. Du, Z. Yin, X. Sun, W. Chen, and H. Zhang, "Electrochemically reduced single-layer $\mathrm{MoS2}$ nanosheets: characterization, properties, and sensing applications," *Small*, vol. 8, no. 14, pp. 2264–2270, 2012.

[111] R. Frindt and A. Yoffe, "Physical properties of layer structures: optical properties and photoconductivity of thin crystals of molybdenum disulphide," *Proceedings of the Royal Society of London. Series A. Mathematical and Physical Sciences*, vol. 273, no. 1352, pp. 69–83, 1963.

[112] J. Wilcoxon, P. Newcomer, and G. Samara, "Synthesis and optical properties of mos and isomorphous nanoclusters in the quantum confinement regime," *Journal of applied physics*, vol. 81, p. 7934, 1997.

[113] R. Coehoorn, C. Haas, J. Dijkstra, C. Flipse, R. De Groot, and A. Wold, "Electronic structure of MoSe_2, MoS_2, and WSe_2. i. band-structure calculations and photoelectron spectroscopy," *Physical Review B*, vol. 35, no. 12, p. 6195, 1987.

[114] M. Rohlfing and S. G. Louie, "Electron-hole excitations in semiconductors and insulators," *Physical review letters*, vol. 81, no. 11, p. 2312, 1998.

[115] S. Albrecht, L. Reining, R. Del Sole, and G. Onida, "Excitonic effects in the optical properties," *physica status solidi (a)*, vol. 170, no. 2, pp. 189–197, 1998.

[116] M. C. Payne, M. P. Teter, D. C. Allan, T. Arias, and J. Joannopoulos, "Iterative minimization techniques for ab initio total-energy calculations: molecular dynamics and conjugate gradients," *Reviews of Modern Physics*, vol. 64, no. 4, pp. 1045–1097, 1992.

[117] M. T. Dove, *Structure and dynamics: an atomic view of materials*, vol. 1. OUP Oxford, 2003.

[118] D. Chadi and M. L. Cohen, "Special points in the brillouin zone," *Physical Review B*, vol. 8, no. 12, p. 5747, 1973.

[119] S. Kurth, J. Perdew, and P. Blaha, "Molecular and solid-state tests of density functional approximations: *LSD*, *GGAs*, and meta-*GGAs*," *International journal of quantum chemistry*, vol. 75, no. 4-5, pp. 889–909, 1999.

[120] E. Antončík, "Approximate formulation of the orthogonalized plane-wave method," *Journal of Physics and Chemistry of Solids*, vol. 10, no. 4, pp. 314–320, 1959.

[121] A. Savin, "The electron localization function (elf) and its relatives: interpretations and difficulties," *Journal of Molecular Structure: THEOCHEM*, vol. 727, no. 1, pp. 127–131, 2005.

[122] Y.-I. *Li, Yunguo and Li*, C. M. Araujo, W. Luo, and R. Ahuja, "Single-layer $\mathrm{MoS_2}$ as efficient photocatalyst," *Catal. Sci. Technol.*, 2013.

[123] K. F. Mak, C. Lee, J. Hone, J. Shan, and T. F. Heinz, "Atomically thin $\mathrm{MoS_2}$: A new direct-gap semiconductor," *Physical Review Letters*, vol. 105, no. 13, p. 136805, 2010.

[124] A. Molina-Sánchez and L. Wirtz, "Phonons in single-layer and few-layer $\mathrm{MoS_2}$ and $\mathrm{WS_2}$," *Physical Review B*, vol. 84, no. 15, p. 155413, 2011.

[125] P. Afanasiev, C. Geantet, C. Thomazeau, and B. Jouget, "Molybdenum polysulfide hollow microtubules grown at room temperature from solution," *Chem. Commun.*, no. 12, pp. 1001–1002, 2000.